Nonlinear Optical Spectroscopy of Two-Dimensional Materials

By

Qiannan Cui

Submitted to the graduate degree program in the Department of Physics and Astronomy and the Graduate Faculty of the University of Kansas
in partial fulfillment of the requirements for the degree of
Doctor of Philosophy.

Committee members

Dr. Hui Zhao, Chairperson

Dr. Siyuan Han

Dr. Judy Wu

Dr. Wai-Lun Chan

Dr. Rongqing Hui

Date defended: April 07, 2017

The Dissertation Committee for Qiannan Cui certifies
that this is the approved version of the following dissertation :

Nonlinear Optical Spectroscopy of Two-Dimensional Materials

Dr. Hui Zhao, Chairperson

Date approved: April 12, 2017

Abstract

Nonlinear optical properties of two-dimensional (2D) materials, such as transition metal dichalcogenides (TMDs), graphene, black phosphorus, and so on, play a key role of understanding nanoscale light-matter interactions, as well as developing nanophotonics applications from solar cells to quantum computation. With ultrafast lasers, we experimentally study nonlinear optical properties of 2D materials.

Employing transient absorption microscopy, we study several members of 2D materials, such as WSe_2, TiS_3 and ReS_2. The dynamical saturable absorption process of 2D excitons is spatiotemporally resolved. Intrinsic parameters of these 2D materials, such as exciton lifetime, exciton diffusion coefficient, and exciton mobility, are effectively measured. Especially, in-plane anisotropy of transient absorption and diffusive transport is observed for 2D excitons in monolayer ReS_2, demonstrating the in-plane degree of freedom. Furthermore, with quantum interference and control nanoscopy, we all-optically inject, detect and manipulate nanoscale ballistic charge currents in a ReS_2 thin film. By tuning the phase difference between one photon absorption and two photon absorption transition paths, sub-picosecond timescale of ballistic currents is coherently controlled for the first time in TMDs. In addition, the spatial resolution is two-order of magnitude smaller than optical diffraction limit. The second-order optical nonlinearity of 2D monolayers is resolved by second harmonic generation (SHG) microscopy. We measure the second-order susceptibility of monolayer MoS_2. The angular dependence of SHG in monolayer MoS_2 shows strong symmetry dependence on its crystal lattice structure. Hence, second harmonic generation microscopy can serve as a powerful tool to noninvasively determine the crystalline directions of 2D monolayers.

The real and imaginary parts of third-order optical nonlinearity of 2D monolayers are resolved by third harmonic generation (THG) microscopy and two-photon transient absorption microscopy, respectively. With third harmonic generation microscopy, we observe strong and anisotropic THG in monolayer and multilayer ReS_2. Comparing with 2D materials with hexagonal lattice, such as MoS_2, the third-order susceptibility is higher by one order of magnitude in ReS_2 with a distorted $1T$ structure. The in-plane anisotropy of THG is attributed to the lattice distortion in ReS_2 after comparing with a symmetry analysis. With two-photon transient absorption microscopy, we observe a giant two-photon absorption coefficient of monolayer WS_2.

Acknowledgements

I would like to greatly thank my advisor Prof. Hui Zhao for his support of my Ph. D. program in The University of Kansas. I am grateful to have the wonderful opportunity of doing research in his ultrafast laser lab. As an efficient, knowledgeable, and professional advisor, he leads me to the research field of 2D physics, teaches me state of the art laser techniques and most importantly his ways of doing research.

Many thanks to our outstanding group members: Dr. Nardeep Kumar, Dr. Rui Wang, Matthew Bellus, Frank Ceballos, Jiaqi He, Sam Lane, Zereshki Peymon, and Yuanyuan Li. I particularly thank Dr. Nardeep Kumar and Matthew Bellus for their constant help and constructive discussions. Thank Frank, Jiaqi, Sam and Peymon for sharing instruments and rotating the laser with me. Thank Yuanyuan specially for her great help on my final project. Thank Prof. Judy Wu and her group members: Jamie Wilt, Dr. Jianwei Liu and Dr. Maogang Gong, for generously sharing their equipments and experience. Thank Prof. Siyuan Han, Prof. Wai-Lun Chan and Prof. Rongqing Hui for insightful suggestions. Thank Prof. Matthew Antonik for teaching me AFM. Thank Prof. Hsin-Ying Chiu for sharing her lab for sample fabrications. Thank Prof. Fischer Chris for being my committee of comprehensive exam. Thank Prof. Rudnick Gregory for many help in the beginning of my program.Thank Mr. Robert Curry for training me towards an outstanding GTA. Thank all nice persons in department offices: Rennells Kristin, Sauerwein Joel, Teri Leahy, Hubbel Kim, and Doug Fay.

Last but not the least, I owe my parents a lifetime of love. Endless thanks to them for all the patience, understanding and support.

Contents

List of Figures

Chapter 1

Introduction

1.1 Scope of the dissertation

The early explorations of graphene [1–4] have started a new era of condensed matter physics in the past decade [5–7]. Novel two-dimensional (2D) physics based on this one-atom layer material leads to great interest ranging from fundamental to applications [6, 8, 9]. As a promising solution of future electronics, unfortunately, graphene does not inherently process a band gap, which plays a key role for modern logic electronic devices based on semiconducting materials. Inspired by graphene, with the discovery of a direct band gap 2D material-monolayer MoS_2 in 2010 [10, 11], road maps towards future electronics based on 2D materials become bright again [12–15]. More importantly, people start to realize that there are a large family of 2D materials with similar van der Waals structures and various properties ranging from superconductors to insulators, that can be exfoliated to one atomic layer [16–19]. The experimental investigations of these 2D materials have greatly boosted our understanding of 2D physics [20–27]. Although it is still a young research field, the family of 2D materials has been significantly expanded so far.

Extraordinary thin, flexible, excitonic and linear optical properties of 2D materials are appealing natures, that have been motivating people to develop novel applications in nanophotonics. However, nonlinear optical properties of 2D materials have been still largely unexplored, which are very important for determining the nonlinear optical performance limit and further de-

signing nanophotonics devices. To explore nonlinear optical properties, this dissertation focuses on nonlinear light-matter interaction phenomena and their underlying physics in 2D materials by employing nonlinear optical spectroscopy with ultrafast lasers. Nonlinear optical spectroscopy has been established as a powerful tool to evaluate and understand intrinsic physical properties of nano-materials [28], which can provide valuable information on nanoscale light-matter interactions that are inaccessible to conventional linear optical measurements. The ultrafast lasers possess high spatiotemporal resolution, high peak intensity, strong coherence, quantum interference ability, high polarization contrast, and so on. These are unique advantages for investigating 2D materials. In this dissertation, by presenting our experimental results that provide valuable information of nonlinear optical properties of 2D materials, we will demonstrate our recent studies and illustrate nonlinear optical spectroscopy we have developed in recent years with ultrafast lasers.

First of all, atomic sheets in 2D materials, such as transition metal dichalcogenides (TMDs), are bonded by van der Waals forces [29]. Unlike gapless graphene, TMD monolayers, such as MoS_2, usually possess a direct band gap. Especially, stable 2D excitons with large binding energies at room temperature dominate the linear and nonlinear optical responses of these monolayers [30]. Understanding the 2D excitonic dynamics of these materials is crucial to develop various optoelectronics applications, such as solar cells, light detectors, transistors and sensors [31]. With ultrafast lasers, we have developed a technique named as transient absorption microscopy. This nonlinear spectroscopy has unique advantages for 2D materials. Comparing with electrical measurements, ultrafast lasers can realize noninvasive measurements with extremely high temporal and spatial resolution to obtain intrinsic properties of 2D materials. In addition, since excitons have zero net charge, the electrical measurements are unable to effectively resolve the transport of excitons in 2D materials. Ultrafast lasers not only can inject excitons, but also directly detect the exciton density evolution by the transient absorption. Hence, the parameters obtained from ultrafast laser transient absorption microscopy are expected to be more accurate comparing with electrical techniques.

Heat dissipation due to diffusive transport in a semiconductor has been a critical problem for modern electronics. When the size of a silicon transistor gets smaller and smaller, overwhelming

heat generation will severely limit the performance of a computer chip. Hence, significant efforts have been devoted to search new materials for next generation electronics [32]. The emergence of 2D materials has led to new hope of fabricating next generation nano-electronics devices. On the one hand, spintronics and valleytronics based on 2D monolayers have been investigated extensively in recent years [33, 34], with the hope that spin and valley degrees of freedom can be utilized in information processing without generating heat. On the other hand, ballistic transport, the scattering free carrier transport process, can also realize zero heat dissipation [35]. Therefore, it is important to study the ballistic transport of 2D materials. Regards this, we have developed a nonlinear optical technique-quantum interference and control. All-optical injection, detection, and manipulation of nanoscale ballistic currents has been successfully realized in semiconducting 2D material-ReS_2 for the first time [36].

Last but not the least, ultrafast lasers with extremely high peak intensity can effectively induce nonlinear optical responses, such as second harmonic generation (SHG), third harmonic generation (THG) and two-photon absorption (TPA), in 2D materials. Comparing with linear optical methods, these nonlinear optical phenomena are more effective to reveal valuable information of 2D materials. With ultrafast laser, SHG microscopy can effectively reveal the crystalline direction as well as the second-order susceptibility of 2D monolayers. Besides the measurement of third-order susceptibility, THG can reveal the lattice distortion existing in special 2D materials. TPA measurements with ultrafast laser can quantify nonlinear optical parameters of 2D materials, such as TPA coefficient, that will boost many useful applications based on 2D materials, such as saturable absorber for passive Q-switching [37].

In summary, this dissertation aims to present nonlinear optical spectroscopy we have developed for 2D materials in recent years, with the hope of stimulating nonlinear optical studies of 2D materials from fundamentals to applications. The organization of the dissertation is as follow:

In the first chapter, we make an introduction to the 2D materials. The concept of 2D excitons in monolayers is explained by comparing with 3D excitons in a bulk semiconducting flake. The relaxation processes of 2D excitons are further discussed. Then, we illustrate the mechanism of

probing 2D excitons of 2D materials with ultrafast lasers.

In the second chapter, we discuss the nonlinear light-matter interaction in 2D materials. The nonlinear optical responses of 2D materials are derived by convolution theory and interpreted in the frequency domain up to third-order. The pump-probe mechanism is explained by a dynamical saturable absorption process. The principles of temporal and spatial scan with ultrafast lasers are illustrated in details. The observed diffusive transport of excitons are further illustrated by a 2D diffusion model.

In the third chapter, we present our experimental results regarding excitonic dynamics in several different 2D materials investigated by transient absorption microscopy. Explicitly, we measure intrinsic parameters of excitons in monolayer and bulk WSe_2 and discuss their differences. Similarly, we also measure TiS_3 nanorribbons. At last ,we present measurements of in-plane anisotropy of 2D excitons in monolayer ReS_2.

In the fourth chapter, we present the quantum interference and control nanoscopy. With this technique taking advantage of quantum interference between one-photon and two-photon transition paths, for the first time, we realize the injection, detection and manipulation of nanoscale ballistic currents in TMDs-ReS_2.

In the fifth chapter, we focus on the second-order nonlinearity of 2D materials by second harmonic generation (SHG) microscopy. Experimentally, we illustrate SHG microscopy of monolayer MoS_2, and discuss the calculation of second-order susceptibility and characterization of lattice orientation. For comparison, we present experimental results of SHG observed in monolayer ReS_2.

In the sixth chapter, we investigate third-order nonlinearity of 2D materials. Experimentally, we present third-harmonic generation (THG) microscopy of monolayer and multilayer ReS_2. Strong and anisotropic THG are observed in this anomalous 2D material with a stable distorted 1T lattice structure. The third-order susceptibility is calculated. The anisotropic THG is compared with a theoretical simulation, then attributed to the lattice distortion.

In the seventh chapter, we discuss two-photon transient absorption microscopy. Experimentally, we present the two-photon transient absorption measurements of monolayer WS_2 and calcu-

late its two-photon absorption coefficient.

1.2 2D materials

1.2.1 The family of 2D materials

2D materials are a family of nano-materials with layered van der Waals structure, that have been widely explored in the near decade. Graphene has created numerous opportunities for novel physics since 2004, when Geim's group for the first time made monolayer graphene with scotch tapes and revealed novel properties in graphene [1, 2]. So far, almost a million papers related to graphene have been published according to Google Scholar. However, the lack of a bandgap limited its application in optoelectronics. Although opening a band gap in graphene can be accomplished, the obtained band gap is usually too small for modern optoelectronics applications in visible and near infrared ranges [38, 39]. In 2010, monolayer MoS_2 was confirmed to have a direct band gap [10, 11], which greatly expanded the family of 2D materials. Various members of transition metal dichalcogenides (TMDs) has been extensively investigated. With band gaps in visible range and outstanding excitonic properties, the family of TMDs have become a hot candidate of next-generation optoelectronics [40].

TMDs typically form in a formula of MX_2, where M is a transition metal atom and X is a chalcogen atom. There are 16 different M elements in group 4, 5, 6, 7, 9, and 10, while there are only 3 different X elements [41]. About 40 different TMDs exist. Bulk TMDs show diverse properties. For example, there are insulators such as HfS_2, semiconductors such as $MoSe_2$ and WSe_2, semimetals such as WTe_2 and $TiSe_2$, metals such as NbS_2 and VSe_2, and even superconductors at low temperatures such as $NbSe_2$ and TaS_2. The property differences are mainly determined by the bonding coordination of transition metal atom and its *d*-orbital electrons. A detailed description of crystal growing, stacking and crystal phases could be found in [41]. TMD monolayers process different properties comparing with bulk, due to the quantum confinement effects and 2D crystal symmetry [40, 41]. For example, it has been shown that monolayer MoS_2 is direct band gap while

bulk MoS_2 is indirect [10, 11]. Strong second harmonic generation in monolayer MoS_2 presents anisotropic dependence of in-plane symmetry, which has become a powerful method of nonlinear imaging [42]. In addition, large exciton binding energy and strong excitonic effects can also been found in TMD monolayers such as WS_2 and WSe_2 [43]. Most importantly, TMD monolayers introduce a new quantum degree of freedom-the valleys, which are inequivalently located at K points [44]. TMD monolayers have became a new platform of coupled spin-valley physics. Beyond TMDs and graphene, other members of 2D materials, such as h-BN [45, 46] and black phosphorus [47–49], have also gained tremendous attentions in recent years. Very recently, the concept of van der Waals heterostructures has been introduced in [50], which will extend the family of 2D materials from natural existing to artificially designed in the near future.

1.2.2 Synthesis of 2D materials

Due to the attractive properties of 2D materials, synthesis of 2D monolayers has become an important mission for this rapidly growing research field. So far, various synthesis methods of 2D materials have been developed. In general, synthesis techniques of 2D materials can be classified into three different types: exfoliations, vapor depositions, and alternative fabrication.

To simply obtain a sample for lab research, exfoliation is the most common method. This method usually requires a bulk flake to begin with. Individual layers are separated from the bulk flake by exfoliations. Specifically, mechanical, chemical, and thermal exfoliations taking advantage of weak van der Waals forces among layers of 2D materials have been widely employed. Chemical and thermal exfoliations [51, 52] involving liquid suspensions or heat treatments can yield monolayers and few layers, but will often introduce defects. Mechanical exfoliation can yield a sample of high quality with less defects comparing with chemical and thermal exfoliations. It has been named as "Scotch tape" method due to the fabrication of the first graphene a decade ago [1]. An adhesive tape was used to peel off layers a few times from a bulk flake. Then, monolayers can be produced and left on these tapes. Next, all of residuals on the tape would be transferred to a substrate. At last, monolayers on the substrate could be identified by characterization methods,

such as optical contrast, optical path length, atomic force microscopy, and Raman spectroscopy. Although the quality of samples by mechanical exfoliation are satisfactory, the yield is very limited and the sizes are usually small (on the order of micrometers). To increase the yield and sample size without introducing defects from any liquid chemical, a technique called "all-dry viscoelastic stamping" has been brought up recently [53]. A stamp made of polydimethylsiloxane (PMDS) serves as a transitional substrate for mechanical exfoliation of a bulk flake. The viscoelastic properties of the stamp facilitate the exfoliation and lead to relatively high yield of monolayers and few layers. In addition, the transparent stamp can be easily integrated into an optical imaging system to transfer the exfoliated sample to a desired position of another substrate. PDMS viscoelastic stamping has become an effective top-down method to fabricate van der Waals heterostructures.

Although the exfoliation methods serve well for fundamental studies, practical applications needs massive and stable production. To solve this problem, bottom-up methods based on vapor depositions, such as chemical vapor deposition (CVD) and physical vapor deposition (PVD), became a very promising solution and attracted a lot of efforts. CVD method provides a solution of growing large scale of 2D materials for industrial applications, such as integrated electronics [54, 55]. CVD usually requires high temperature and certain vacuum conditions, where monolayers are deposited on a substrate via chemical reactions. So far, 2D materials fabricated by CVD have still been limited by defects, resulting in low electronic transport performances [56]. However, CVD is capable of fabricating complicated heterostructures [57, 58]. This will not only lead to unconventional heterostructures that exfoliation methods could not reach, but also provide new route to develop novel materials and devices. Similar to CVD, PVD needs high temperature treatment, but does not involve any chemical reaction towards the formation of 2D materials on substrate [59]. There are also some alternative fabrication methods to produce 2D materials. For instance, laser-thinning of MoS_2 has been demonstrated that one can use laser machining techniques to fabricate large-area MoS_2 monolayer [60].

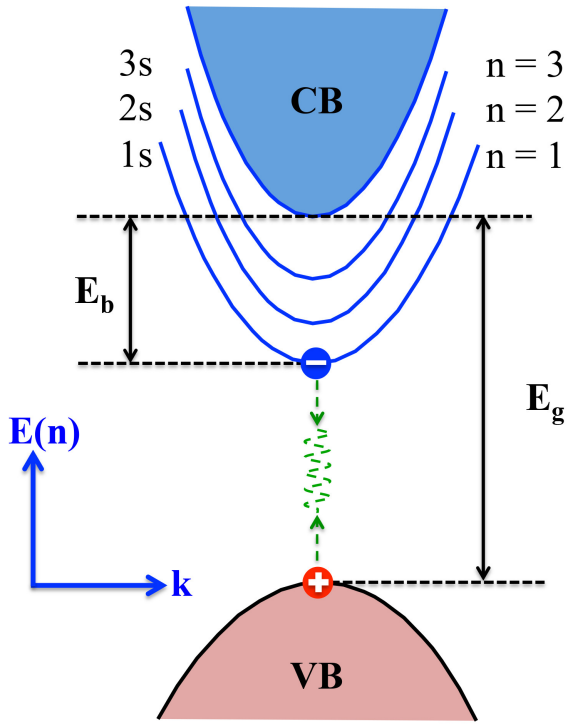

Figure 1.1: Exciton band structure in a direct-gap semiconductor.

1.3 2D excitons

1.3.1 Excitons in 3D semiconductors

For a typical direct-gap semiconductor, electron dispersion (that is, energy-momentum relation) near the edges of the conduction and valence bands can be simplified to a parabolic shape. If the photon energy of a laser is higher than the semiconductor band gap, under the illumination of this laser, electrons in the valence band will absorb the photon energy and can be excited into the conduction band. Instantaneously, a hole will be created in the valence band. Under this picture of interband transition, Coulomb interactions between the injected electron-hole pairs can form quasiparticles, that is, the excitons. There are usually two types of excitons: Frenkel excitons and Wannier excitons [61]. Frenkel excitons have a relatively smaller radius and large binding energy, while Wannier excitons have relatively large radius and small binding energy [61].

As shown in Figure 1.1, the energy levels of excitons are similar to a hydrogen atom, which

is formed by highly bound proton-electron pair. The exciton has no net charge, but a mass. The reduced mass of an exciton (m^*_{ex}) can be considered in the center-of-mass coordinate, according to the effective mass of the electron in the conduction band and the hole in the valence band [62],

$$\frac{1}{m^*_{ex}} = \frac{1}{m^*_e} + \frac{1}{m^*_h}, \tag{1.1}$$

where m^*_e and m^*_h are the effective mass of electron in the conduction band and the effective mass of hole in the valence band, respectively. Hence, such a two-body problem can be equivalently simplified to a one-body problem. In analogy with hydrogen atom, the energy of excitons can be described as [63],

$$E(n) = -\frac{E_b}{n^2}, \tag{1.2}$$

where n and E_b are quantum number and $1s$-exciton binding energy, respectively. Exciton binding energy is an important parameter to characterize the optical responses of a semiconductor material. Especially when the exciton binding energy is higher than the thermal energy k_bT, excitons will dominate the optical properties of semiconductor at that temperature.

In the real space, exciton can be interpreted as a bound electron-hole pair, occupying a certain space of crystal lattice. According to quantum mechanics, define the Bohr radius of an exciton as [62],

$$r_{ex} = \frac{\varepsilon \hbar^2}{m^*_{ex} e^2}, \tag{1.3}$$

where ε and $\hbar$ are environment dielectric constant and Planck constant, respectively. Due to the Coulomb interaction, the exciton binding energy (energy of its ionisation) is,

$$E_b = \frac{\hbar^2}{2m^*_{ex} r^2_{ex}}. \tag{1.4}$$

The exciton binding energy for a bulk semiconductor is usually small. For instance, the exciton

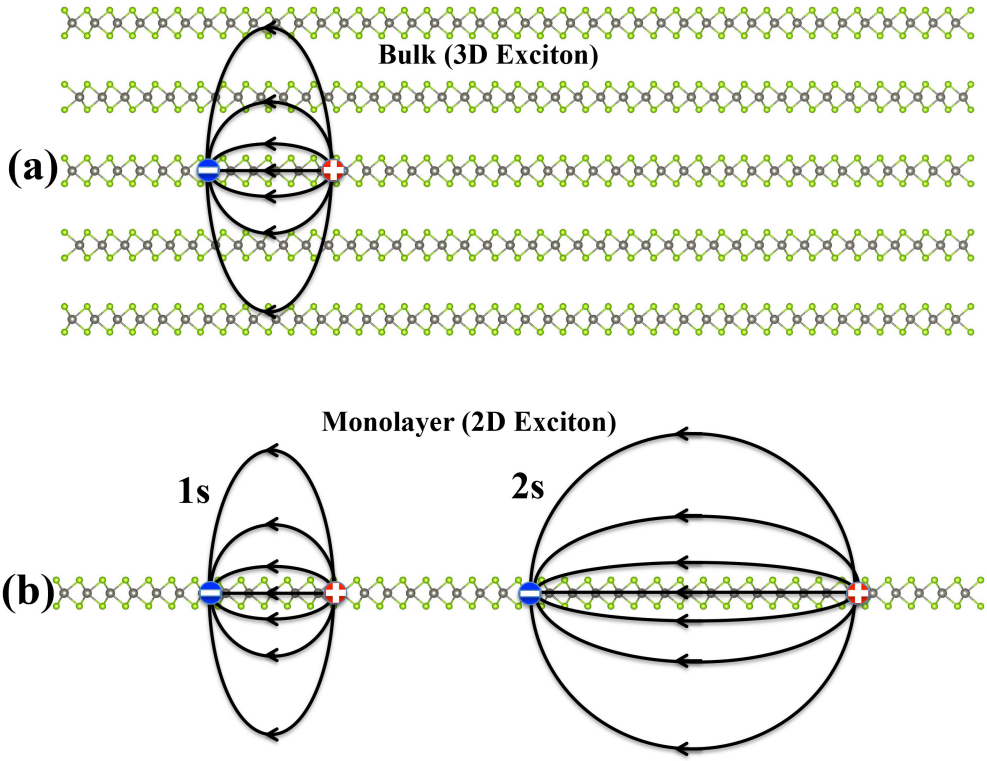

Figure 1.2: (a) 3D exciton in the bulk semiconductor. (b) 2D exciton in the monolayer semiconductor.

binding energy of bulk GaAs is only a few meV, much smaller than the thermal energy at room temperature [61]. Hence, excitons of bulk semiconductors are not stable at room temperature.

1.3.2 Excitons in 2D semiconductors

When the thickness of a semiconductor is as thin as only one atomic layer, quantum confinement will change the wavefunction of excitons. The real space occupation of 2D excitons will be confined to a certain area. More importantly, the significantly reduced coulomb screening, due to the extension of field lines in the surrounding vacuum, will greatly influence the exciton binding energy. In general, the exciton binding energy in 2D monolayers can reach as high as a few hundred meV at room temperature. Comparing with 3D case, the Bohr radius of 2D exciton becomes [64],

$$r_{2D}(n) = (n - \frac{1}{2})\frac{\varepsilon\hbar^2}{m^*_{ex}e^2}. \tag{1.5}$$

The energy levels of 2D exciton [64],

$$E_{2D}(n) = -\frac{E_b}{(n-\frac{1}{2})^2}. \tag{1.6}$$

The binding energy of 2D exciton [64],

$$E_{2Db}(n) = \frac{\hbar^2}{2m^*_{ex}r_{2D}(n)^2} = \frac{m^*_{ex}e^4}{2\hbar^2\varepsilon^2(n-\frac{1}{2})^2}. \tag{1.7}$$

From the expression of 2D exciton , the binding energy of different quantum numbers is altered. When n = 1, the 1s-exciton in 2D has a factor of 4 enhancement, in comparison with 3D case. Beyond formula expression, Coulomb screening effects will influence the binding energy. Therefore, in 2D monolayers, the reduced dielectric constant must be taken into consideration. It can be easily understood from the Figure 1.2. In 3D semiconductor, the dielectric environment is dominated by the bulk semiconductor. Hence, the dielectric constant determining the binding energy can be simply taken as the dielectric constant of the semiconductor material, as shown in Figure 1.2 (a). However, in a 2D monolayer indicated in Figure 1.2 (b), the dielectric constant term will be reduced by the weak .Coulomb screening from the environment or the substrate, since the electrical lines between electron and hole are leaking into the air or substrate. In this scenario, a nonlocal screening model is required [65]. In addition, for 2s-exciton in 2D, the Bohr radius is larger than 1s-exciton. Hence, the Coulomb screening for 2s-exciton is expected stronger. An experimental study in monolayer WS_2 has been established in [64], where a large exciton binding energy of 320 meV has been observed.

Semiconducting members of TMDs are ideal platforms to study 2D excitons. They are usually formed with a formula of MX_2, where M is a transition atom (Mo and W) and X is a chalcogenide atom (S, Se and Te). Similar to graphene, the crystal lattice of monolayer MX_2 is hexagonal, as shown in Figure 1.3 (a). Different from graphene, there are three layers of atoms for MX_2 monolayer. The M atoms are sandwiched by two layers of X atoms, as shown in Figure 1.3 (b). The primitive unite cell is indicated by the diamond of dashed lines. a_0 is the lattice constant

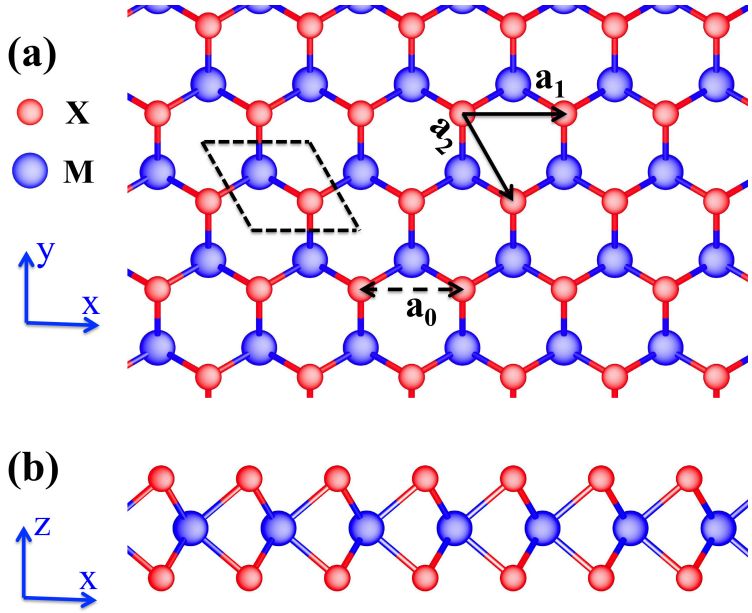

Figure 1.3: (a) Top view of lattice structure of MX_2 monolayers. The diamond of dashed lines is the primitive unit cell. Lattice constant $a_0 \approx 0.32$ nm. (b) Side view. M atoms are sandwiched by two layers of X atoms.

indicated by the double arrow along the zigzag direction. The basis vectors then can be written as,

$$\vec{a}_1 = (a_0, 0), \qquad \vec{a}_2 = (\tfrac{1}{2}a_0, -\tfrac{\sqrt{3}}{2}a_0). \tag{1.8}$$

In reciprocal space, the corresponding vectors are,

$$\vec{b}_1 = (\tfrac{2\pi}{a_0}, -\tfrac{2\pi}{\sqrt{3}a_0}), \qquad \vec{b}_2 = (0, \tfrac{4\pi}{\sqrt{3}a_0}). \tag{1.9}$$

As dominating carriers in semiconducting members of TMDs, light-2D exciton interactions highly depend on corresponding electronic structures. A variety of theoretical models have been developed to describe the electronic structures of TMD monolayers, such as tight binding models [66, 67] and $k \cdot p$ models [33, 68]. For illustration, a simple two-band $k \cdot p$ model by Xiao *etal*. in 2012 [33] is presented here. Considering the strong spin-orbit coupling originating from d orbitals of transition metal atoms, the Hamiltonian is given by [33],

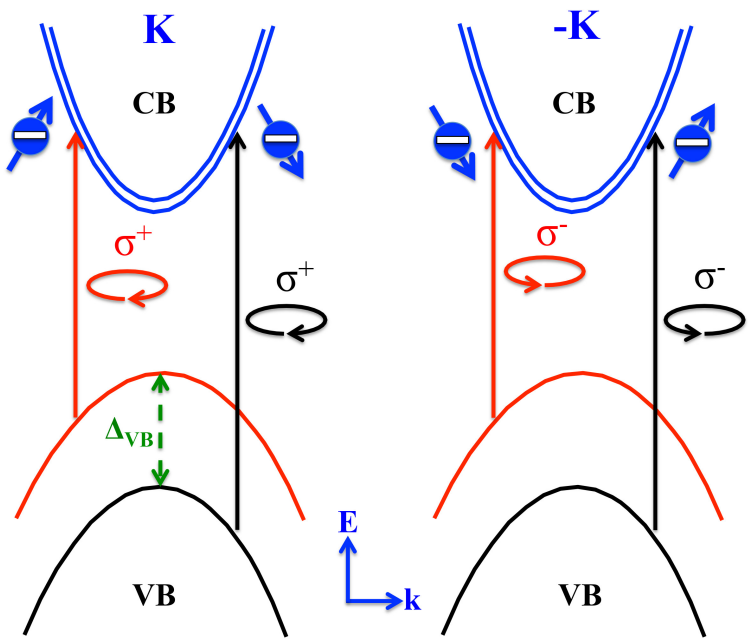

Figure 1.4: Optical selection rule for coupled spin-valley physics in TMD monolayers.

$$\hat{H} = a_0 t(\tau k_x \hat{\sigma}_x + k_y \hat{\sigma}_y) + \frac{\Delta}{2}\hat{\sigma}_z - \lambda\tau\frac{\hat{\sigma}_z - 1}{2}\hat{s}_z, \tag{1.10}$$

where a_0 is the lattice constant, t is the effective hopping integral, Δ is the energy gap, 2λ is the spin splitting at the top of valence band, $\tau = \pm 1$ is the valley index, $\hat{\sigma}$ is Pauli matrices for basis functions, and $\hat{s}_z$ is Pauli matrices for spin. The spin splitting at different valleys must be opposite because of time-reversal symmetry.

The coupled spin-valley band structure of TMD monolayers (MX_2) is depicted in Figure 1.4. The strong spin-orbit coupling induces a large splitting of valence bands in K and -K valley. The energy difference of splitting valence band top, Δ_{VB}, is typically a few hundred meV for MX_2 monolayers. Corresponding optical selection rules can be evaluated by considering the interband transition from valence band top to conduction band bottom. The coupling strength of circular polarized light $\sigma_\pm$ with the TMD monolayers would be [33],

$$\hat{P}_\pm(\mathbf{k}) = \hat{P}_x(\mathbf{k}) + i\hat{P}_y(\mathbf{k}), \tag{1.11}$$

where $\hat{P}_\alpha(\mathbf{k})$ is the interband matrix element of the canonical momentum operator [69]. Approximately, near K points, the interband transition probability has been calculated as [33],

$$|\hat{P}_\pm(\mathbf{k})|^2 = \frac{m_0^2 {a_0}^2 t^2}{\hbar^2}(1 \pm \tau \frac{\Delta'}{\sqrt{{\Delta'}^2 + 4{a_0}^2 t^2 k^2}})^2, \tag{1.12}$$

where Δ' is the spin-dependent band gap and m_0 is the free electron mass. Due to $\Delta' \gg atk$, the interband transition probability can be simplified to [33],

$$|\hat{P}_\pm(\mathbf{k})|^2 \approx \frac{m_0^2 {a_0}^2 t^2}{\hbar^2}(1 \pm \tau)^2. \tag{1.13}$$

Therefore, when coupling with K valley, that is, τ = +1, the interband transition probability will be zero for circular polarization σ_-. Only circular polarization σ_+ will realize the interband transition in K valley, as show in Figure 1.4. Similarly, for τ = -1, only circular polarization σ_- will realize the interband transition in -K valley.

1.3.3 Energy relaxations in 2D semiconductors

Followed by an ultrafast laser pulse excitation from thermodynamic equilibrium, a semiconductor will go through several energy relaxation processes to reach thermodynamic equilibrium again. These processes are occurring in four temporally overlapped regimes, including coherent relaxation, non-thermal relaxation, hot-carrier relaxation and isothermal relaxation, which have been well discussed for a traditional semiconductor in [70]. The coherent relaxation, generally called decoherence, starts immediately after the excitation of the ultrafast laser pulse, the electromagnetic field of which creates a well-defined phase relation with the injected carrier ensemble. In 2D semiconductors, the established coherence will be destroyed by scattering within a sub-picosecond timescale. After decoherence, the distribution of injected excitons and free $e-h$ pairs is very likely non-thermal. That is, the distribution function cannot be described by a temperature. The non-thermal relaxation is within a timescale of picosecond. The temperature of thermalized distribution is usually higher than the lattice temperature [70]. For 2D semiconductors, the timescale

of hot-carrier is within a few picoseconds. 2D excitons are likely formed after hot-carrier relaxation processes. When the temperature of excitation ensemble, such as excitons, free $e-h$ carriers and phonons, reduces to the same as the temperature of lattice, the isothermal relaxation will start [70]. The isothermal relaxation will finally lead 2D semiconductors to thermodynamics equilibrium through radiative or non-radiative recombination. The timescale of isothermal relaxation can range from a few picoseconds to a few nanoseconds, depending on quite a few conditions, such as defects, temperature, carrier density, et al [70].

Employing the nonlinear optical spectroscopy, one can study all these four relaxations in 2D semiconductors. First of all, the population of stable 2D excitons at room temperature likely reaches a maximal value after the hot-carrier relaxation. The isothermal relaxation will account for the lifetime of excitons in a 2D semiconductors. Hence, the process of isothermal relaxation has been of particular interest so far for the majority of ultrafast laser spectroscopy. In a non-degenerate pump-probe measurement, the isothermal relaxation can be resolved, together with faster mechanism such as hot-carrier relaxation. The discussion of transient absorption measurements for excitonic dynamics will be presented in Chapter 3 at low carrier density from 10^{11} to 10^{12} cm^{-2}. Secondly, in the coherent regime, the 2D semiconductors have been predicted to be a novel platform of all-optical coherent control. Experimentally, with quantum interference between one-photon absorption and two-photon absorption transition paths, we also study the coherent carrier dynamics. Corresponding discussion will be presented in Chapter 4.

Chapter 2

Nonlinear light-matter interactions

2.1 Light-matter interaction in 2D materials

Light-matter interaction is an important phenomenon when investigating the physical properties of 2D materials. Based on Maxwell's equations, one can derive wave equation of light-matter interaction [71],

$$\nabla^2 \vec{E} = \mu_0 \varepsilon_0 \frac{\partial^2 \vec{E}}{\partial t^2} + \mu_0 \frac{\partial^2 \vec{P}}{\partial t^2}, \tag{2.1}$$

where $\vec{P}$ is the polarization. This equation indicates that when a time-varying polarization exists, electromagnetic radiation will be generated. Therefore, the polarization is important for interpreting the nonlinear light-matter interaction when the light is in the form of ultrafast laser pulses. Intuitively, time-dependent polarizations can be treated as an intermediate source generating the output of electromagnetic radiations [71]. In a dielectric material, the optical polarization, $\vec{P}(t)$ is induced by the electrical field of the illuminating light $\vec{E}(t)$. The induced polarization takes the form of convolution [72],

$$\vec{P}(t) = \varepsilon_0 \int_{-\infty}^{\infty} R(\tau) \vec{E}(t-\tau) d\tau, \tag{2.2}$$

where $R(\tau)$ is the intrinsic response function of the dielectric material, which is equivalent to a Green's function, since it yields the response of polarization from a delta function input of light electric field. In the temporal domain, causality requires that the effect should be always generated after the cause. Then, in the above convolution, when $t < t - \tau$, $\vec{E}(t-\tau)$ cannot contribute to the polarization $\vec{P}(t)$. As a result, the response function $R(\tau)$ needs to be zero for $\tau < 0$. Based on the analysis of causality, the convolution will be zero for negative time. To reveal the physical nature of a convolution, Fourier transform is usually carried out. The conversion from the time domain to the frequency domain will point to the following form of product [72],

$$\vec{P}(\omega) = \varepsilon_0 \chi(\omega) \vec{E}(\omega), \tag{2.3}$$

where $\chi(\omega)$ is the electric susceptibility of the dielectric material, which is an intrinsic parameter. Based on the above discussion, $\chi(\omega)$ is the Fourier transform of the response function $R(t)$ [72],

$$\chi(\omega) = \int_{-\infty}^{\infty} R(\tau) e^{-2\pi i \omega \tau} d\tau. \tag{2.4}$$

Under the illumination of ultrafast laser, the responses of a dielectric material are usually nonlinear, since the electric field of the laser is very high. In nonlinear optics, the corresponding polarization is usually expanded to an infinite series with respect to the electric field in the time domain [72],

$$\vec{P}(t) = \vec{P}_i^{(1)}(t) + \vec{P}_{ij}^{(2)}(t) + \vec{P}_{ijk}^{(3)}(t) + \cdots\cdots + \vec{P}_{ijk\cdots}^{(n)}(t). \tag{2.5}$$

Apply the convolution formalism for each scalar term [72],

$$
\begin{aligned}
P_i^{(1)}(t) &= \varepsilon_0 \int_{-\infty}^{\infty} R_{ij}^{(1)}(\tau_1) E_j(t-\tau_1) d\tau_1, \\
P_{ij}^{(2)}(t) &= \varepsilon_0 \int_{-\infty}^{\infty}\int_{-\infty}^{\infty} R_{ijk}^{(2)}(\tau_1,\tau_2) E_j(t-\tau_1) E_k(t-\tau_2) d\tau_1 d\tau_2, \\
P_{ijk}^{(3)}(t) &= \varepsilon_0 \int_{-\infty}^{\infty}\int_{-\infty}^{\infty}\int_{-\infty}^{\infty} R_{ijkl}^{(3)}(\tau_1,\tau_2,\tau_2) E_j(t-\tau_1) E_k(t-\tau_2) E_l(t-\tau_3) d\tau_1 d\tau_2 d\tau_2, \\
&\vdots \\
P_{ijk\cdots}^{(n)}(t) &= \varepsilon_0 \int_{-\infty}^{\infty}\cdots\int_{-\infty}^{\infty} R_{ijk\cdots n+1}^{(n)}(\tau_1,\cdots,\tau_n) E_j(t-\tau_1)\cdots E_n(t-\tau_n) d\tau_1\cdots d\tau_n,
\end{aligned}
\tag{2.6}
$$

where the symbols, j,k,l, are the tensor elements of χ along different directions. After Fourier transform of the above terms of $P(t)$, the scalar form of the induced polarization can be obtained in the frequency domain as [72],

$$
P(\omega) = \varepsilon_0 \{ \chi_{ij}^{(1)} E(\omega_1) + \chi_{ijk}^{(2)} E(\omega_1) E(\omega_2) + \chi_{ijkl}^{(3)} E(\omega_1) E(\omega_2) E(\omega_3) + \cdots + \chi_{ijk\cdots n+1}^{(n)} E(\omega_1) \ldots E(\omega_n) \}.
\tag{2.7}
$$

It should be emphasized that the n^{th} susceptibility $\chi_{ijk\cdots n+1}^{(n)}$ is a tensor of rank $n+1$. For a material with isotropic crystal lattice structure, the tensor elements can be greatly simplified by symmetry. Hence, scalar notation can be effectively employed for hexagonal 2D materials. For anisotropic crystal lattice, the symmetry will be reduced and the tensor notation is necessary. In addition, the induced polarization is a vector, because of the vector nature of applied electric fields. It would be also necessary to employ the vector notation.

In 2D materials, especially the 2D monolayers, nonlinear optical responses up to the third-order are of interest. Next, we will discuss the first, second, and third-order susceptibility in details together with physical impacts of them towards various linear and nonlinear optical phenomena induced by ultrafast lasers in 2D materials.

2.1.1 First-order susceptibility

In an isotropic medium, the first-order susceptibility $\chi^{(1)}(\omega)$ is a dimensionless parameter that is related to the linear electric relative permittivity $\varepsilon(\omega)$ by [73],

$$\varepsilon(\omega) = 1 + \chi^{(1)}(\omega), \tag{2.8}$$

and $\chi^{(1)}(\omega)$ takes a complex form [73]:

$$\chi^{(1)}(\omega) = \chi_R^{(1)}(\omega) + i\chi_I^{(1)}(\omega). \tag{2.9}$$

The linear electric relative permittivity $\varepsilon(\omega)$ is also complex and can be generalized as [73],

$$\sqrt{\varepsilon(\omega)} = n(\omega) + i\kappa(\omega) = n(\omega) + i\alpha(\omega)\frac{\lambda}{4\pi}, \tag{2.10}$$

where $n(\omega)$ and $\alpha(\omega)$ are the linear refractive index and linear absorption coefficient of the isotropic medium at the frequency of ω, respectively. Under such formalism, we can further obtain in SI units [73],

$$\begin{aligned} n(\omega) &= \sqrt{1 + \chi_R^{(1)}(\omega)}, \\ \alpha(\omega) &= \frac{\omega\chi_I^{(1)}(\omega)}{n(\omega)c}. \end{aligned} \tag{2.11}$$

From the above results, it is clear that linear refractive index and linear absorption coefficient are not independent to each other. As a result, in linear optics, a general dispersion relation has been given by the linear Kramers-Kronig relation [72],

$$n(\omega) - 1 = \frac{c}{\pi} P \int_0^\infty \frac{\alpha(\omega')d\omega'}{\omega'^2 - \omega^2}, \tag{2.12}$$

where P stands for the Cauchy principle value. Therefore, based on the above discussion, a further understanding of linear optics can be established that the macroscopic behaviors and observables in linear optics, such as refraction and absorption, are intrinsically determined by the first-order

susceptibility in an isotropic medium. For an anisotropic medium, the linear dielectric constant becomes a symmetric tensor and an explicit derivation can be found elsewhere [73].

2.1.2 Second-order susceptibility

The second-order nonlinearity of a dielectric material can be characterized by the second-order susceptibility $\chi^{(2)}$, which is a rank 3 tensor [71]. Consider an incoming electrical field with two different frequency components in the following form[71],

$$\vec{E}(t) = E_1 e^{-i\omega_1 t} + E_2 e^{-i\omega_2 t} + c.c. \tag{2.13}$$

The complex amplitude of second-order nonlinear polarization will be induced with various frequency mixing terms as [71],

$$\vec{P}^{(2)}(\omega) = P(2\omega_1) + P(2\omega_2) + P(\omega_1 + \omega_2) + P(\omega_1 - \omega_2) + P(0) + c.c. \tag{2.14}$$

Specificly, four complex amplitudes of nonlinear polarization components can be expressed in terms of $\chi^{(2)}$ as [71],

$$\begin{aligned}
P(2\omega_1) = \varepsilon_0 \chi^{(2)} E_1^2 &\implies (SHG) \\
P(2\omega_2) = \varepsilon_0 \chi^{(2)} E_2^2 &\implies (SHG) \\
P(\omega_1 + \omega_2) = 2\varepsilon_0 \chi^{(2)} E_1 E_2 &\implies (SFG) \\
P(\omega_1 - \omega_2) = 2\varepsilon_0 \chi^{(2)} E_1 E_2^* &\implies (DFG) \\
P(0) = 2\varepsilon_0 \chi^{(2)} (E_1 E_1^* + E_2 E_2^*) &\implies (OR)
\end{aligned} \tag{2.15}$$

where SHG is second harmonic generation, SFG is sum frequency generation, DFG is difference frequency generation, and OR is optical rectification. In real experiments, certain phase-matching conditions usually require no more than one polarization component can be significant [71].

2.1.3 Third-order susceptibility

The third-order nonlinearity of a dielectric material, can be characterized by the third-order susceptibility $\chi^{(3)}$, which is a rank 4 tensor [71]. Hence, third-order nonlinear phenomena are much more richer. Consider an incoming electrical field with three different frequency components in the following form [71],

$$\vec{E}(t) = E_1 e^{-i\omega_1 t} + E_2 e^{-i\omega_2 t} + E_3 e^{-i\omega_3 t} + c.c. \tag{2.16}$$

The third-order nonlinear polarization will be induced with various frequency mixing terms in scalar form as [71],

$$\begin{aligned} \vec{P}^{(3)}(\omega) &= P(\omega_1) + P(\omega_2) + P(\omega_3) + P(3\omega_1) + P(3\omega_2) + P(3\omega_3) \\ &+ P(\omega_1+\omega_2+\omega_3) + P(\omega_1+\omega_2-\omega_3) + P(2\omega_1+\omega_2) + c.c. \end{aligned} \tag{2.17}$$

There will be three polarization components with the same frequency as the the incoming light, complex amplitudes of which are [71],

$$\begin{aligned} P(\omega_1) &= \varepsilon_0 \chi^{(3)}(3E_1E_1^* + 6E_2E_2^* + 6E_3E_3^*)E_1 \\ P(\omega_2) &= \varepsilon_0 \chi^{(3)}(6E_1E_1^* + 3E_2E_2^* + 6E_3E_3^*)E_2 \implies (PM) \\ P(\omega_3) &= \varepsilon_0 \chi^{(3)}(6E_1E_1^* + 6E_2E_2^* + 3E_3E_3^*)E_3 \end{aligned} \tag{2.18}$$

where PM is phase modulation. Phase modulation includes two types: self-phase modulation (SPM) and cross-phase modulation (XPM). In addition, there will be three polarization components with triple frequencies of the incoming light, complex amplitudes of which are [71],

$$\begin{aligned} P(3\omega_1) &= \varepsilon_0 \chi^{(3)} E_1^3 \\ P(3\omega_2) &= \varepsilon_0 \chi^{(3)} E_2^3 \implies (THG) \\ P(3\omega_3) &= \varepsilon_0 \chi^{(3)} E_3^3 \end{aligned} \tag{2.19}$$

where THG is third harmonic generation. Furthermore, complex amplitudes of frequency-mixing polarization components will be listed a few as [71],

$$\begin{aligned} P(\omega_1+\omega_2+\omega_3) &= 6\varepsilon_0\chi^{(3)}E_1E_2E_3 \\ P(\omega_1+\omega_2-\omega_3) &= 6\varepsilon_0\chi^{(3)}E_1E_2E_3^* \Longrightarrow (FWM) \\ P(2\omega_1+\omega_2) &= 3\varepsilon_0\chi^{(3)}E_1^2E_2 \\ &\vdots \end{aligned} \tag{2.20}$$

where FWM is four wave mixing. Comparing with the second-order susceptibility, the third-order susceptibility of a dielectric is a few order of magnitude smaller. As a result, much higher light intensity is required for the observation of third-order nonlinear effects. From another point of view, the third-order nonlinear effects are much more sensitive. In terms of nonlinearity measurements with ultrafast lasers, both magnitude and in-plane symmetry of nonlinear susceptibility will provide valuable information for the evaluation of the 2D materials. The experimental measurements of the second-order and third-order nonlinear susceptibility will be illustrated from Chapter 5 to Chapter 7.

2.2 Transient absorption: a dynamical process of saturable absorption

In semiconductors, when an ultrafast laser pulse excites electrons from valence band (VB) to conduction band (CB), electronic states in the CB are occupied. As a result, the absorption coefficients of materials will change. This phenomenon is usually named as saturable absorption. As time goes by, the injected electrons will gradually decay back to VB. Hence, saturable absorption in semiconductors is a dynamical process.

The dynamical process is depicted in Figure 2.1, where a simplified band structure is used. Assuming a femtosecond laser pulse with the frequency of ω, the photon energy of which is higher than the band gap, illuminates the semiconductor material, electrons will be excited into CB. Initially, as shown in Figure 2.1(a), excited electrons are in a high energy level of CB. Then, due to intraband transition facilitated by phonons, excited electrons will transit to the bottom of CB and

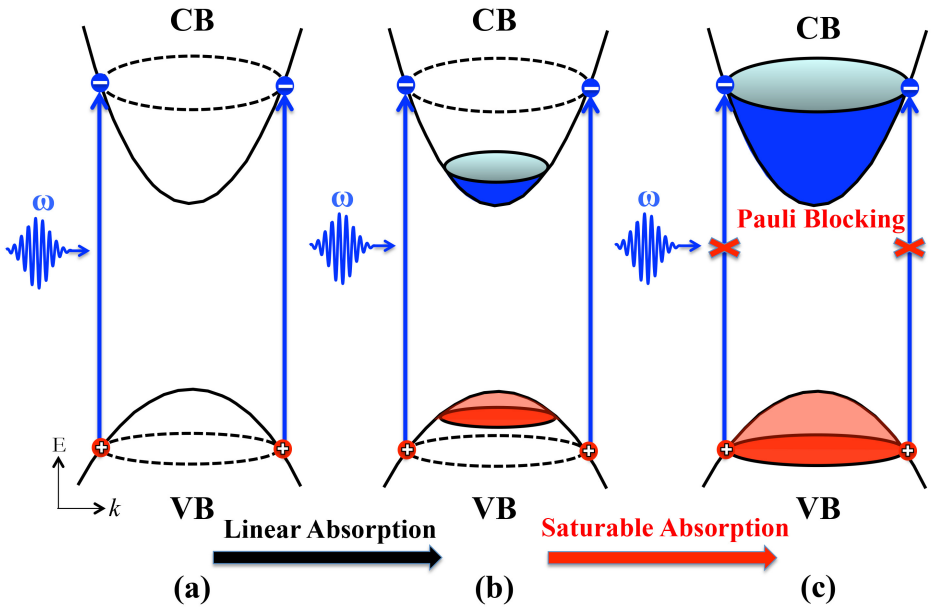

Figure 2.1: (a) Electrons are excited from valence band to conduction band by a femtosecond laser pulse; (b) States close to the bottom of CB will be gradually occupied and linear absorption is maintained; (c) All states are occupied and Pauli blocking occurs.

accumulate till available electronic states for lower states of CB are occupied, as shown in Figure 2.1(b). The states corresponding to ω, are still empty in this stage so that the absorption coefficient of incoming femtosecond laser is not affected. The absorption is still linear. As energy level of occupied states gets as high as the femtosecond laser photon energy, Pauli blocking occurs [74], indicated in Figure 2.1(c). That is because electron is a fermion. Lack of available states in CB will reduce the absorption of incoming femtosecond laser pulses, accounting for saturable absorption.

The saturable absorption discussed above is a degenerate case. In the majority of pump-probe (also called transient absorption) measurements of 2D semiconductors, the probe laser wavelength is usually different from the pump wavelength. Figure 2.2 illustrates the situation of the nondegenerate transient absorption. In this nondegenerate case, photon energy of probe laser pulse is chosen to match with the band gap while the photon energy of pump laser pulse is higher than the band gap. When $t = 0$, electrons in VB are excited to high energy level of CB, as shown in Figure 2.2(a). In the meantime, if the probe laser pulses illuminate the sample, the absorption of probe laser will not be affected since the bottom of CB is still empty. When $t = 0 + t_0$, because of intraband transition, electrons will accumulate and electronic states will be occupied in the bottom

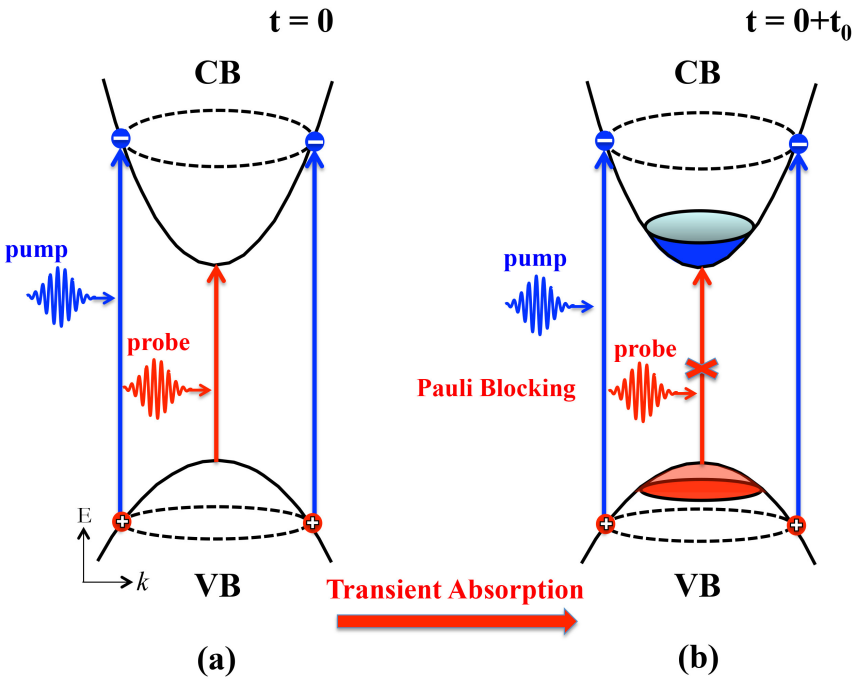

Figure 2.2: (a) Electrons are excited from VB to CB by a pump laser pulse. A probe laser pulse with photon energy close to band gap is used to detect the carrier density accumulated in the bottom of CB. (b) After some time, Pauli blocking induces the change of probe laser absorption, which is a transient effect as a function of time.

of CB, as shown in Figure 2.2(b). The absorption of incoming probe laser will be affected due to Pauli blocking. Eventually, as the electrons recombine with holes in the VB, the absorption of probe laser will recover to the situation of $t = 0$.

2.3 Probe the 2D excitons via transient absorption

Transient absorption has been a widely employed technique to resolve the temporal dynamics of injected free carriers in semiconducting materials. In 2D semiconducting monolayers, 2D excitons will be the dominating carriers instead of free carriers. Therefore, it is necessary to show the probing mechanism and probing efficiency of 2D excitons by transient absorption. Transient probing 2D excitons in quantum well structure has been well discussed by Miller et al [75].

In a bulk semiconductor, the linear susceptibility $\chi^{(1)}$ is [75],

$$\chi^{(1)} = \sum_n \frac{f_n}{\omega - \omega_n + i\gamma_n}, \tag{2.21}$$

where the index n sums over all exciton states, f_n is the oscillator strength of the transition, ω_n is the energy of each state, and γ_n is the width of each state.

For $1s$-exciton, only keep the resonance term [75],

$$\chi^{(1)} = \frac{f_{1s}}{\omega - \omega_{1s} + i\gamma_{1s}}. \tag{2.22}$$

To evaluate the change of linear susceptibility induced by the renormalization of the exciton oscillator strength [75],

$$\frac{\delta f_{1s}}{f_{1s}} = -\frac{N}{N_s}, \tag{2.23}$$

where N_s is the saturation density of exciton. There are two contributions to the change of f_{1s}: the phase-state filling effect due to the Pauli exclusion, and exciton orbital wave function renormalization.

In the dilute limit, the carrier distributions can be described by the Boltzmann distribution[75],

$$f_i(k) = \frac{N\hbar^2\pi}{m_i k_b T} e^{-\frac{\hbar^2 k^2}{2m_i k_b T}}, \tag{2.24}$$

where m_i, $i = e$ or h, are the electron or hole effective masses, and T is the temperature.

To evaluate the case of excitons, the resonant generation of excitons yields a distribution [75],

$$f_i(k) = \frac{N}{2}|U_{1s}(k)|^2, \tag{2.25}$$

where $U_{1s}(k)$ is the Fourier transform of the relative-motion orbital wave function $U_{1s}(r)$. Since an exciton is built up from a linear combination of single-particle fermion states distributed according to $U_{1s}(k)$, the creation of one exciton corresponds to an occupation probability in the fermion phase space $|U_{1s}(k)|^2$ that is equally shared between the spin-up and spin-down states, hence the factor

$\frac{1}{2}$.

In the case of 2D excitons, the wave function is [75],

$$\begin{aligned} U_{1s}(r) &= (\tfrac{2}{\pi})^{\frac{1}{2}} \tfrac{1}{a_0} e^{-2r/a_0}, \\ U_{1s}(k) &= \sqrt{2\pi} \tfrac{a_0}{(1+(a_0 k/2)^2)^{\frac{3}{2}}}. \end{aligned} \tag{2.26}$$

The relative change of the exciton oscillator strength accounting for phase-space filling (PSF) is [75],

$$\frac{\delta f_{1s}}{f_{1s}}|_{PSF} = -\sum_k [f_e(k) + f_h(k)] \frac{U_{1s}(k)}{U_{1s}(r=0)}. \tag{2.27}$$

For an exciton gas [75],

$$\frac{1}{N_s}|_{PSF,ex} = \frac{32}{7}\pi a_{2D}^2. \tag{2.28}$$

For an $e-h$ plasma, two limits of interest [75],

$$\begin{aligned} \tfrac{1}{N_s}|_{PSF,pl} &= 8\pi a_{2D}^2, \tfrac{k_b T}{E_{1s}} \ll 1, \\ \tfrac{1}{N_s}|_{PSF,pl} &= 8\pi a_{2D}^2 \tfrac{E_{1s}}{k_b T}, \tfrac{k_b T}{E_{1s}} \gg 1. \end{aligned} \tag{2.29}$$

It shows that at low temperatures, phase-space filling effects due to free $e-h$ pairs are larger than those due to excitons (7/4 times larger), but as temperature increases free $e-h$ pairs effects become weaker and eventually tend to zero. Above a temperature of about $k_b T = 7E_{1s}/4$, free $e-h$ pairs effects are smaller than exciton effects.

Next, considering the contribution of the renormalization of the exciton orbital wave function (short range exchange effects), for exciton [75],

$$\frac{1}{N_s}|_{EXCH,ex} = \frac{4832}{1225}\pi a_{2D}^2. \tag{2.30}$$

For an $e-h$ plasma, two corresponding limits of interest [75],

$$\begin{aligned} \frac{1}{N_s}|_{EXCH,pl} &= 4(\pi - 2/3)a_{2D}^2, \frac{k_bT}{E_{1s}} \ll 1, \\ \frac{1}{N_s}|_{EXCH,pl} &= 16\pi a_{2D}^2 \frac{E_{1s}}{k_bT}, \frac{k_bT}{E_{1s}} \gg 1. \end{aligned} \tag{2.31}$$

Last but not the least, it should further be noticed that the refractive index and absorption coefficient of a 2D semiconductor are related by nonlinear Kramers-Kronig formalism [72],

$$\Delta n(\omega) = \frac{c}{\pi} P \int_0^\infty \frac{\Delta\alpha(\omega')d\omega'}{\omega'^2 - \omega^2}, \tag{2.32}$$

where P stands for the Cauchy principle value.

2.3.1 Temporal scan

To obtain the temporal information of injected carrier density, the relative delay time between the pump pulse and probe pulse needs to be controlled. It is realized by precisely changing optical length of probe path, while the optical length of the pump path is fixed. Since the light speed in the air is a constant, the time of propagation of an ultrafast laser pulse can be calculated with a given optical path. Experimentally, the optical length of probe path is controlled by scanning a linear delay stage, on which a retro-mirror enables a round trip of the probe laser. The change of optical length of probe path will be twice of the change of delay stage movement. A schematic illustration of temporal scan is shown in Figure 2.3.

It needs to be noticed that the repetition frequency of our ultrafast laser cavity is about 80 MHz. Hence, the time interval of the output pulse train is about 13 ns. When a series of pump laser pulses illuminate the sample, each pulse will induce equal carrier density assuming each pulse has same energy and temporal width. A maximal carrier density is achieved within about 100 fs, which is the temporal width of pump pulses. Once the maximal carrier density is injected, the initial pump pulse will not affect the behavior of carriers until the next pump pulse arrives. The 13 ns time interval between the initial pump pulse and the next pump pulse is much longer than the carrier decay time of most 2D semiconducting materials. It means that the carrier density indeed will decrease to zero before the next pump pulse arrives. When the optical length of probe

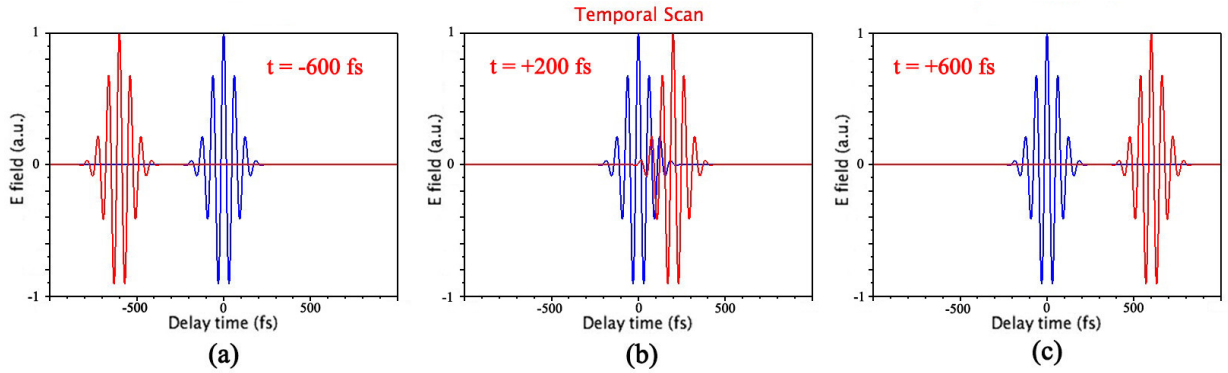

Figure 2.3: Schematic illustration of the temporal scan. The pump pulse is fixed at zero delay. Probe pulse is tuned to (a) 600 fs before zero delay; (b) 200 fs; and (c) 600 fs after the zero delay.

path is shorter than that of pump path, the probe pulse will arrive at the sample before the pump pulse. That is, in time the probe pulse is before the zero delay with respect to the pump pulse, as shown in Figure 2.3 (a). In this case, the pump pulse at zero delay has not arrived at the sample, and the carrier density induced by the previous pulse has dropped to zero. Hence, the reflection or transmission of the probe laser will not be changed. The measured differential reflection or differential transmission, which is defined as the normalized reflection or transmission of probe laser, will be zero. Now, if we increase the optical length of the probe pulse to be longer than that of pump laser, the probe pulse will arrive at the sample right after the pump pulse, as shown in Figure 2.3 (b). In this case, a carrier density has been injected by the pump pulse fixed at the zero delay. The reflection or transmission of the probe laser will be changed by the carrier density. A signal of differential reflection or differential transmission can be detected. If we keep increasing the optical length of probe pulse, indicated in Figure 2.3 (c), we will be able to measure the signal of differential reflection or differential transmission as a function of the delay time.

2.3.2 Spatial scan

To obtain the spatial information of injected carrier density, the relative position between the pump spot and the probe spot needs to be controlled. In a pump-probe measurement, pump and probe beams are collimated by two different beam splitters. Reflected pump and probe beams are then

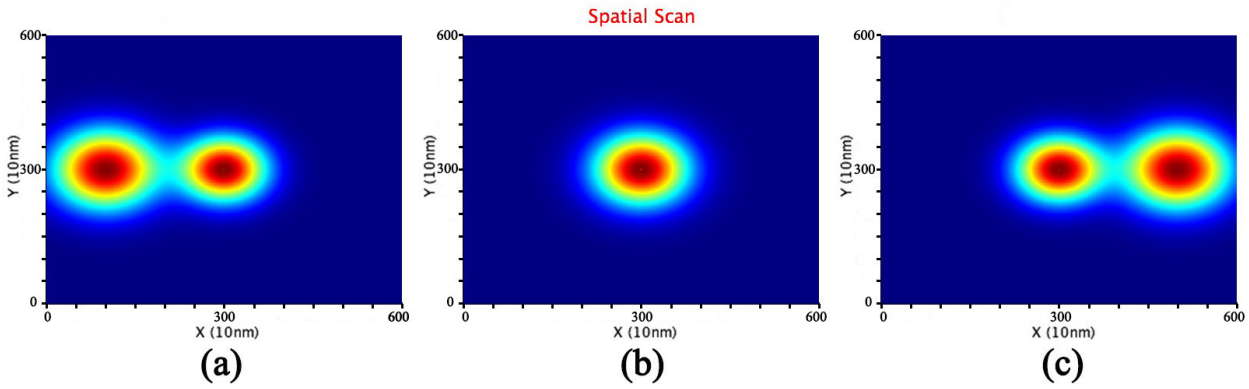

Figure 2.4: Schematic illustration of the spatial scan. The pump spot is fixed at the origin of x-y plane in the lab coordinate. The tilting angle of the probe beam before the objective lens is altered along the horizontal direction. (a) Probe spot is moved to the left of the pump spot; (b) Probe spot overlaps with pump spot; (c) Probe spot is moved to the right of the pump spot.

together focused by an objective lens on the sample. The beamsplitters change the direction of pump and probe beams by 90 degree. Hence, when tilting the beamsplitters, the reflection angle will be changed and the corresponding pump and probe spots on the sample will move as well. Using small angle approximation, when the tilting angle is small, the spatial movement of spot position will be proportional to the tilting angle. Based on this analysis, the spatial scan can be realized by tilting the beamsplitter of probe beam, while the beamsplitter of pump beam is fixed.

To better illustrate the spatial-scanning process, a schematic illustration is presented in Figure 2.4. The beam splitter of pump spot will be fixed so that the pump spot remains at the same position of the sample. The beamsplitter of the probe beam is mounted with a picomotor, which controls the tilting angle along the horizontal direction in the lab coordinate. Hence, when the picomotor moves multiple steps, the probe spot on the sample will move along the horizontal direction accordingly. The spatial-scanning system usually needs to be calibrated in order to convert moving steps of picomotor to the real spatial distance of probe spot movement. The calibration is facilitated by a CCD imaging system in our experiments.

First, the pump and probe spots are perfectly overlapped with each other to ensure the efficiency of detection. That is, the center of pump spot should be overlapped with the center of probe spot on the sample. By tilting a small angle of the probe beamsplitter, the probe spot is moved to the

left of the pump spot, indicated in Figure 2.4 (a). Then, oppositely tilting the probe beamsplitter will scan the probe spot horizontally across the pump spot. Figure 2.4(b) shows the probe spot is overlapped with pump spot. In this way, the spatial scan is accomplished until the probe spot is moved to the right of pump spot as shown in Figure 2.4(c). The signal of differential reflection or differential transmission can be measured as a function of space.

2.3.3 Diffusion model

Assume $N(r,t)$ is the exciton density in 2D space at position r and time t. Then, the flux can be expressed as,

$$\vec{J} = -D\nabla N. \tag{2.33}$$

For 2D material with in-plane anisotropic transport property, diffusion tensor D is a 2 by 2 matrix, the flux $\vec{J}$ will be a vector which shows the gradient of exciton density as a function of space. Due to the conservation of mass, we will get,

$$\frac{\partial N}{\partial t} = -\nabla \cdot \vec{J}, \tag{2.34}$$

where $\nabla \cdot \vec{J}$ is the divergence of the flux, which is,

$$\nabla \cdot \vec{J} = \frac{\partial J_x}{\partial x} + \frac{\partial J_y}{\partial y}. \tag{2.35}$$

Therefore, 2D anisotropic exciton diffusion equation can be given as,

$$\frac{\partial N}{\partial t} = \nabla \cdot (D\nabla N). \tag{2.36}$$

The fundamental solution in 2D can be derived by the transition probability with n-dimensional Gaussian kernel function [76],

$$N(r,t) = \frac{1}{4\pi t\sqrt{detD}} exp^{-\frac{1}{4t}r^T D^{-1} r}. \tag{2.37}$$

Since D is symmetric matrix, the eigenvalues of D could be obtained by its diagonal matrix. The level sets of carrier density function can be given by [76]: $r^T D^{-1} r = constant$. Therefore, the equal exciton density in 2D space will form an ellipse. Assume λ_1 and λ_2 are the eigenvalues of D, the structure of the diffusion tensor can be visualized by: $\frac{x^2}{\lambda_1} + \frac{y^2}{\lambda_2} = constant$.

For 2D materials with in-plane isotropic transport property, diffusion tensor D reduces to a scalar. In the meantime, the total exciton density will decrease due to exciton recombination. As a result, 2D isotropic exciton diffusion equation changes to,

$$\frac{\partial N}{\partial t} = D\nabla^2 N - \frac{N}{\tau}, \tag{2.38}$$

where τ is lifetime of injected excitons.

The macroscopic nature of a laser is Gaussian beam. Gaussian function will still be Gaussian after Fourier transformation, which is the focusing process by a lens in optics. Therefore, the fluence distribution of the pump spot in the sample should be also a 2D Gaussian distribution. In a linear absorption regime, the initial condition: injected exciton density by the pump when t = 0, will be a 2D Gaussian distribution,

$$N(r,0) = N_0 e^{-\frac{r^2}{\sigma(0)^2}}, \tag{2.39}$$

where $r^2 = x^2 + y^2$ and $\sigma(0)$ is the $1/e$ half width of the spatial profile for the 2D isotropic exciton density when t = 0. It is straightforward to interpret the diffusion process with the example presented in Figure 2.5. Initially, at 0 ps, a Gaussian distribution of exciton density is injected as shown in Figure 2.5 (a). At 100 ps, due to diffusion, the exciton density is expanded in space, as shown in Figure 2.5 (c). To be clear, cross-sections of spatial profiles of exciton density along horizontal direction at 0 ps and 100 ps are indicated in Figure 2.5 (b). With Gaussian kernel function, the solution of 2D isotropic diffusion equation can be easily given as,

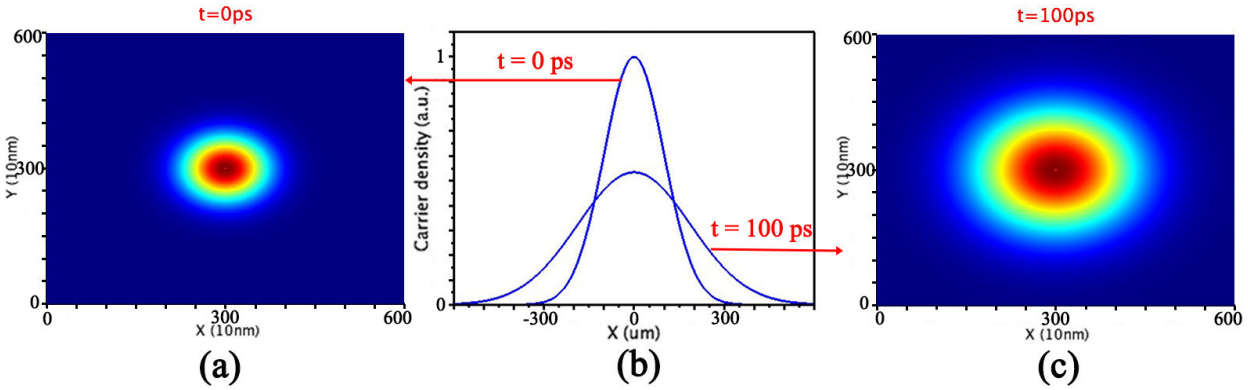

Figure 2.5: (a) Spatial distribution of injected carrier density in $x-y$ when t = 0 ps. (b) Horizontal cross-section of spatial distribution of injected carrier when t = 0 ps and 100 ps. (c) Spatial distribution of injected carrier density in $x-y$ when t = 100 ps.

$$N(r,t) = \frac{N_0 \sigma(0)^2}{4Dt + \sigma(0)^2} e^{-\frac{r^2}{4Dt+\sigma(0)^2} - \frac{t}{\tau}}. \tag{2.40}$$

From the above solution, it can be concluded that the spatial profile of 2D exciton density will remain a 2-dimensional Gaussian distribution during the process of diffusion. What's more, although the total exciton density is no longer conserved because of the exciton recombination, the spatial width of 2D exciton density will not be affected by the following relation,

$$\sigma(t)^2 = \sigma(0)^2 + 4Dt. \tag{2.41}$$

In conclusion, employing the spatial and the temporal scan techniques discussed, the distribution of injected exciton density can be resolved in both space and time. With the temporal scan data, the decay time, τ, of exciton density can be directly fitted by the model of exponential decay function. Furthermore, by fitting the spatial profiles of exciton density with a Gaussian function, the squared $1/e$ half width at various time delay $\sigma(t)^2$ can be obtained. Finally, by plotting the $\sigma(t)^2$ at various delay time t, the slope, the diffusion coefficient D, that is related to the slope, can be further fitted with a linear function.

Diffusion coefficient D and exciton lifetime τ are intrinsic parameters of 2D semiconductors. Other important parameters can also be derived. The exciton diffusion length l_{ex} is calculated as,

$$l_{ex} = \sqrt{D \cdot \tau}. \tag{2.42}$$

With the Einstein relation, the mobility of exciton μ can be derived by,

$$\frac{D}{\mu} = \frac{k_B T}{e}, \tag{2.43}$$

where e is elemental charge.

Chapter 3

Transient absorption microscopy

3.1 Spatiotemporal scan in transient absorption microscopy

To resolve the 2D excitons in both time and space, we have implemented a nonlinear optical spectroscopy named as transient absorption microcopy. One typical experimental setup of transient absorption microscopy from the ultrafast laser lab of KU is shown in Figure 3.1, which detects the differential reflections of the probe laser. In a regular setup, mode-locking of a Ti: sapphire oscillator will yield a train of femtosecond laser pulses with a repetition frequency $f \approx 80$ MHz. The output power of Ti: sapphire oscillator is about 2 W and the pulse width is about 100 fs with a tunable wavelength range from 750 nm to 850 nm. A small part of the output beam from Ti: sapphire oscillator is picked up by a beamsplitter placed between the Ti: sapphire oscillator and an optical parametric oscillator (OPO), which is sent to the probe path. The majority of the output beam from Ti: sapphire oscillator is delivered to the OPO, which generates a signal output in the wavelength range from 1000 nm to 1600 nm, with the same repetition frequency as the Ti output and a pulse width of about 150 fs. The output power of OPO is smaller than 300 mW. A β-Barium borate (BBO) crystal converts the signal output of OPO by second harmonic generation to the wavelength range from 500 nm to 800 nm, which will be sent to the pump path.

Pump and probe paths are constructed on a stable optical-table by various optical-components, such as silver mirrors, pinholes, lens, mechanical mounts and so on. By two beamsplitters, pump

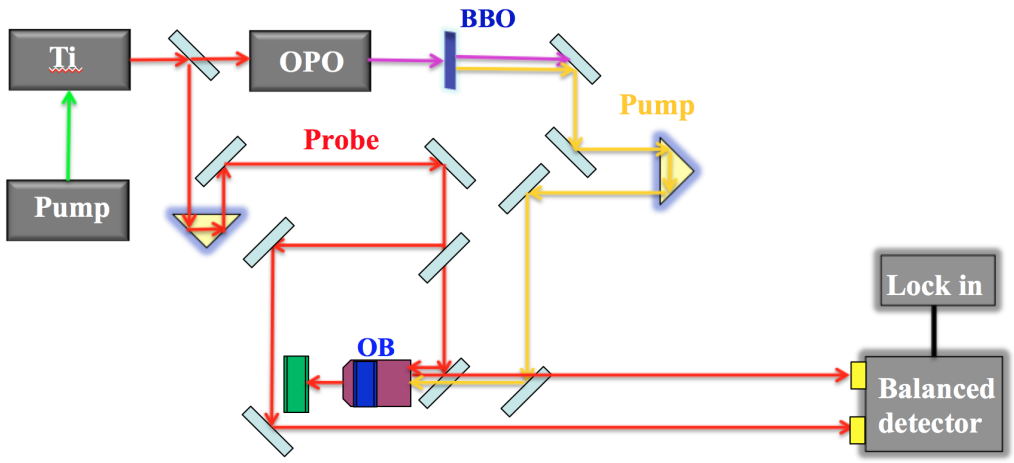

Figure 3.1: Layout of transient absorption microscopy.

and probe beams are finally combined and sent to an objective lens (OB). Tightly focusing conditions of both pump and probe beams on the sample are maintained by choosing an OB with relatively high numerical aperture. The reflected probe beam from the sample surface will be recollected by the OB and sent to a silicon detector, which will convert the optical power of probe beam to electrical signals. To cancel the fluctuations of probe path, balanced detection is employed. To increase the signal-to-noise ratio, lock-in detection technique is applied. The modulation of lock-in detection is accomplished by chopping the pump beam with a mechanical chopper with a frequency range from 1 kHz to 3 kHz. The time interval of pump (probe) pulse train can be calculated as: $t_{int} = 1/f \approx 12.5$ ns. Hence, the distance interval of pump (probe) pulse train is $\Delta L = c \cdot t_{int} = 3.75$ m. The optical lengths of both pump and probe paths are constructed to be reasonably close, enabling pump and probe pulses reach the sample approximately at the same time. The optical length of probe path is controlled by a linearly mechanical delay stage. The probe beam makes a round trip by a retro-mirror fixed on the delay stage. By scanning the retro-mirror, the time delay between pump and probe pulses can be controlled.

The photon energy of pump laser is usually higher than the band gap so that electron will be excited from valence band to conduction band through one-photon absorption. Excitons can be accordingly formed in sub-picosecond timescale followed by the pump pulse. To resolve dynamics

of injected excitons, the photon energy of probe laser is tuned to be close to the band gap of excitons. Since the reflection coefficient of probe laser depends on the injected exciton density, the temporal dynamics of excitons can be resolved by measuring $\Delta R/R_0$. The differential reflection is defined as the normalized change of the probe reflection induced by the pumps, $\Delta R/R_0 = [R(N) - R_0]/R_0$, where $R(N)$ and R_0 are the reflectance of the probe by the sample with and without the presence of the pump pulse, respectively.

To observe the spatial dynamics of injected excitons, we scan the probe laser spot across the pump spot on the sample by tilting the beamsplitter before the objective lens (OB), as shown in Figure 3.1. This is facilitated by a picomotor system. The injected density of excitons on the sample plane will be Gaussian. Soon after injection, the excitons will diffuse so that the size of the measured profile of injected excitons will expand in the real space as a function of time. Combining with the temporal scan, spatiotemporal dynamics of injected excitons can be resolved. As we have showed in Chapter 2, this process can be modeled with the diffusion equation and simplified to the solution: $\sigma^2(t) = \sigma^2(0) + 4Dt$, where D and $\sigma(0)$ are the diffusion coefficient of excitons and the $1/e$ half width of the initial spatial profile at $t = 0$. In addition, according to Einstein relation $D = \mu k_B T/e$, where k_B and T are Boltzmann constant and temperature, we can further calculate the exciton mobility μ and other intrinsic parameters of the 2D material.

3.2 Exciton dynamics in bulk and monolayer WSe_2

Tungsten diselenide (WSe_2) is an important member of transition metal dichalcogenides, with layered crystal structure and stable chemical properties in ambient conditions. Monolayer WSe_2 has a hexagonal lattice structure. Photoluminescence measurements have confirmed an indirect-to-direct band gap transition in monolayers [77]. Its optical responses are dominated by two exciton transitions at 1.71 and 2.30 eV, known as A nd B excitons [78–80], respectively.

WSe_2 has been widely used as electrodes in photoelectrochemical solar cells [81–83] and hydrogen evolution [84], due to its high optical absorption coefficients in visible range and its resistance to photocorrosion. With the layered crystal structure, WSe_2 is flexible and has very low

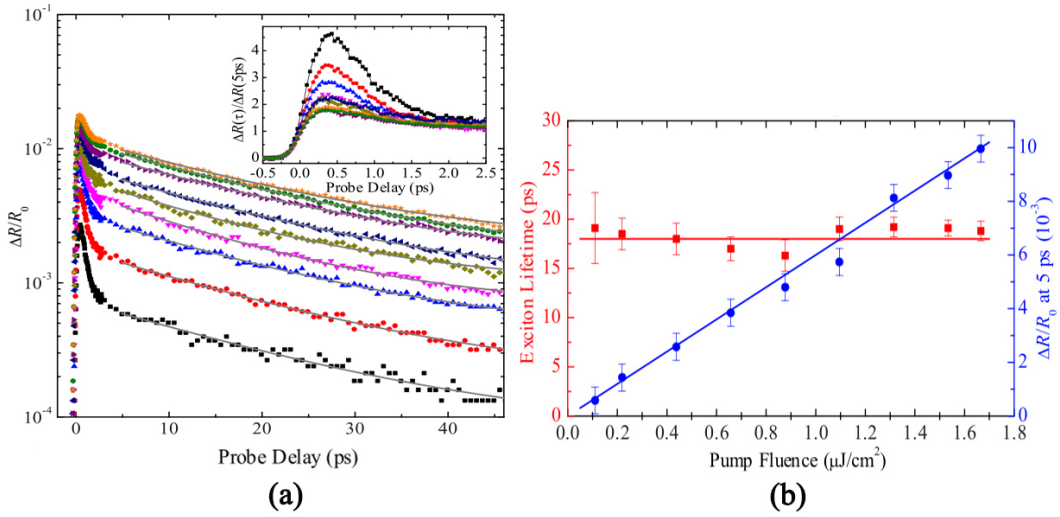

Figure 3.2: (a) Differential reflection of a 750 nm probe as a function of the probe delay in monolayer WSe_2 measured with a 405 nm pump of energy fluences of (from bottom) 0.11, 0.22, 0.44, 0.66, 0.88, 1.10, 1.31, 1.54, and 1.66 μJ cm^{-2}. The inset shows the signal at early probe delays. (b) The exciton lifetime (red squares, left axis) and the magnitude of the signal at a probe delay of 5 ps (blue circles, right axis) as a function of pump fluence. Data from Cui et al [97].

surface trap density, making it a promising candidate for flexible electronics. Actually, ultrathin films containing only two layers of WSe_2 have been successfully produced by mechanical exfoliation in 1970, and the thickness effect on the exciton transitions has been revealed [85]. In a recent study, field effect transistors based on single crystal WSe_2 have been demonstrated, and carrier mobilities were found to be comparable to silicon at room temperature [86]. First-principles calculations predicted giant spin-orbital-induced spin splittings in monolayer WSe_2 of more than 400 meV [87], which has been experimentally determined to be about 370 meV[43], suggesting potential applications of WSe_2 in spintronics [88–90]. Electric manipulation of spin-valley-coupled photogalvanic current in WSe_2 has been experimentally realized [91]. More interesting, it has been reported that WSe_2 has ultralow thermal conductivity, 100000 times smaller than the best thermal conductor diamond [92].

Besides being a novel 2D material itself, WSe_2 can play important roles in developing van der Waals heterostructures and crystals [50, 93–96]. Therefore, it is important to understand the intrinsic properties of WSe_2. We study the excitonic dynamics in monolayer and bulk WSe_2 by transient absorption microscopy.

The samples (monolayer and bulk WSe_2) are fabricated by mechanical exfoliation onto a silicon substrate with a 280 nm oxide layer. Monolayer sample is identified by the optical contrast under a commercial optical microscope and further confirmed by photoluminescence spectroscopy. In the transient absorption measurements, a 10 W and 532 nm continous laser is used to pump a passively mode-locked Ti: sapphire oscillator that generates 100 fs pulses with a central wavelength of 810 nm at 80 MHz. A small portion of this bean is focused into a beta barium borate (BBO) crystal to obtain 405 nm pulses through efficient second harmonic generation, which is used as the pump laser in the transient absorption. The rest of the 810 nm beam is sent to an optical parametric oscillator to generate a signal output in the range of 1400-1580 nm. Second harmonic of the signal output is used as the probe laser. Both pump and probe lasers are tightly focused on the samples by an objective lens. The reflected probe laser is delivered to a detector. Balance detection and lock-in detection techniques are employed to increase the signal-to-noise ratio. A modulation frequency of about 2 kHz is applied by chopping the pump beam with a mechanical chopper.

In our experiments, the excitons in WSe_2 are injected by a 100 fs pump laser pulse and are detected by measuring the differential reflection of a probe laser pulse, which is the relative change of the probe reflection induced by the pump pulse. To obtain the spatiotemporal dynamics of excitons, the differential reflection is measured as a function of the probe delay time, probe wavelength, and the spatial overlap between the probe and the pump laser spots focusing on samples. All measurements are taken in ambient conditions with no signs of sample variation observed during the whole investigation.

To obtain the lifetime of injected excitons in the monolayer WSe_2, we carry out temporal scans of differential reflection. The probe laser is fixed at 750 nm, which is close to $1s$ resonance of the A-excitons. Figure 3.2 (a) shows the differential reflection signal of the monolayer sample as a function of pump pulse fluence. The inset shows the short range scans with respect to the relatively long range scans in Figure 3.2 (a). The decay curves are consist of a fast and a low decay components. From the short range scans in the inset, the fast decay component is shorter

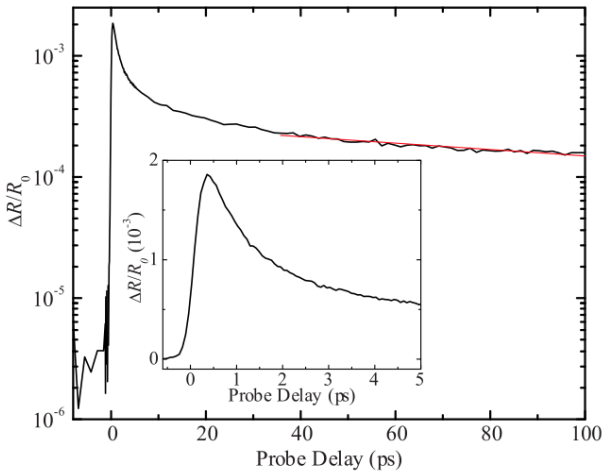

Figure 3.3: Differential reflection of the 750 nm probe as a function of the probe delay in bulk WSe_2 measured with a 405 nm pump fluence of 0.3 μJ cm^{-2}. The red line is an exponential fit. The inset provides a closer view over the early probe delays. Data from Cui et al [97].

than 5 ps, which can be attributed to hot carrier relaxation, since the photon energy of our pump pulse is much higher than the band gap, and hence carriers are injected with large kinetic energies. To obtained the lifetime of excitons, we fit the slow decay component after 5 ps with a single exponential model, as shown with the gray curves in Figure 3.2 (a). The slow decay of differential reflection signals can be attributed to the loss of exciton population due to their recombination. The fitted lifetimes of excitons (red squares) are plotted in Figure 3.2 (b), indicating the lifetime is independent of pump fluence. To convert the pump fluence to the injected exciton density, we use bulk absorption coefficient of 0.5×10^{11} cm^{-1}, as previously reported [78], and assume that every pump photon absorbed excites one exciton. We find that the largest pump fluence used (1.66 μJ cm^{-2}) corresponds to an areal exciton density of about 1.0×10^{11} cm^{-2}, or an average distance between excitons of about 31 nm. In such a low density regime, it is reasonable that exciton-exciton interaction does not influence the exciton dynamics. An averaged value of the lifetime of 18 ± 1 ps is obtained as shown in Figure 3.2 (b). A linear dependence of differential reflection signals at 5 ps as a function of pump fluence is shown in Figure 3.2 (b), which further confirms the validity of using the differential reflection signal to monitor the exciton density. For comparison, we study a thick flake on the same substrate that is fabricated from the same crystal. Its thickness

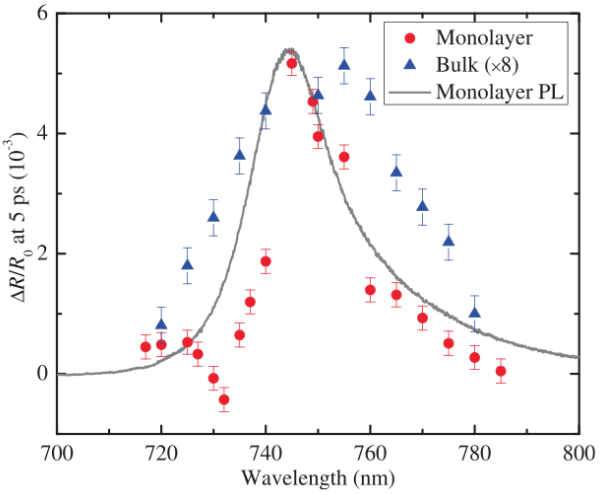

Figure 3.4: Differential reflection signals as a function of the probe wavelength measured in the monolayer (red circles) and bulk (blue triangles, multiplied by 8) WSe_2 samples. The 405 nm pulse has a fluence of 0.7 μJ cm^{-2} and arrives 5 ps before the probe pulse. The gray line shows the PL spectrum of the monolayer sample (in arbitrary units). Data from Cui et al [97].

is not accurately determined; however, it is not transparent for visible light. Hence, it is at least several 10 nm thick and can be treated as a bulk sample. Under the same experimental conditions, the temporal dynamic of the bulk sample with a pump fluence of 0.3 μJ cm^{-2} is shown in Figure 3.3. A similar fast decay component is observed, followed by a much slower decay component. An exponential fit (red line) gives a decay constant of 160 $\pm$ 10 ps, which is a factor of 8 longer than monolayer. The enhanced exciton recombination in monolayer here is consistent with recent PL measurements that showed much higher PL yield in monolayer WSe_2 than few-layer and bulk samples [77, 98, 99].

With a fixed 405 nm pump fluence of 0.7 μJ cm^{-2}, we measure the differential reflection of the monolayer sample as a function of the probe delay with various probe wavelengths. The same temporal dynamics are observed. The red circles in Figure 3.4 show the magnitude of differential signal at a fixed probe delay of 5 ps, together with a PL spectrum of the monolayer sample (the gray line) measured under the excitation of a 632.8 nm He-Ne laser beam. We find that on the long-wavelength side of the PL peak, the differential reflection spectrum agrees very well with the PL line shape, which reflects the A-exciton resonance. However, on the short-wavelength side, there

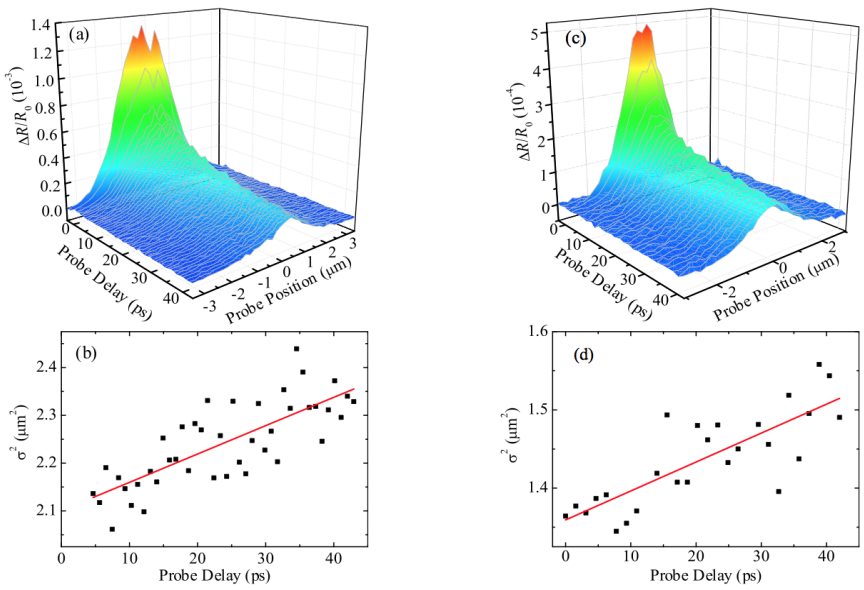

Figure 3.5: Spatiotemporal dynamics of exciton in monolayer (a) and bulk (c) WSe_2. The deduced squared width of each differential reflection spatial profile as a function of the probe delay in monolayer (b) and bulk (d) WSe_2. The red lines indicate linear fits. Data from Cui et al [97].

appears to be negative component that is superimposed to the resonance. In a small wavelength range around 730 nm, the signal becomes negative. In general, the transient absorption on exciton resonances in semiconductors can be induced by several mechanisms, such as phase-space state filling [75], screening of the Coulomb interaction [75], and band gap renormalization [100]. The phase-space state filling effect reduces the exciton transition strength, while the other two effects cause the exciton transition to shift and broaden. Our results indicate that on the long-wavelength side the effect is predominately phase-space state filling, while on the short-wavelength side, other mechanisms are also involved. We also measure the transient absorption spectrum of the bulk sample under the same conditions. The results are shown as the blue triangles in Figure 3.4. Compared to the PL of monolayer, the peak is broader and is slightly shifted to longer wavelength. The negative component in the short-wavelength side is not seen.

To evaluate the diffusive transport properties of excitons in WSe_2, we spatially and temporally resolve the differential reflection signal. The data of spatiotemporal dynamics in monolayer and bulk WSe_2 is shown in Figure 3.5 (a) and (c), respectively. We fit the spatial profiles at various delay time with Gaussian functions. With the diffusion model discussed in Chapter 2, we fit

the squared widths as a function of time with a linear function as shown in Figure 3.5 (b) and (d) for monolayer and bulk sample respectively, so that the exciton diffusion coefficients can be deduced by the slopes. With the diffusion coefficients, the corresponding mobility is obtained. In monolayer WSe_2, the exciton diffusion coefficient and mobility are about 15 cm^2s^{-1} and 600 $cm^2V^{-1}s^{-1}$, respectively. In bulk WSe_2, the exciton diffusion coefficient and mobility is about 9 cm^2s^{-1} and 350 $cm^2V^{-1}s^{-1}$, respectively. Larger mobility in monolayer WSe_2 indicates better transport property than bulk WSe_2.

For electronic applications, charge transport, instead of exciton transport, dominates device performances. Previously, charge transport was studies in field-effect transistors made of ultra-thin WSe_2 films. An electron mobility of 200 $cm^2V^{-1}s^{-1}$ and a hole mobility of 250 $cm^2V^{-1}s^{-1}$ of monolayer WSe_2 were deduced from these measurements [101, 102]. Since excitons are neutral particles, their interactions with charged impurities and piezoelectric types of phonons are expected to be weaker than the charge carriers. Hence, it is reasonable that exciton mobility is larger than the charge mobilities. We note that the all-optical approach used here is free of device fabrication and, hence, avoids any potential complications caused by the quality of the devices and the contacts.

3.3 Transient absorption study of TiS_3 nanoribbons

The measuring ability of transient absorption microscopy is not limited to visible region and TMDs. For 2D semiconducting materials with near-infrared excitonic resonances such as transition metal trichalcogenides, transient absorption microscopy can still be employed as a powerful tool to resolve the spatiotemporal dynamics of excitons. Transition metal trichalcogenides (TMTs), MX_3 (where M=Ti, Zr, Hf, Nb, Ta and X=S, Se, Te), can offer complementary electronic and optical properties of TMDs but are still largely unexplored [103]. TiS_3 is one of the first members of TMTs that started gaining attention due to its low cost production from earth abundant elements. A TiS_3 crystal is composed of parallel sheets of chains of stacked triangular prisms that are held by van der Waals forces. *Abinitio* calculations show that the TiS_3 monolayer is a direct-gap semiconductor with a band gap of 1.02 eV [104, 105] and with an exceptionally high in-plane

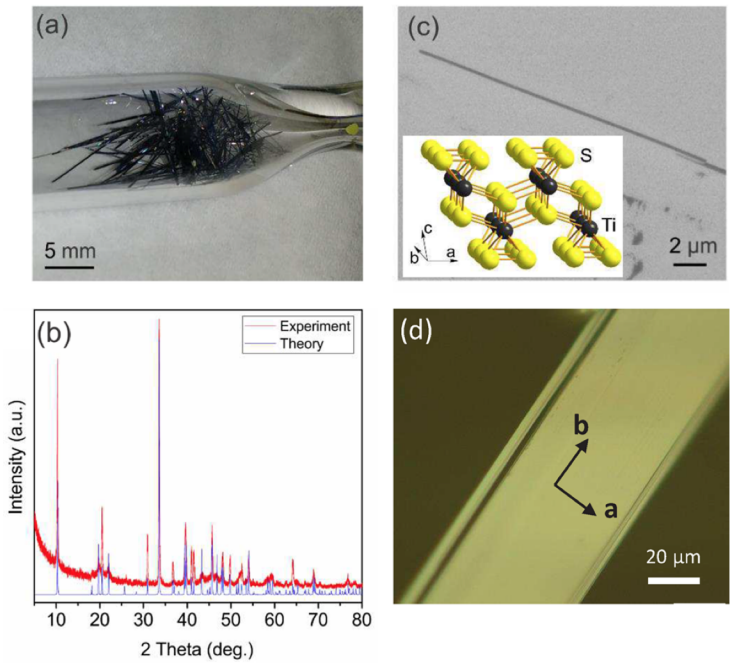

Figure 3.6: Synthesis and characterization of TiS_3 crystals. (a) A picture of TiS_3 single crystals formed on the walls of a quartz ampule. (b) Powder X-ray diffraction pattern for TiS_3 phase (blue). (c) Scanning electron microscopy image of a mechanically exfoliated TiS_3 crystal on the Si/SiO_2 substrate. The crystal structure of TiS_3 and the principal crystallographic directions are shown in the inset. (d) Optical microscopy image of a TiS_3 nanoribbon along the ***b*** direction. Data from Cui et al [113].

electron mobility of about 10000 $cm^2V^{-1}s^{-1}$ [104, 106]. Experimentally, TiS_3 nanoribbons have been synthesized [107–110] and used to fabricate field-effect transistors with room temperature electron mobilities in the range of 1-40 $cm^2V^{-1}s^{-1}$ [107–109] and ultrahigh photoresponse in the entire visible range [109]. Higher electron mobilities of about 70 $cm^2V^{-1}s^{-1}$ was achieved in TiS_3 nanosheets, too [107]. Scanning tunneling spectroscopy and photoelectrochemical measurements showed that TiS_3 nanoribbons have a band gap of 1.2 eV and an exciton binding energy of 0.13 eV, respectively [110]. Applications of TiS_3 as an electrode material for Li batteries [111] and for hydrogen generation [112] have been investigated.

Due to the large binding energy, excitons are the primary form of photoexcitations and are stable at room temperature. Hence, they are expected to dominate optical responses of TiS_3 nanoribbons. Understanding their properties, especially dynamical properties, is necessary for developing novel optoelectronic applications based on this material.

TiS_3 nanoribbon samples were provided by our collaborators from University of Nebraska-Lincoln [108]. These nanoribbons were grown by using a combination of titanium foil of about 0.2 g with excess elemental sulfur of about 0.5 g. The mixture was sealed in a quartz ampule at a pressure of about 200 mTorr and annealed in a furnace at 500 °C for 4 days. Figure 3.6 summarizes material characterization of TiS_3 samples. Shiny black TiS_3 whiskers were formed both on Ti foil and on the walls of the ampule, see Figure 3.6 (a). The crystals grown on the walls were isolated and characterized by powder X-ray diffraction, as shown in Figure 3.6 (b). Cell parameters of TiS_3 phase, extracted from the X-ray diffraction pattern, are consistent with those reported earlier (a = 0.4969, b = 0.3397, c = 0.8797 nm, and β= 97.23°). The lattice structure and the three principal crystalline directions are illustrated in the inset of Figure 3.6 (c). No signatures from additional phases, such as TiS_2 and TiO_2, were observed from the X-ray diffraction, which confirms the purity of the sample. For scanning electron microscopy (SEM) characterization, the samples were mechanically exfoliated onto a Si/SiO_2 substrate. A representative SEM image of an exfoliated TiS_3 nanoribbon, which is less than 1 μm wide, is shown in Figure 3.6 (c). For optical measurements, we typically used wider nanoribbons to avoid possible edge effects.

In the transient absorption setup, the 532 nm output of a diode laser was used to pump a Ti: sapphire laser, which generate 150 fs pulses with a central wavelength of 790 nm. A beamsplitter was used separate it to two beams. By focusing one of the beams to a BBO crystal, we generated its second harmonic at 395 nm, which was used as a pump. The other 790 nm beam was coupled to a photonic crystal fiber to generate supercontinuum. A bandpass filter with a passing wavelength of 950 nm and a bandwidth of 10 nm was employed to select a 950 nm pulse from the supercontinuum, which serve as the probe. A half-wave plate and a polarizer were used to control the polarization and power of each beam. The pump and probe were linearly polarized along perpendicular directions. A dichroic beamsplitter was used to combine the pump and probe beams, which were both focused to the sample by a microscope objective lens. The reflected probe pulse from the sample was sent to a silicon photodetector, which was connected to a lock-in amplifier. The pump pulse was modulated by a mechanical chopper at about 2.2 kHz. The sample was fixed

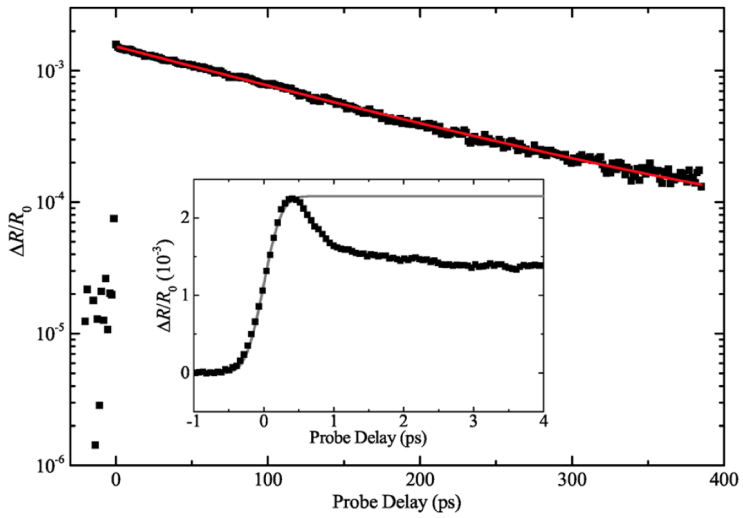

Figure 3.7: Differential reflection signal of a 950 nm probe pulse as a function of the probe delay after the samples is excited by a 395 nm pump pulse. The red curve is a single-exponential fit with a time constant of 140 ps. The inset shows the signal at early delays. The gray curve is the integral of a Gaussian function with a width of 0.47 ps. Data from Cui et al [113].

on a 3-dimensional translation stage. With the assistance of an imaging system, the laser spots were located at the central regions of TiS_3 nanoribbons to avoid edge effects. All measurements were performed at room temperature.

Transient absorption measurements were performed on a number of TiS_3 nanoribbon samples, with similar results obtained. Here, we will present results from one sample shown in Figure 3.6 (d). The thickness of this sample is about 3 μm, determined by atomic force microscopy measurements. Electron-hole pairs are excited by a 395 nm (3.14 eV) pump pulse with a time duration of about 200 fs. The dynamics of these photocarriers are monitored by measuring differential reflection of a probe pulse of 950 nm and 300 fs.

Figure 3.7 shows the measured differential reflection signal as a function of the probe delay. In this measurement, the pump pulse with an energy fluence of 4 μJ cm^{-2} injects a peak photocarrier density (at the center of the pump spot) near the sample surface of about 8×10^{17}cm^{-3}, which is estimated by using an absorption coefficient of 1×10^7 m^{-1} and a reflectance of 0.1 at the pump wavelength [114]. As shown in the inset of Figure 3.7, the differential reflection signal rapidly reaches a peak after the excitation of the pump pulse. The gray curve is the integral of a Gaussian

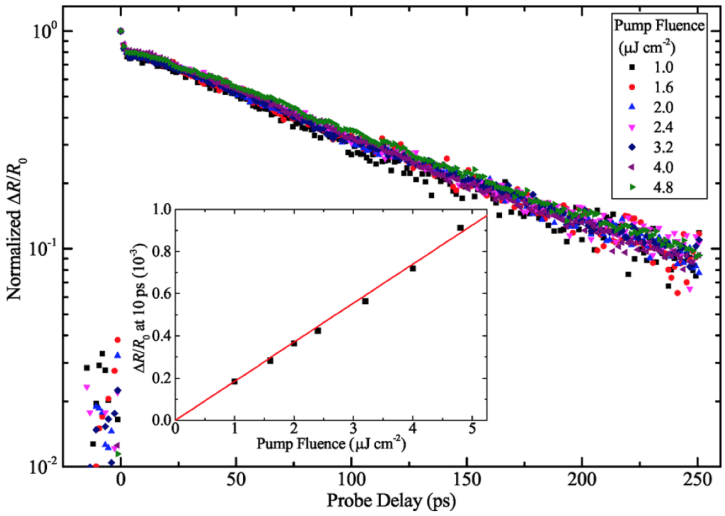

Figure 3.8: Normalized differential reflection signal of a 950 nm probe pulse as a function of the probe delay after the sample is excited y a 395 nm pump pulse. The values of the pump fluence are indicated in the label. The inset shows the magnitude of the signal, reflected by the signal at a probe delay of 10 ps, as a function of the pump fluence .The red line shows a linear fit. Data from Cui et al [113].

function with a width of 0.47 ps (full width at half-maximum). This is close to the response time of the setup. After a sub-picosecond drop, the signal decays single-exponentially, with a time constant of 140 $\pm$ 5 ps, as indicated by the red curve in the main panel of Figure 3.7.

To understand the observed dynamics, we note that with a band gap of 1.2 eV [110], the 3.14 eV pump injects electron-hole pairs with excess energies of about 1 eV, while the 1.3 eV probe predominately senses carrier populating states that are about 50 meV above the bandedges and excitons. The electrons and holes are injected with a narrow Gaussian energy distribution, dictated by the spectrum of the pump pulse. This distribution evolves to a Fermi-Dirac distribution in a thermalization process, achieved by exchange of energy among the carrier via carrier-carrier scattering. Then, the hot carriers will relax their energy to reach quasi-equilibrium with the lattice at 300 K. This energy relaxation is achieved by emission of phonons. Both the thermalization and energy relaxation involve movement of carriers into the probing window and hence should cause an increase in the differential reflection signal. The lack of a resolvable rising part suggests that these processes are completed on a time scale faster than 0.5 ps.

The thermalized and cooled electron-hole pairs are expected to form excitons. Since the exciton

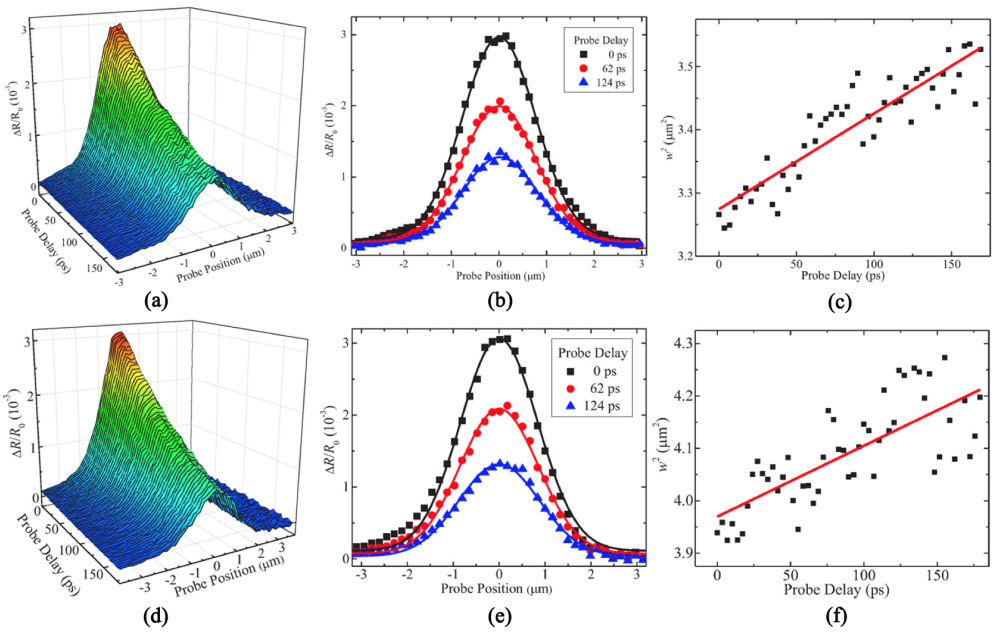

Figure 3.9: When the probe spot is scanned along $\boldsymbol{b}$: (a) Differential reflection signal as a function of both the probe delay and the probe position. (b) Spatial profiles at the probe delay of 0, 62, and 124 ps. (c) Squared width of spatial profile as a function of probe delay. The red line is a linear fit. When the scanning direction of probe spot is perpendicular to $\boldsymbol{b}$, results are illustrated in (d), (e) and (f) in the same fashion. Data from Cui et al [113].

binding energy [110] of 0.13 eV is much larger than thermal energy at 300 K, once formed, excitons are expected to be stable and decay due to radiative or nonradiative recombination. The small drop right after the peak observed in the inset of Figure 3.7 could be associated with the exciton formation, since in this process the carriers are moving out of the probing window. The excitons can induce a differential reflection signal for the probe tuned above the band edge due to the phase-space state filling effect, since the exciton states are formed by superposition of all free carrier states [75]. Hence, the occupation of an exciton state influences excitation of other free carrier states. However, if the excitons are less efficient in including the signal than free carriers of the same density, the signal is expected to decrease as the free carriers form excitons.

Next, we repeat the measurement with various values of the pump fluence, that is, injected carrier density. As shown in Figure 3.8, the decay of the signal is independent of the pump fluence. The magnitude of the signal is proportional to the pump fluence, as indicated in the inset. Therefore, exciton-exciton annihilation is absent under the experimental conditions we applied.

Otherwise, the decay is expected to be faster at higher densities [115–119].

To study the in-plane transport property of excitons, we perform spatial scans of probe focus spot over the pump spot on the sample at various probe delay time. Figure 3.9 (a) shows the differential reflection signal as a function of both the probe delay and the probe position (the distance between the centers of the pump and probe spot). Here, the probe spot was scanned along the vertical direction in lab coordinate, while the sample is oriented such that the $\boldsymbol{b}$ direction is vertical. At each probe delay, the spatial profile of the differential reflection is proportional to the spatial profile of the excitons along $\boldsymbol{b}$. Figure 3.9 (b) shows a few examples these profiles obtained at several different probe delays. By fitting these profiles with a Gaussian function, we deduce the squared width (full width at half-maximum), which is plotted as a function of the probe delay in Figure 3.9 (c).

The broadening of the profile observed in Figure 3.9 (c) originates from the diffusion of excitons along $\boldsymbol{b}$. As shown in Figure 3.8, decay of the differential reflection signal is independent of the exciton density. Hence, different parts of the profile decay at the same rate, and the exciton recombination only causes reduction of the height of the spatial profile, without changing the width. On the other hand, diffusion of excitons would broaden the profiles. From a linear fit (red line) based on the diffusion model discussed previously, we obtain a diffusion coefficient of 1.2 $\pm$ 0.2 $\mathrm{cm^2 s^{-1}}$. To study the exciton diffusion perpendicular to the $\boldsymbol{b}$ direction, the measurement was repeated by scanning the probe spot along the horizontal direction. The results are summarized in Figure 3.9 (d), (e) and (f). A similar exciton diffusion coefficient of 1.0 $\pm$ 0.3 $\mathrm{cm^2 s^{-1}}$ was obtained. For a thermalized particle system, the diffusion coefficient is related to the mobility, μ, by the Einstein relation, $D/k_bT = \mu/e$, where e, k_b and T are elementary charge, Boltzmann constant, and the temperature of the distribution, repectively. The measured diffusion coefficient corresponds to an exciton mobility of about 50 $\mathrm{cm^2 V^{-1} s^{-1}}$. Recently, charge mobilities in the range of 20 to 70 $\mathrm{cm^2 V^{-1} s^{-1}}$ were deduced from transport measurements [107–109]. Although excitons and change carriers interact with their environments differently, the order-of-magnitude agreement of these mobilities is satisfactory. Furthermore, by using the measured exciton lifetime

of τ = 140 ps, we deduce an exciton diffusion length of $\sqrt{D\tau}$ = 130 nm.

3.4 Anisotropic exciton transport in monolayer ReS_2

The four mainly studied TMD monolayers, MoS_2, $MoSe_2$, WS_2 and WSe_2, belong to $1H$ symmetry, which makes the transport properties of them all in-plane isotropic. To develop van der Waals heterostructures with anisotropic properties, a TMD monolayer with large in-plane anisotropy is highly desirable. Hence, we cast the light to monolayer ReS_2, which is a rarely explored TMDs member. Bulk ReS_2 is a semiconducting TMD with a room-temperature band gap of about 1.5 eV, an absorption coefficient of about 8×10^6 cm^{-1} in visible range, an exciton binding energy of about 30 meV, and room-temperature charge mobilities of about 20 $cm^2V^{-1}s^{-1}$ [120–125]. Unlike other TMDs, ReS_2 forms a stable distorted $1T$ structure with triclinic symmetry [126–129]. Due to the lower lattice symmetry, bulk ReS_2 processes in-plane anisotropic optical [124, 130]and transport properties [129]. Hence, monolayer ReS_2 can potentially offer anisotropic optical and transport properties to TMD family. In recent years, monolayer ReS_2 samples have been fabricated by mechanical exfoliation [126, 131], liquid exfoliation [132] and CVD [133, 134]. It has been shown that monolayers and bulk ReS_2 have similar bandstructures due to the weak interlayer coupling [126]. However, the electronic and optical properties of monolayer ReS_2 have been largely unexplored.

With transient absorption microscopy, we experimentally measure the spatiotemporal dynamics of charge carriers and excitons in monolayer ReS_2. In our measurements, electron-hole pairs are injected by interband absorption of a pump pulse. Excitons are formed from injected electron-hole pairs and are detected by measuring the differential reflection of a time-delayed and spatially scanned probe pulse. We find that the magnitude of the transient absorption signal depends on the crystalline direction of the sample with respect to the polarization directions of the pump and probe pulses. Both the pump absorption and the probing efficiency were anisotropic. By performing spatially resolved measurements, we find that the exciton diffusion coefficient is also anisotropic. These results establish monolayer ReS_2 as an anisotropic 2D material.

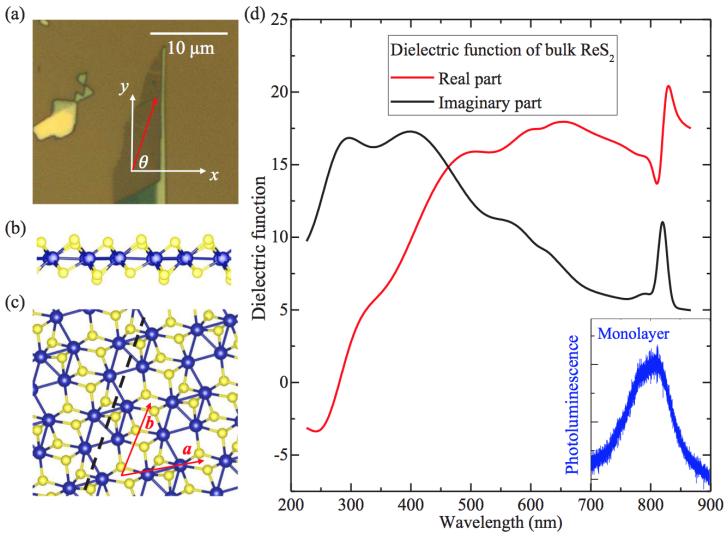

Figure 3.10: (a) The monolayer ReS_2 sample fabricated by mechanical exfoliation. The $x-y$ coordinates represent the laboratory frame. The orientation of the sample with respect to the laboratory is described by the angle θ. (b) The side view of crystal structure of monolayer ReS_2, which contains one Re atomic layer (dark) and two S atomic layers (light). (c) The top view showing the $\boldsymbol{a}$ and $\boldsymbol{b}$ lattice vectors. Zigzag chains of Re atoms are formed along $\boldsymbol{b}$. (d) Complex dielectric function of the bulk ReS_2 crystal obtained by spectroscopic ellipsometry. The inset shows a photoluminescence spectrum of the monolayer sample. Data from Cui et al [135].

A large ReS_2 monolayer, as shown in Figure 3.10 (a), is obtained by mechanical exfoliation. From AFM measurements, the flake has a thickness of about 1 nm, indicating its monolayer nature. Figure 3.10 (b) and (c) show the side and top views of the crystal structure of monolayer ReS_2. The stable crystal structure of monolayer ReS_2 is a distorted $1T$ structure. Its unit cell contains 4 Re and 8 S atoms. Along the $\boldsymbol{b}$ lattice vector direction, Re atoms form zigzag chains, as indicated by the black dashed line in Figure 3.10 (c), due to the Peierls transition. These Re atomic chains break the in-plane hexagonal symmetry, which is expected to introduce in-plane anisotropy. Spectroscopic ellipsometry was used to determine the complex dielectric function of the bulk ReS_2 crystal that was used to fabricate the monolayer. The results are shown in Figure 3.10 (d). The imaginary part shows a pronounced excitonic transition at 820 nm, with a width of about 17 nm. Due to the limited size of the monolayer sample, spectroscopic ellipsometry was not carried out here. Alternatively, we measured the photoluminescense of the monolayer under the excitation of a 405 nm laser. As shown in the inset of Figure 3.10 (d), we observed a peak centered at 800 nm with a width of about

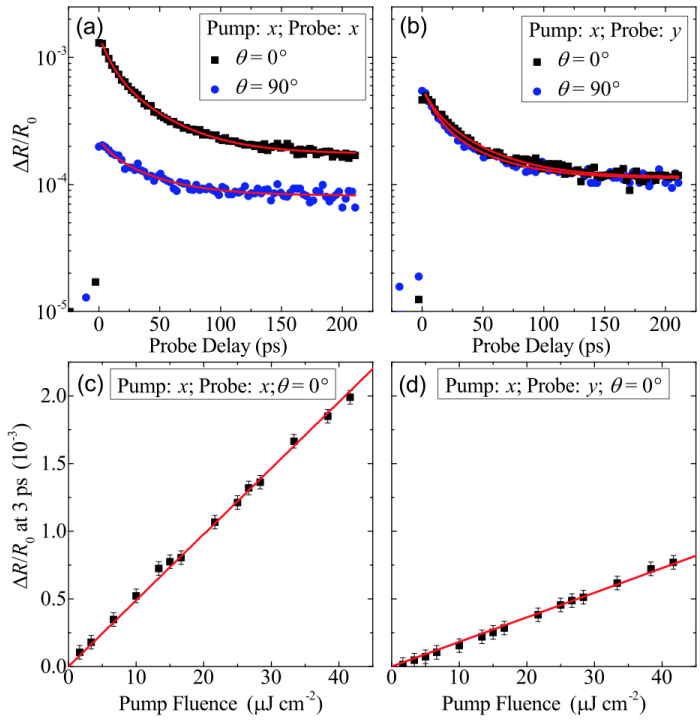

Figure 3.11: (a) Differential reflection signal as a function of the probe delay measured with both pump and probe pulses being polarized along x, and with the angle θ being 0° (squares) and 90°(circles), respectively. The red lines are biexponential functions with two time constants of 10 and 40 ps. (b) Same as (a) except a y-polarized probe is used. (c) Magnitude of the differential reflection signal (represented by the signal measured with a probe delay of 3 ps) as a function of the pump pulse fluence. The pump and probe pulses are both x-polarized and $\theta = 0°$. The red line is a linear fit. (d) Same as (c) except a y-polarized probe is used. Data from Cui et al [135].

80 nm, which is similar to a previously reported result [126].

In our transient absorption measurements, we use a 100 fs and 730 nm pump pulse to excite the sample. The photon energy of the pump pulse is about 150 meV above the photoluminescence peak of the sample. Hence, we expect that the pump pulse excites electron-hole pairs with a large excess energy. It has been well established that the reduced dielectric screening in monolayer TMDs results in significantly enhanced exciton binding energies [136]. Since the exciton binding energy in bulk ReS_2 is about 30 meV, which is above the thermal energy at room temperature, it is reasonable to assume that in ReS_2 monolayers excitons will form from the injected electron-hole pairs, which will be stable at room temperature. The dynamics of the photocarriers and excitons is detected by measuring differential reflection of a time-delayed and spatially scanned probe pulse

of 810 nm, which is near the center of the photoluminescence peak. In all measurements, the pump pulse is linearly polarized along the horizontal direction in the laboratory frame, defined as x in Figure 3.10 (a). The probe polarization is either horizontal or vertical (y). We use the angle (θ) from the $+x$ direction to one of the edges of the flake, indicated as the red arrow in Figure 3.10 (a), to describe the crystalline orientation with respect to the polarizations. By mounting the sample on a rotation stage, θ can be varied with an accuracy of better than 1°.

We first present time-resolved differential reflection with x-polarized pump and probe pulses, and with the sample orientation of $\theta = 0^\circ$, as shown as the black squares in Figure 3.11 (a). Here, the pump fluence is 25 μJ cm^{-2}. By using an absorption coefficient of 8×10^6 m^{-1} (bulk value) [120] and assuming that each pump photon absorbed generates one electron-hole pair, we estimate that an area carrier density of 5×10^{11} cm^{-2} is injected at the center of the pump spot. We found that the signal reaches a peak slightly after zero probe delay, indicating immediate response of the probe to the injected carriers. The decay of the signal can be fitted by a biexponential function (red line), with two time constants of 10 ± 1 and 40 ± 2 ps, respectively. Next, we rotate the sample to $\theta = 90^\circ$ and repeated the measurements. As shown as the blue circles in Figure 3.11 (a), the magnitude of the signal is decreased by about a factor of 7, while the bi-exponential function with the same time constants (red line) can satisfactorily describe the decay of the signal. These two measurements were repeated with a y-polarized probe. The results are shown in Figure 3.11 (b). We found that these two curves have similar magnitudes, both being smaller than $\theta = 0^\circ$ but large than $\theta = 90^\circ$ in the $x - x$ pump-probe configuration. Furthermore, the decay of both curves can also be described by the biexponential function with time constants of 10 and 40 ps (red lines). By repeating the measurements with different values of the pump fluence, and the magnitude of the signal increases linearly with the fluence, as shown in Figure 3.11 (c), (d) for $x - x$ and $x - y$ configurations, respectively.

From these measurements, we conclude that the exciton dynamics observed is independent of the probe polarization and sample orientation. Upon injection, the hot carriers relax their energy and form excitons. In this process, even without carrier and exciton recombination, the differential

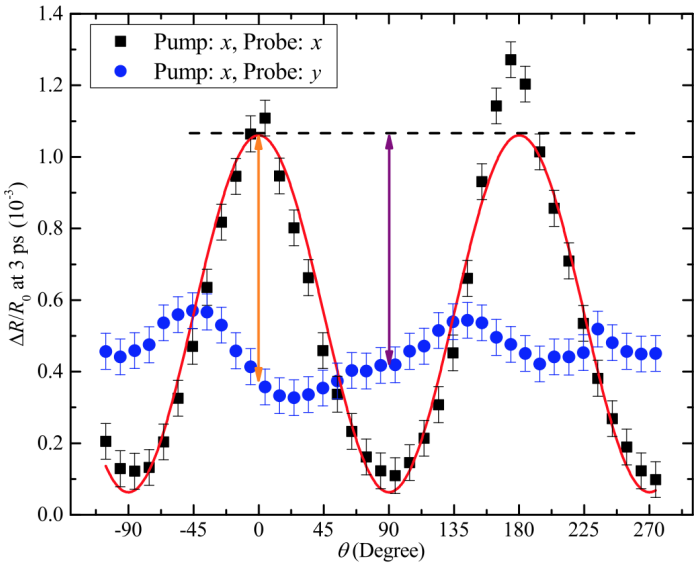

Figure 3.12: Differential reflection signals at a probe delay of 3 ps measured with pump-probe polarizations of $x-x$ (squares) and $x-y$ (circles). The angle θ is defined in Figure 3.10 (a). The red solid line is a fit ($A\cos 2\theta + B$). Data from Cui et al [135].

reflection signal is expected to decrease since free carriers are more efficient than excitons in changing the absorption coefficient at the exciton resonance. Based on this argument, we assign the short time constant of 10 ps to energy relaxation of hot carriers and exciton formation. The long time constant of 40 ps can then be assigned to the lifetime of excitons. Given the extremely low photoluminescence yield of monolayer ReS_2, such a short lifetime is limited by nonradiative recombination of excitons.

To systematically study the anisotropic properties of the differential reflection signal, we repeated these measurements as we varied the angle θ. In these measurements, the pump fluence was kept at 25 μJ cm^{-2}. Figure 3.12 shows the signal with a probe delay of 3 ps as a function of θ for $x-x$ (black squares) and $x-y$ (blue circles) pump-probe polarizations, respectively. A rather large anisotropy was observed on the $x-x$ configuration, where the data can be fitted with $A\cos 2\theta + B$ with $A = 1.0\times 10^{-3}$ and $B = 0.63\times 10^{-4}$. The variation of the data in $x-y$ configuration is smaller.

The angular dependence of the differential reflection can be induced by anisotropic interactions

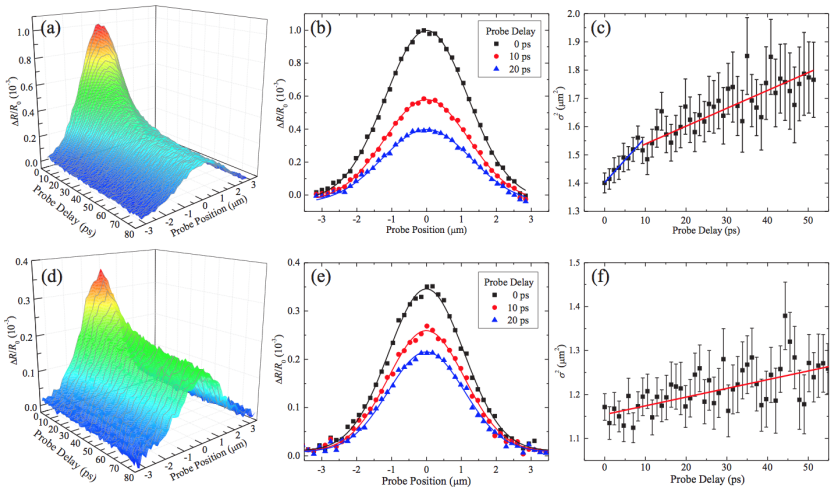

Figure 3.13: (a) Differential reflection signal as a function of probe delay and probe position, as the probe spot is scanned along the ***b*** direction. The pump and probe polarizations are also along ***b***. (b) Spatial profiles of the differential reflections signal at probe delays of 0 (black squares), 10 (red circles), and 20 ps (blue triangles). The solid lines are Gaussian fits. (c) Squared width of the profiles as a function of probe delay. The blue and red lines are linear fits for the time ranges of 0 to 10 ps and 10 to 50 ps, respectively. Panels (d)-(f) are the same as (a)-(c), but with the probe spot scan direction and probe polarization being perpendicular to ***b***. Data from Cui et al [135].

of the sample with both the pump and the probe. To consider the effect of pump, we compare the differential reflection at $\theta = 0^\circ$ of $x-x$ and $\theta = 90^\circ$ of $x-y$ configurations, as shown as the purple double arrow in Figure 3.12. In both cases, the probe polarization is parallel to the direction indicated by the red arrow in Figure 3.10 (a). The only difference is that the pump polarization is parallel ($x-x$, $\theta = 0^\circ$) or perpendicular ($x-y$, $\theta = 90^\circ$) to that direction. From the two signal values of 1.06×10^{-3} and 0.42×10^{-3}, we conclude that the pump polarized along the direction indicated by the red arrow in Figure 3.10 (a) injects a factor of 2.5 higher carrier density than that the pump polarized perpendicular to that direction. That indicates that the absorption coefficient of the sample is anisotropic by that factor, with the maximal absorption occurring when the polarization is along that direction. Early studies have shown that in bulk ReS_2, the absorption coefficient is maximal when the polarization is along the ***b*** direction. Based on this, we can assign the sample direction indicated by the red arrow in Figure 3.10 (a) as the ***b*** direction, that is, the direction of the Re atomic chains.

To understand the anisotropic effects of the probe, we compare the results of $x-x$ and $x-y$ configurations both at $\theta = 0^\circ$, as shown as the orange double arrow in Figure 3.12. In this case, the pump polarization are both parallel to $\boldsymbol{b}$. Hence, they inject the same (and maximal) carrier density. With the signal values of 1.06×10^{-3} (x-probe) and 0.38×10^{-3} (y-probe), we conclude that the probe polarized along $\boldsymbol{b}$ is a factor of 2.8 more efficient in sensing carriers and excitons than that polarized perpendicular to $\boldsymbol{b}$. We note that the anisotropic effects pump and probe have similar magnitudes (2.5 and 2.8, respectively), which is reasonable since they both originate from the interband transition matrix element. The fact that the pump and probe effects both peak along $\boldsymbol{b}$ with similar magnitudes of anisotropy suggests that the variation of signal in $x-y$ configuration should be smaller than $x-x$, as observed in Figure 3.12. Finally, the magnitude of anisotropic effects of pump and probe suggest that in the $x-x$ configuration, the signal at $\theta = 0^\circ$ (where both effects are maximal) should be a factor of 7 larger than $\theta = 90^\circ$ (where both effects are minimal). This is reasonably consistent with the results shown in Figure 3.11 (a) and 3.12.

To measure the diffusion coefficient along the $\boldsymbol{b}$ direction, we rotate the sample so that $\boldsymbol{b}$ is along x, and measure the differential reflection signal as a function of probe delay as we scan the probe spot along x. The pump and probe are both polarized along x, too, with a pump fluence of 36 μJ cm^{-2}. The result of this spatiotemporal scan is shown in Figure 3.12 (a). At each probe delay, the profile is a Gaussian function. A few examples of the profiles are shown in Figure 3.12 (b), with probe delays of 0 (black squares), 10 (red circles), and 20 ps (blue triangles), respectively. By fitting each profile with a Gaussian function, we deduce its $1/e$ half width σ. σ^2 is plotted as a function of probe delay in Figure 3.12 (c). Despite the rather large uncertainties, an expansion of the profile is clearly seen. By fitting the data in the range of 10 - 50 ps (the red solid line), we find a diffusion coefficient of 16 ± 4 cm^{2}s^{-1}.

Next, we study diffusion of excitons along the direction perpendicular to $\boldsymbol{b}$ by rotating the sample by 90° so that $\boldsymbol{b}$ is along y direction. The pump polarization is also changed to y in order to inject the same carrier density. We repeat the measurements described above under otherwise same conditions. The results are plotted in panels (d), (e), and (f) of Figure 3.12 in a similar fashion as

(a), (b), and (c). We find that the diffusion coefficient along this direction is 5 ± 2 cm^{2}s^{-1}, about a factor of 3 smaller than along the $\boldsymbol{b}$ direction.

Based on the diffusion coefficients obtained from these measurements, we can deduce the corresponding exciton mobilities, μ, from the Einstein relation $D = \mu k_B T/e$. Where k_B, T, and e are Boltzmann constant, the temperature, and elementary charge, respectively. We find the mobilities of about 620 cm^{2}V^{-1}s^{-1} along $\boldsymbol{b}$ and about 200 cm^{2}V^{-1}s^{-1} perpendicular to $\boldsymbol{b}$, respectively. Furthermore, we deduce the exciton diffusion lengths ($L = \sqrt{D\tau}$) of about 250 nm along $\boldsymbol{b}$ and about 80 nm when moving perpendicular to $\boldsymbol{b}$, by using the measured exciton lifetime of τ = 40 ps. Similar to the lifetime, this diffusion length is limited by fast nonradiative recombination of excitions. Nevertheless, we find that the value is similar to other TMD monolayers, such as WSe_2 (160 nm) [97], $MoSe_2$ (400 nm) [137], and WS_2 (350 nm) [138].

Chapter 4

Quantum interference and control nanoscopy

In semiconductors, net flow of carriers is called carrier transport, which can be induced by either carrier density gradients or applied electrical fields. In general, collective motions of carriers, such as diffusion and drift, are two basic carrier transport mechanisms [139, 140]. During the transport processes, carriers usually will be scattered by the lattice and impurities of semiconducting materials. As a result, the energy of carriers will be dissipated [140]. However, when the size of a device becomes smaller than the mean free path, the carriers will travel without scattering [141, 142]. This is the ballistic transport. Due to the absence of scattering, ballistic transport of carriers will almost create no heat. In such cases, the carriers will flow like the photons in vaccum. As the size of transistor on a microchip gets extremely small, the performances of electronics devices will be dominated by ballistic transport properties of carriers.

The ballistic transport length is expected to be smaller than the mean free path. The mean free path of carriers in TMDs, such as MoS_2, has been predicted to be about 15 nm at room temperature [143]. Therefore, an ordinary optical measurement is not feasible in the ballistic regime since the spatial resolution is not enough. To solve this problem, a nonlinear optical spectroscopy called quantum interference and control nanoscopy has been developed with a spatial resolution as small

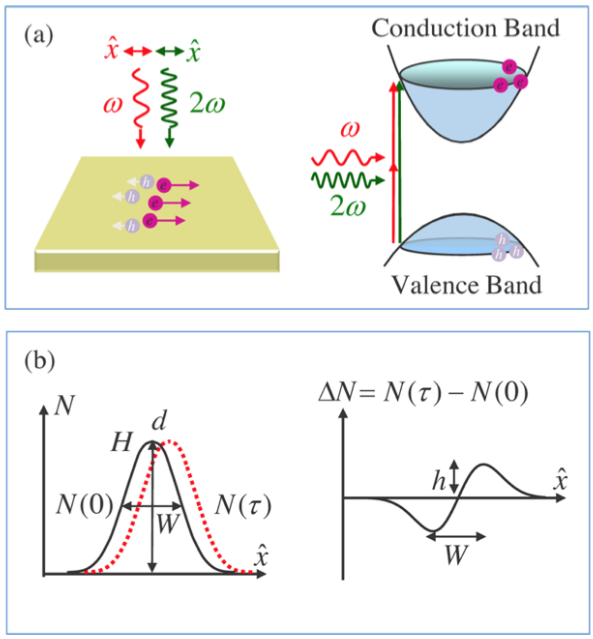

Figure 4.1: (a) The quantum interference between one-photon absorption of the 2ω pulse and two-photon absorption of the ω pulse allows control of the average velocities of the injected electrons and holes. (b) Differential pump-probe scheme to detect nanoscale transport. The initial electron density profile [$N(0)$, solid Gaussian curve] and the profile at a later time [$N(\tau)$, dashed Gaussian curve] are separated by a small distance d. Their difference has a derivative-like profile (ΔN), with a height h that is proportional to d. Data from Cui et al [36].

as 1 nm [144], that is capable of detecting motions of carriers as small as 1 nm. With quantum interference and control nanoscopy, for the first time in TMDs-ReS_2, we have realized the injection, detection and coherent control of nanoscale ballistic currents.

4.1 Quantum interference and control

In our experiment, we use a coherence control technique to inject ballistic currents. This current injection process has been demonstrated in conventional semiconductors, such as Si and GaAs, as well as nanomaterials of carbon nanotubes and graphene. As shown in Figure 4.1(a), a ReS_2 thin film sample is simultaneously illuminated by two 100 fs laser pulses with central wavelengths of 1500 nm (ω) and 750 nm (2ω), respectively. With a photon energy (1.65 eV) higher than the band gap of ReS_2 (about 1.5 eV), the 2ω pulse injects electrons and holes via one-photon

interband absorption (green vertical arrow). Usually, the transition amplitude of this one-photon absorption process, $A_1(\vec{k})$, is an even function of $\vec{k}$, the wavevector of the electrons. Hence, along any direction, an equal number of electrons are injected with opposite $\vec{k}$ values, resulting in no net current. The ω pulse has a photon energy lower than the band gap and can inject carriers only by two-photon absorption (red vertical arrows). Although the transition amplitude of this two-photon process, A_2, is approximately and odd function of $\vec{k}$, the corresponding transition probability, $P_2 = |A_2|^2$, is still an even function of $\vec{k}$. Such a $\vec{k}$-space symmetry can be broken by utilizing the quantum interference effect: When the two transition pathways exist simultaneously, the overall transition probability is,

$$P_{1+2} = |A_1 + A_2|^2 = |A_1|^2 + |A_2|^2 + A_1^* A_2 + A_1 A_2^*. \tag{4.1}$$

The last two terms on the right-hand side are the interference terms and are odd functions of $\vec{k}$. Therefore, in most cases, $P_{1+2}(k) \neq P_{1+2}(-k)$, making coherent control of current injection possible. Specifically, when both pulses are linearly polarized along the same direction, defined as $\hat{x}$, electrons are injected in the conduction band with an average velocity of,

$$\vec{v}_{av} = \eta v \sin(\Delta\phi)\hat{x}, \tag{4.2}$$

where v is the speed of each electron determined by the excitation excess energy and $\Delta\phi = \phi_{2\omega} - 2\phi_{\omega}$ is the relative phase of the two transition amplitude. η is a parameter describing the efficiency of the current injection process. Owing to the crystal momentum conservation, holes are injected in the valence band with an opposite crystal momentum. Once injected, the electrons and holes move oppositely along $\hat{x}$. Without a driving force, this ballistic current is expected to decay quickly, due to phonon and carrier scattering. In addition, the Coulomb force also decelerates the electrons and the holes and eventually pulls them back toward the origin.

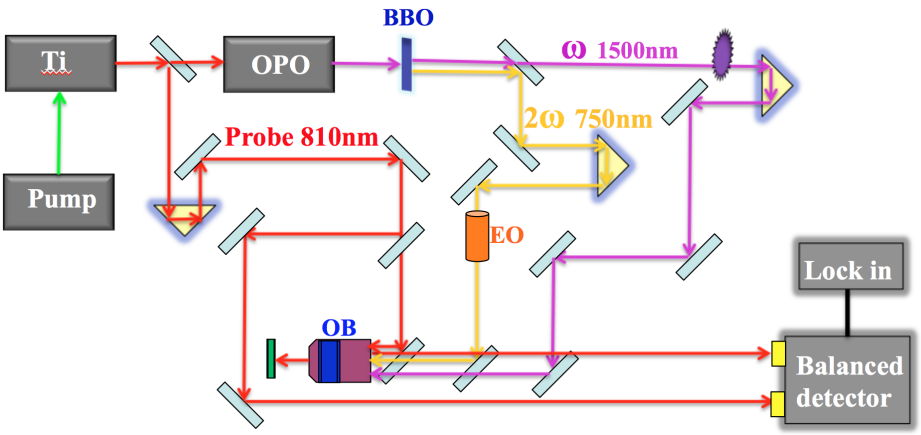

Figure 4.2: Experimental setup of quantum interference and control in ReS_2 thin film

4.2 Differential pump-probe to resolve nanoscale transport

To study ballistic transport, the μm resolution is not enough. We use a new approach, the differential pump-probe technique to solve this problem. As shown in Figure 4.1(b), $N(0)$ is the electron density profile at t=0, with a width W of about 1 μm and a height H. At a later time, the profile $N(\tau)$ moves a small distance d. Such a small distance is hard to measure optically. However, we directly measure the difference between the two profiles, ΔN. It can be viewed as electron accumulation due to the ballistic transport. It has a derivative-like profile, with a height h with respect to the width W. This model can be described by the formula,

$$\frac{L}{W} = 0.707\frac{h}{H}. \tag{4.3}$$

By measuring h, we can accurately determine the transport length d. To measure a distance that is three orders of magnitude smaller than the laser spot, we have to detect a signal three order of magnitude smaller than that in an normal transient absorption measurement. Hence, we are converting a resolution problem to a signal-to-noise ratio (SNR) problem. The smallest ballistic transport distance we can measure will be limited by the SNR.

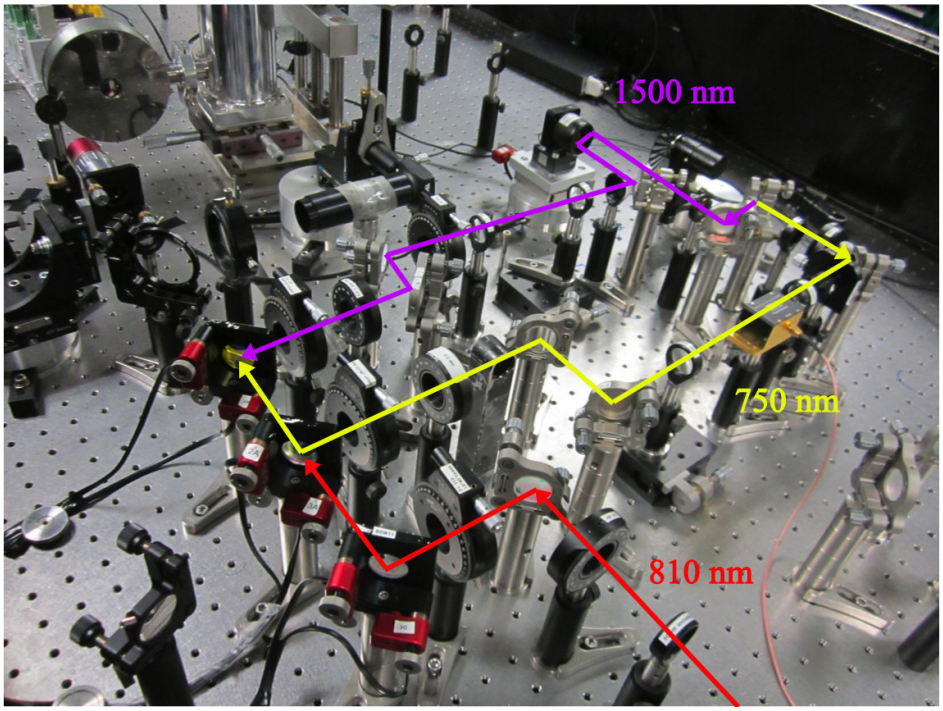

Figure 4.3: The photo of interferometer established for QUIC.

4.3 Experimental setup

Figure 4.2 shows the experimental setup of quantum interference and control (QUIC) in ReS_2 thin film. The probe laser wavelength is 810 nm, which is very close to the band gap of ReS_2. To get the quantum interference, we need two pump laser paths. One path is ω with a wavelength 1500 nm and the other path is 2ω with a wavelength 750 nm, which is generated by second harmonic generation of 1500 nm by a BBO crystal. ω and 2ω are first separated by a beamsplitter and then combined to the objective lens (OB). These two paths, ω and 2ω, form an interferometer, a real photo of which is presented in Figure 4.3. We can precisely control the phase difference of the two paths by a piezo-motor. The high signal-to-noise ratio is obtained by the electrical-optical modulator (EO) and the balanced detection technique. After careful calibrations of the interferometer, all these three ultrafast pulses will be able to overlap precisely in both time and space on the sample.

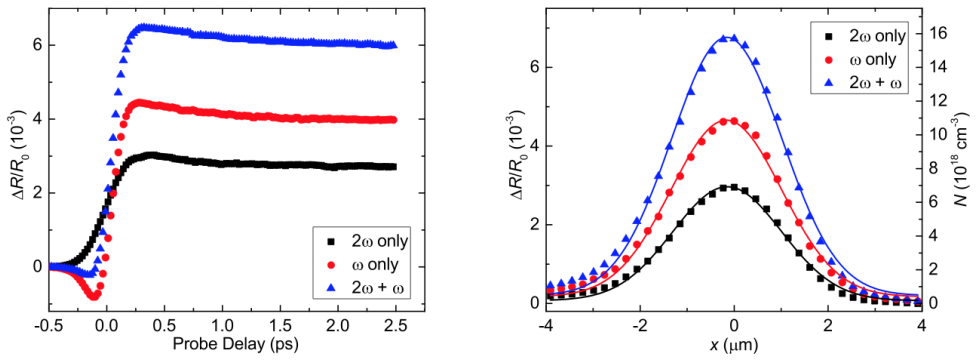

Figure 4.4: Differential reflection (left panel) of the 810 nm probe pulse and spatial profiles (right panel) of the carrier densities induced by the 2ω pump only (black squares), the ω pump only (red circles), and both pumps (blue triangles). Here x = 0 is defined as where the centers of the pump and probe spots overlap with a fixed probe delay of 0.35 ps. Data from Cui et al [36].

4.4 Coherent injection, detection and control of ballistic charge currents in ReS_2

We choose ReS_2, a relatively less studied TMD, in our experiments for several considerations. First, unlike most TMDs, which crystallize in hexagonal phase, ReS_2 forms a stable distorted $1T$ structure with triclinic symmetry [126]. As a consequence, the interlayer coupling in ReS_2 is much weaker than other TMDs, with the adjacent monolayers largely decoupled. Hence, a multilayer ReS_2 behaves like a collection of noninteracting monolayers. This allows us to study multilayer thin film samples, which yield larger signals and still reveal ballistic transport properties of monolayers. Second, the exciton binding energy in ReS_2 is about 30 meV [121], much smaller than other TMDs. This facilitates free carrier transport. Third, due to the unique lattice structure, ReS_2 possesses different properties from other TMDs, such as in-plane anisotropic optical responses [145]. Hence, it can be used to complement other TMDs in various applications, as we have discussed in Chapter 3.

We investigated two ReS_2 samples with thickness of 15 nm and 18 nm, respectively. Similar results were obtained. Here, we only present the results from the 15 nm sample [36]. First, we carry out the differential reflection measurements to confirm all three laser pulses can overlap in time, after calibrating the interferometer with GaAs. A peak pump fluence dependence with only

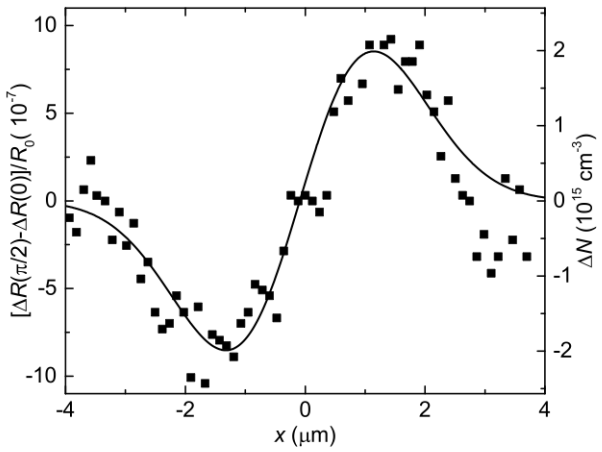

Figure 4.5: Transport-induced electron accumulation (right axis) deduced from the measured difference between the differential reflection signals (left axis) with $\Delta\phi = \pi/2$ and $\Delta\phi = 0$. The probe delay is 0.35 ps. Data from Cui et al [36].

2ω is then performed to ensure the one-photon absorption induced carrier density by the desired peak pump fluence is in linear range. Hence, the peak energy fluence of 2ω is set at 18 μJ cm^{-2}, induced carrier density of which is estimated to be about 7×10^{18} cm^{-3} at the sample surface. Next we try to match the two-photon absorption induced carrier density with one-photon absorption. The peak pump fluence of ω is 2 mJ cm^{-2}. From the results in Figure 4.4, $\Delta R/R_0$ with both ω and 2ω pump pulses simultaneously present is slightly smaller than the sum of two other signals, which can be attributed to the saturation of the $\Delta R/R_0$ at high carrier densities. To maximize the quantum interference effect between ω and 2ω spots focused on the sample, we also make sure the size of ω spot matches with that of 2ω spot. It can be confirmed by measuring the spatial profiles of $\Delta R/R_0$ with a fixed probe delay of 0.35 ps. Spatial profiles in Figure 4.4 can be fitted well with Gaussian functions, with a width of $W = 2.8$ μm.

To measure the ballistic current, we modulate $\Delta\phi$ between $\pi/2$ and 0. A derivative-like signal as shown in Figure 4.5, is then observed. Then, we further confirm it with a fit. Based on equation 4.3, we calculated a transport distance of about 0.3 nm. We note that although the process of deducing the ΔN and N individually from the measured differential reflection relies on knowledge of the absorption coefficient and pump fluence and is subject to the influence of saturation, only the

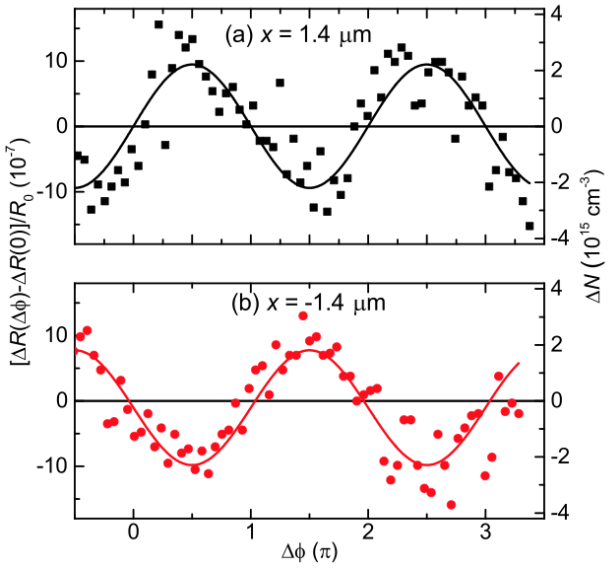

Figure 4.6: Electron accumulation due to transport as a function of $\Delta\phi$ measured at probe positions of 1.4 μm (a) and -1.4 μm (b), respectively. The probe delay is 0.35 ps. Data from Cui et al [36].

ratio $\Delta N/N$ is used in obtaining the transport length. This ratio is not influenced by any of these factors. In the optically injected ballistic currents, the electrons and the holes move oppositely since they have opposite crystal momenta. The signal plotted in Figure 4.5 mainly originates from the electrons since the electron effective mass is a few times smaller than the holes, according to the calculated band structure of ReS_2 [126]. With a smaller effective mass, the electrons are more efficient in inducing a transient absorption signal via phase-space state filling [146]. More importantly, electrons are injected with a higher average velocity and hence move a larger distance than the holes. On the basis of these two factors, we attribute the observed ΔN to the electron density, and the transport length to be the electron transport length.

To demonstrate coherent control of the injected ballistic current, we measure ΔN as a function of $\Delta\phi$ at a probe delay of 0.35 ps and a probe position of $x = 1.4\ \mu m$. This is achieved by measuring the quantity $[\Delta R(\Delta\phi) - \Delta R(\Delta\phi = 0)]/R_0$, as $\Delta\phi$ is varied. The results plotted in Figure 4.6(a) show a clear sinusoidal dependence, as confirmed by a fit (solid line). When the probe spot is moved to $x = -1.4\ \mu m$, the signal changes sign, as shown in Figure 4.6(b). This is consistent with the fact that accumulation of electrons on one side of the profile, due to the transport, is

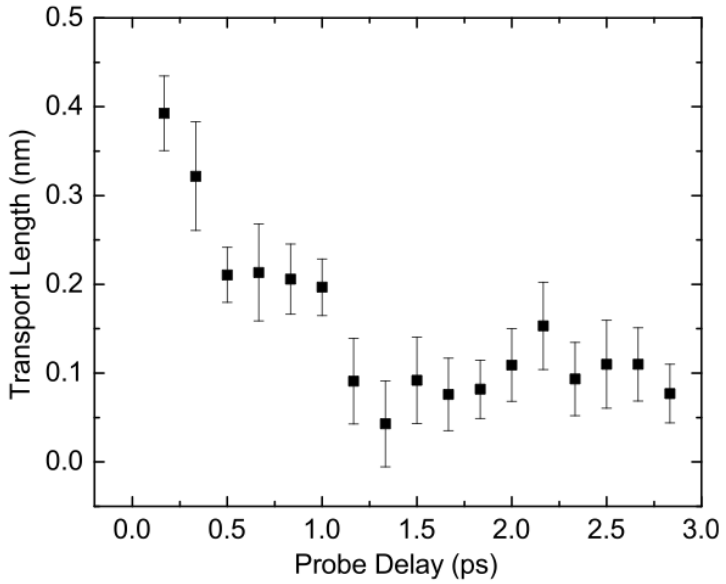

Figure 4.7: Time evolution of the transport length of electrons. Data from Cui et al [36].

always accompanied by a depletion on the other side, as illustrated in Figure 4.5. Since ΔN (and d) is proportional to the initial velocity of electrons and the thus the injected current density, this measurement demonstrates the phase control of the current injection process.

These measurements performed at a fixed probe delay of 0.35 ps demonstrate optical injection and coherent control of ballistic currents in ReS_2. To reveal the dynamics of the injected ballistic currents, we attempt to time resolve the transport process. The measurement is performed by repeating the scan shown in Figure 4.5 at various probe delays. The deduced d as a function of probe delay is shown in Figure 4.7. Despite the rather large error bars due to the laser intensity noise, we can draw a few conclusions. First, the transport distance reaches a peak right after zero probe delay. This indicates that the velocity of the electrons in the injected ballistic currents drops to zero within our time resolution of about 200 fs. Both phonon scattering and electron-hole scattering can contribute to such a fast momentum relaxation process. Considering the high carrier density used in this experiment, we expect the latter to make a bigger contribution. Second, the d decreases to about 20% of its peak value in about 1 ps. This indicates that once the electrons reach their maximal displacement, the Coulomb force from the oppositely moving holes pull them back

toward their original position. Third, the d maintains a value slightly larger than zero for the rest of the time, indicating the electrons do not return to their original position. Since the electrons can rest only when they overlap with the holes, this nonzero final transport length indicates that there is a small center-of-mass motion of the electron-hole system. Since the electron-hole system in the injected ballistic current has no net crystal momentum, such a center-of-mass motion indicates that the carrier system has gained momentum from the lattice during the transport. This can occur because electrons and holes both interact with phonons during their transport and transfer part of their momenta to phonons. Since they have different effective masses and densities of state, their phonon scattering rates are expected to be different. This imbalance of momentum relaxation of electrons and holes due to phonon scattering causes a nonzero net momentum of the electron-hole system and a center-of-mass movement.

Chapter 5

Second harmonic generation microscopy

Second harmonic generation (SHG) is a special effect of second-order nonlinearity. Two photons of the same frequency ω coherently generate one photon of 2ω. In history, observation of SHG with laser in 1961 is widely considered as the birth of nonlinear optics [147]. Due to the giant peak intensity, ultrafast laser is an ideal tool to study SHG in materials. Symmetry properties of a material play an important role for the nonlinear optical phenomenon-SHG. Lack of inversion symmetry of a material is required for SHG. Hence, in 2D monolayers, such as MoS_2, the lack of inversion symmetry usually leads to efficient SHG of an ultrafast laser. In addition, in-plane lattice symmetry of a monolayer is directly related to the tensor structure of SHG. The angular distribution of SHG will provide information of monolayer lattice structure. By measuring the angular dependence of SHG form monolayers, the crystal orientation can be revealed. In the following discussion, we will present the SHG microscopy of MoS_2.

5.1 SHG in 1H monolayer

5.1.1 In-plane SHG of MoS_2

A reflection experimental setup is employed, as shown in Figure 5.1 (a). Fundamental pulse (200 fs) with an angular frequency of ω and a central wavelength of 810 nm is generated from a Ti:

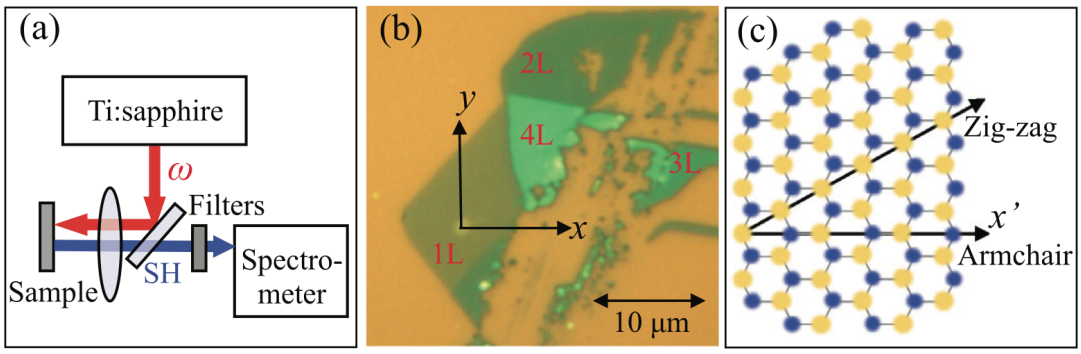

Figure 5.1: 1H lattice MoS_2 in-plane SHG distribution. Data from Kumar et al [148].

sapphire laser. It is tightly focused on the sample by an objective lens with a numerical aperture of 0.42. The FWHM of the spot is about 2 μm. Generated second harmonic (SH) is collected by the same objective lens and sent to a spectrometer. Filters before the spectrometer are used to isolate SH signals. A MoS_2 sample fabricated by mechanical exfoliation is fabricated on a 90 nm SiO_2/Si substrate, indicated in Figure 5.1 (b). The monolayer, labeled as 1L, is characterized by its optical contrast and strong PL. The other fewlayer regions are confirmed by their relative optical contrasts with respect to the monolayer optical contrast.

The lattice structure of monolayer MoS_2 is depicted in Figure 5.1 (c). Mo and S atoms are in blue and yellow, respectively. Monolayer MoS_2 lattice belongs to D_{3h} symmetry. The tensor of second-order susceptibility has nonzero elements of $\chi^{(2)}_{y'y'y'} = -\chi^{(2)}_{y'x'x'} = -\chi^{(2)}_{x'x'y'} = -\chi^{(2)}_{x'y'x'} \equiv \chi^{(2)}$, where $x'y'z'$ are crystalline coordinates. x' is along the armchair direction, which is 30° from the zigzag direction, along which the mirror symmetry is broken. The polarization of fundamental beam is linearly along the horizontal direction (x) of lab coordinate. Normal incidence of fundamental beam is along z'. It is straightforward to show that horizontal (x) and vertical (y) components of SH fields are proportional to $\sin(3\theta)$ and $\cos(3\theta)$, where θ is angle between x and x'. The horizontal and vertical power components of SH are,

$$\begin{aligned} P_x &= P_0 \sin^2(3\theta), \\ P_y &= P_0 \cos^2(3\theta), \end{aligned} \tag{5.1}$$

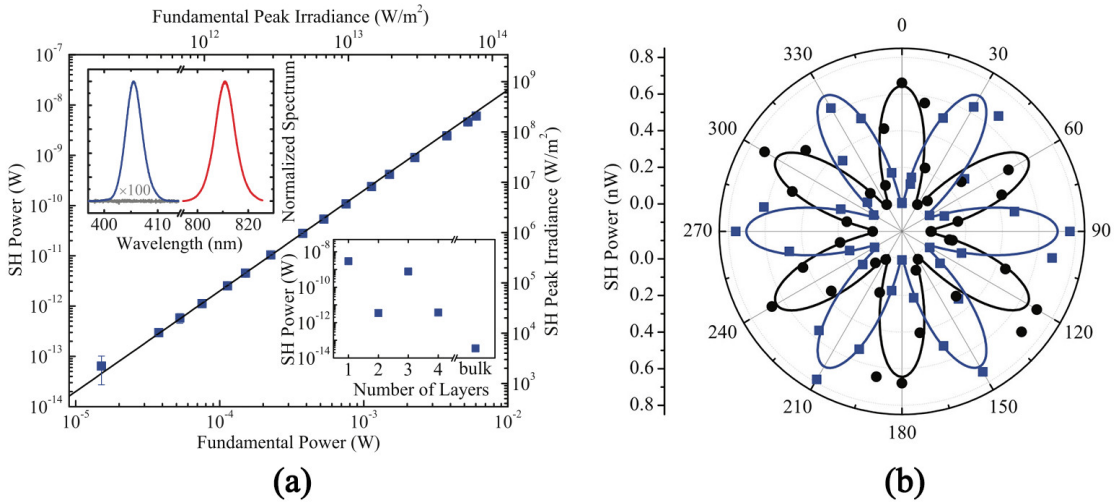

Figure 5.2: Second harmonic generation measured from a mechanically exfoliated MoS_2 sample.(a) The fundamental power dependence of SHG of the monolayer MoS_2. The solid line is a quadratic fitting. The upper inset indicates the spectra of SHG from monolayer MoS_2 (blue), the substrate (multiplied by 100, grey), and the fundamental beams (red). The lower inset is the layer dependence of SHG. (b) Measured power components of SHG in monolayer MoS_2 along the horizontal (blue squares) and vertical direction (black circles) in the lab coordinate as a function of θ. The blue and black solid lines are fitting expected by $\sin^2(3\theta)$ and $\cos^2(3\theta)$, respectively. Data from Kumar et al [148].

where P_0 the total power of SH (P_x+P_y). P_0 is independent of θ.

By fixing the power of fundamental beam at 4 mW, we directly measured the SHG spectra of monolayer MoS_2 centered at 405 nm (blue), as shown in the upper inset of Figure 5.2 (a), where the fundamental beams are at 810 nm (red). To evaluate the contribution of SHG from the substrate, we also measure the spectra of substrate by focusing the fundamental beam on the substrate under the same experimental conditions. From the spectra of bare substrate, the grey line in the upper inset of Figure 5.2 (a), no distinguishable SHG can be observed. This result rules out the contribution of substrate. Next, we carry out the fundamental power dependence of SHG in the monolayer MoS_2. The results (blue squares) match well with a quadratic fitting (solid line), as shown in Figure 5.2 (a), which is the expected behavior of SHG.

To evaluate the SHG from samples of different thicknesses, we carried out thickness dependence of SHG in monolayer, bilayer, trilayer, and quadralayer under the same experimental conditions (the fundamental powers are fixed at 4 mW). The results are shown in the lower inset of

Figure 5.2 (a). SHG power of trilayer is about a factor of seven smaller than the monolayer, while those of the bilayer and quadralayer are about two orders of magnitude smaller than the monolayer. The inversion symmetry should be absent for even atomic layers. Therefore, a nonzero SH response is attributed to the surface and interface effects for SHG results in even atomic layers.

At last, to resolve the in-plane distribution of SHG from monolayer, we focus the fundamental beam on the monolayer MoS_2 sample and a polarizer is placed in front of the spectrometer. P_x and P_y of SHG are measured by rotating the sample around z', that is changing θ, the angle between x and x'. This is facilitated by placing the substrate of the sample on a high precision rotation stage and the rotation center of monolayer sample has been calibrated to overlap with the rotation center of the stage. The corresponding results are in Figure 5.2 (b). We fit the experimental results of SHG by the symmetry analysis model. The angular dependence model as a function of θ agrees with our experimental results. Although the P_x and P_y show strong in-plane angular dependence, the total SHG power remain a constant. Therefore, the SH response of monolayer MoS_2 is in-plane isotropic.

5.1.2 Second-order susceptibility of monolayer MoS_2

Since the SHG of monolayer MoS_2 is in-plane isotropic, we can further extract the magnitude of the second-order susceptibility from the experimental results measured in Figure 5.2 (b). Here, the monolayer MoS_2 is modeled as a bulk medium. In a bulk model, the amplitude of SH field of the horizontal component can be derived as,

$$\varepsilon_x = \frac{1}{4}\frac{i2\omega}{2n_{2\omega}c} d\chi^{(2)}\varepsilon_\omega^2 \sin(3\theta), \tag{5.2}$$

where c is the speed of light, ε_ω is the amplitude of fundamental field and $n_{2\omega}$ the refractive index of MoS_2 at the frequency of SH. Each amplitude of field is related the laser irradiance under the relation: $I = \frac{1}{2}n\varepsilon_0 c\varepsilon\varepsilon^*$. By using the FWHM of fundamental spot W = 2 μm, fundamental pulse repetition frequency f = 81 MHz, fundamental pulse width τ = 200 fs, and $n_{2\omega} \approx 6.0$, the

magnitude of $\chi^{(2)}$ is estimated to be about 10^{-8} m/V. The large value of $\chi^{(2)}$ confirms the large second-order nonlinearity in monolayer MoS_2.

5.2 SHG in a distorted 1T monolayer

Unlike the 1H monolayer, such as monolayer MoS_2, monolayer ReS_2 which has a distorted 1T lattice structure, has inversion symmetry. In fact, inversion is the only preserved symmetry by the lattice distortions. Ideally, SHG should be absent in monolayer ReS_2. However, SHG could still be possible when fabricating monolayer ReS_2 on a substrate and carrying our a measurement. Therefore, it is interesting for us to evaluate the SHG of monolayer ReS_2, which is an anomalous member of 2D semiconducting materials. In this section, we will first present a theoretical calculation of SHG by considering the substrate contributions. Then, we will show the experimental results of SHG in monolayer ReS_2.

5.2.1 Symmetry analysis: SHG of monolayer ReS_2 on a substrate

A model describing SHG of monolayer ReS_2 based on symmetry analysis was developed by our collaborators: Rodrigo A. Muniz and John E. Sipe from University of Toronto [149], which is outlined in the following. The lattice distortions of monolayer ReS_2 will only preserve the inversion symmetry. For a theoretical analysis, here we choose the point group of the 1T lattice assuming there is no lattice distortions. 1T monolayer has a point group D_{3d}, which consists of the inversion operation (i), sixfold improper rotations around the $\hat{z}$ axis (S_6^z), threefold rotations around the $\hat{z}$ axis (C_3^z), twofold rotations around three different horizontal axes ($C_2^{'}$)-or equivalently reflections along those axes (σ_d) since $\sigma_d = iC_2^{'}$, where one of the reflection axes is the $\hat{y}$ axis. In the representation of matrices acting on the basis $(x,y,z)^T$, the symmetry operations correspond to,

$$i = -\begin{bmatrix} 1 & 0 & 0 \\ 0 & 1 & 0 \\ 0 & 0 & 1 \end{bmatrix}, S_6^z = \begin{bmatrix} \frac{1}{2} & -\frac{\sqrt{3}}{2} & 0 \\ \frac{\sqrt{3}}{2} & \frac{1}{2} & 0 \\ 0 & 0 & -1 \end{bmatrix}, C_3^z = \begin{bmatrix} -\frac{1}{2} & -\frac{\sqrt{3}}{2} & 0 \\ \frac{\sqrt{3}}{2} & -\frac{1}{2} & 0 \\ 0 & 0 & 1 \end{bmatrix}, \sigma_d^y = \begin{bmatrix} 1 & 0 & 0 \\ 0 & -1 & 0 \\ 0 & 0 & 1 \end{bmatrix}, \tag{5.3}$$

where the other two reflections were ignored here.

In the presence of a substrate, the transformations that change the $\hat{z}$ axis are broken. For the point group D_{3d}, the broken symmetries are the inversion (i), the sixfold improper rotations around the $\hat{z}$ axis (S_6^z), and the twofold rotations around three different horizontal axes ($C_2^{'}$). The preserved symmetries from the point group C_{3v} that consists of threefold rotations around the $\hat{z}$ axis (C_3^z), and reflections along three horizontal axes (σ_d), which includes σ_d^y. In the representation of matrices acting on the basis $(x, y, z)^T$, the symmetry operations correspond to,

$$C_3^z = \begin{bmatrix} -\frac{1}{2} & -\frac{\sqrt{3}}{2} & 0 \\ \frac{\sqrt{3}}{2} & -\frac{1}{2} & 0 \\ 0 & 0 & 1 \end{bmatrix}, \sigma_d^y = \begin{bmatrix} 1 & 0 & 0 \\ 0 & -1 & 0 \\ 0 & 0 & 1 \end{bmatrix}, \tag{5.4}$$

where the other two reflections were ignored again. Since we are only interested on electric fields in the $\hat{x} - \hat{y}$ plane, here we will focus only on the relations obtained for the tensor components excluding the $\hat{z}$ axis direction.

The second order susceptibility $\chi_{abc}(\omega, \omega)$ is a rank-3 tensor, so it is non-zero only if inversion symmetry is broken. Therefore, a $1T$ lattice will only have a non-zero $\chi_{abc}(\omega, \omega)$ in the presence of a substrate, as even the distortions from the $1T$ lattice of monolayer ReS_2 preserve inversion symmetry. However, in the presence of a substrate the distortions affect the angular dependence of the SHG, although it is expected that these changes are small since the distortions are usually not large. Here we focus on the effect induced by the substrate for an undistorted $1T$ lattice, which has the point group C_{3v}, as discussed above. For second harmonic generation, the last indices of the susceptibility are taken equal, and $\chi_{abc}(\omega, \omega)$ describes the polarization along the

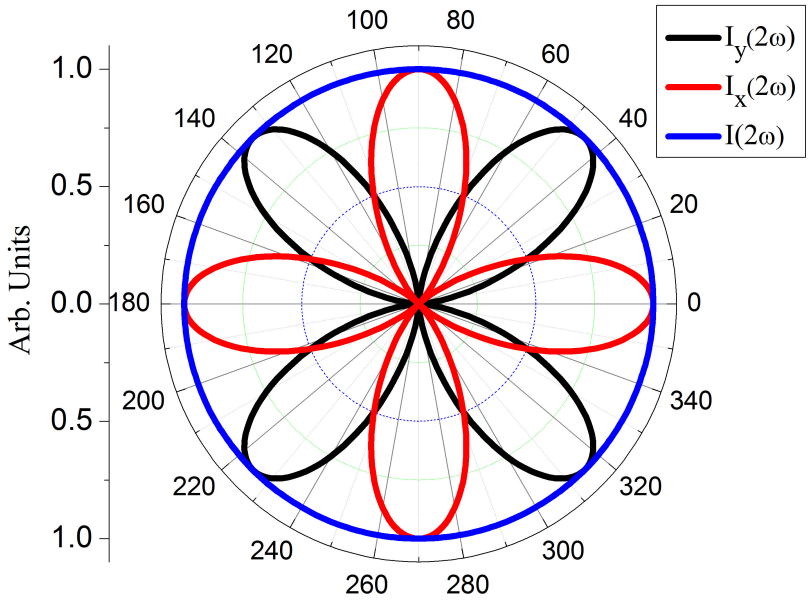

Figure 5.3: In-plane SHG intensities of monolayer ReS_2 along the horizontal (red) and vertical (black) directions and the total intensity (blue), deduced from symmetry analysis.

direction $\hat{a} = \hat{x}\cos\alpha + \hat{y}\sin\alpha$, that is generated by the incident filed polarized along the direction $\hat{b} = \hat{x}\cos\beta + \hat{y}\sin\beta$. For rank-3 tensors, the induced polarization is,

$$\mathbf{P}(2\omega)\cdot\hat{\mathbf{a}} = \chi_{xxx}(\omega,\omega)\cos(\alpha+2\beta)|E(\omega)|^2. \tag{5.5}$$

Hence, the horizontal $\alpha = 0$ and $\alpha = \frac{\pi}{2}$ components are,

$$\begin{aligned} P_x(2\omega) &= \chi_{xxx}(\omega,\omega)\cos(2\beta)|E(\omega)|^2, \\ P_y(2\omega) &= -\chi_{xxx}(\omega,\omega)\sin(2\beta)|E(\omega)|^2, \end{aligned} \tag{5.6}$$

and the intensities of the SHG fields will have angular dependence as,

$$\begin{aligned} I_x(2\omega) &= I_2\cos^2(2\beta) = \tfrac{1}{2}I_2[1+\cos(4\beta)], \\ I_y(2\omega) &= I_2\sin^2(2\beta) = \tfrac{1}{2}I_2[1-\cos(4\beta)], \\ I(2\omega) &= I_x(2\omega)+I_y(2\omega) = I_2. \end{aligned} \tag{5.7}$$

The corresponding results are plotted in Figure 5.3. It is clear that the horizontal and vertical intensity components of SHG fields have a fourfold symmetry while the total intensity is isotropic.

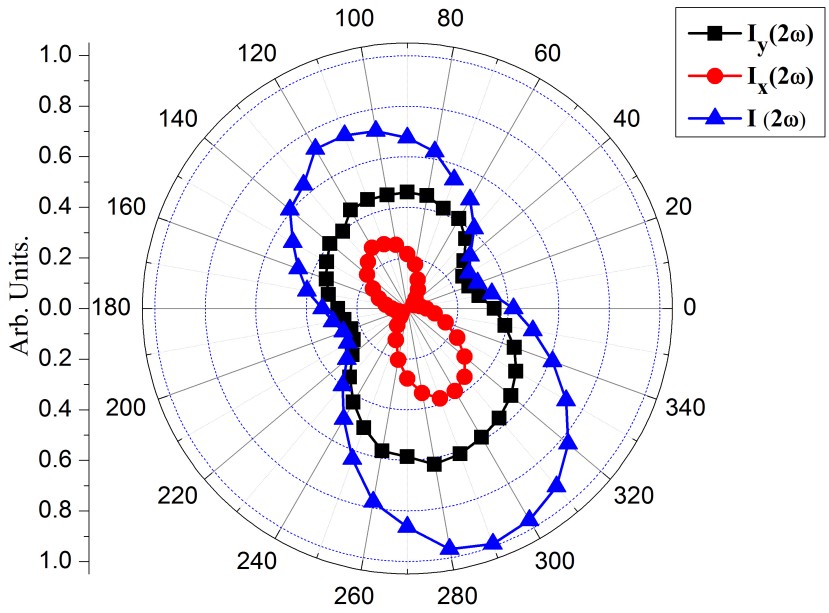

Figure 5.4: In-plane SHG intensities of monolayer ReS_2 along the horizontal (red) and vertical (black) directions and the total intensity (blue), observed in experiments with a fundamental wavelength of 1515 nm.

5.2.2 Experimental results: SHG of monolayer ReS_2 on BK7 substrate

For comparison, we carried out an experiment with femtosecond laser. The monolayer ReS_2 sample is the same one on a BK7 substrate we used for THG study as shown in Figure 6.2. In addition, the experimental conditions are also the same. By rotating the polarization of fundamental pulses with respect to the $\boldsymbol{b}$-axis direction of the lattice, we obtained the in-plane SHG intensities as a function of θ, which is defined as the angle between the x axis of lab coordinate and $\boldsymbol{b}$-axis, as shown in Figure 5.4.

The obtained experimental results show strong deviation from the theoretical prediction as shown in Figure 5.3. In the theoretical calculations, we have assumed there is no lattice distortions for monolayer ReS_2. Therefore, it can be seen that the role of lattice distortions in this specific material should not be neglected. To explicitly extract SHG of the distorted $1T$ lattice, a first principle calculation is highly desired in the future. Our experimental results prove that although

inversion symmetry is preserved in monolayer ReS_2, lattice distortions play an important role for SHG when monolayer ReS_2 is on a substrate. At last, noticing that recently giant anisotropic SHG has been observed in Weyl semimetals [150], which are also 2D materials, we want to point out that SHG is a powerful nonlinear optical spectroscopy for 2D materials.

Chapter 6

Third harmonic generation microscopy

Transition metal dichalcogenides (TMDs) constitute a new generation of semiconducting materials. Understanding light-matter interactions in TMD monolayers is essential for developing applications in electronics, photonics, and optoelectronics. So far, ultrafast excitonic dynamics [151], coupled spin-valley physics [152, 153], large exciton binding energies [154, 155], and nonlinear optical responses [148, 156–158] in TMD monolayers have been widely explored. It has been also shown that van der Waals heterostructures with different TMD monolayers can be constructed [159] to realize devices with multiple functionalities.

Unlike the TMD monolayers based on Mo and W, which form in a hexagonal lattice, monolayer ReS_2 has a stable distorted $1T$ crystal lattice [160]. Re atomic chains formed by Re-Re bonding run along the direction of the $\boldsymbol{b}$-axis, enabling the in-plane anisotropy of electrical and optical response. As a result, ReS_2 has been identified as an anomalous member of the TMD family. In 2014, few-layer and bulk samples of ReS_2 were reported to display monolayer behavior [161]. Since then the optical and electrical properties of ReS_2 have been intensively investigated. Coherent control of nanoscale ballistic transport has been realized in ReS_2 thin films [162]. The in-plane anisotropic optical and electrical properties of monolayer ReS_2 have also been experimentally studied [163, 164]. A recent work has shown that stacking orders can be resolved by Raman spectroscopy, due to the unique crystal structure of ReS_2 [165]. Based on these novel properties,

a wide spectrum of applications using ReS_2 has been proposed. Among them are energy storage devices [166, 167], integrated digital converters [168], and sensitive photodetectors [169–172]. However, to date there have been no reports of the nonlinear optical properties of ReS_2. Since nonlinear optical properties are known to be extremely sensitive to lattice symmetry [173, 174], it is important to determine to what extent the lattice distortions of ReS_2 affect its nonlinear optical properties.

In this chapter, we present experimental results of third harmonic generation (THG) in monolayer and multilayer ReS_2. We determine the third-order susceptibility of monolayer ReS_2 and find that its magnitude is about one order of magnitude larger than those of hexagonal TMDs such as MoS_2 [156]. We also find that the third-order nonlinear response has strong in-plane anisotropies incompatible with an undistorted 1T lattice.

6.1 1T distorted lattice structure of ReS_2

We use 250 fs pulses generated from an optical parametric oscillator pumped by a Ti:sapphire near-infrared laser. As shown in Figure 6.1(a), a half wave plate (HW) and a Glan prism (GP) are used to adjust the power and the polarization direction of the fundamental pulses. The fundamental pulses at ω are tightly focused on the sample by an objective lens (OB1) with a numerical aperture (NA) of 0.42. The generated third harmonic pulses are collected by another objective lens (OB2) with the same NA. A spectrometer (SM) is employed to directly measure the power of the third harmonic pulses at 3ω, and a polarizer (P) before the spectrometer is used to resolve the horizontal and vertical components of the third harmonic pulses. A charge-coupled device (CCD), a beam-splitter (BS), and the OB1 serve as a microscope to monitor the focusing position on the sample by collecting the reflected light at 3ω.

Figure 6.1(b) shows a diagram of THG in monolayer ReS_2 with a simplified band structure, where three photons at ω generate one photon at 3ω. The fundamental photon energy is about $\hbar\omega = 0.82$ eV (1515 nm), while the energy of the generated photons is about $3\hbar\omega = 2.46$ eV (505 nm). Since the band gap of monolayer ReS_2 is about 1.53 eV (810 nm), the fundamental pulse can

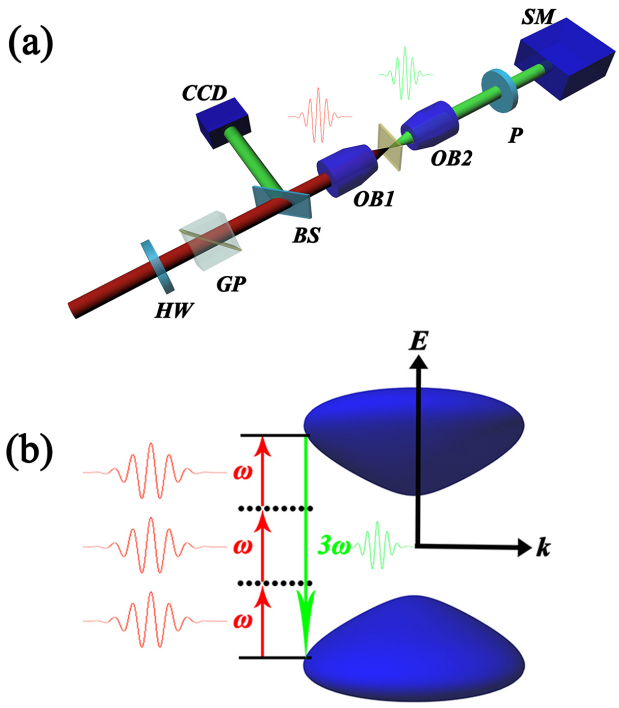

Figure 6.1: (a) Experimental setup: the infrared femtosecond laser (red pulse) is tightly focused on the sample by an objective lens (OB1). The induced THG signal (green pulse) is directly measured by a spectrometer(SM). HW is a half wave plate, GP represents a Glan prism, and P is a polarizer. (b) The diagram illustrates the THG due to the fundamental pulse ω and the monolayer ReS_2 bandstructure.

not be absorbed by monolayer ReS_2 via one-photon absorption. The ReS_2 samples are fabricated on the surface of PDMS by mechanical exfoliation and transferred to a BK7 glass substrate about 0.48 mm thick [175]. All measurements are carried out in ambient conditions.

An optical microscope image of the monolayer ReS_2 sample is shown in Figure 6.2(a), where the monolayer flake is attached to a multilayer. The red dots 1 and 2 in the same figure indicate the focused fundamental laser spots on the monolayer and multilayer, respectively. The figure also shows laboratory axes x and y, as well as the angle θ between the fundamental pulse polarization and the x-axis. The lattice structure of ReS_2 monolayer is depicted in Figure 6.2(b); Re atom chains are formed along the $\boldsymbol{b}$-axis direction, which is depicted by the blue arrow and experimentally determined by transient absorption measurement (see Supplemental Material). As shown in Figure 6.2(a), the $\boldsymbol{b}$-axis direction is along one of the two cracked edges of the flake.

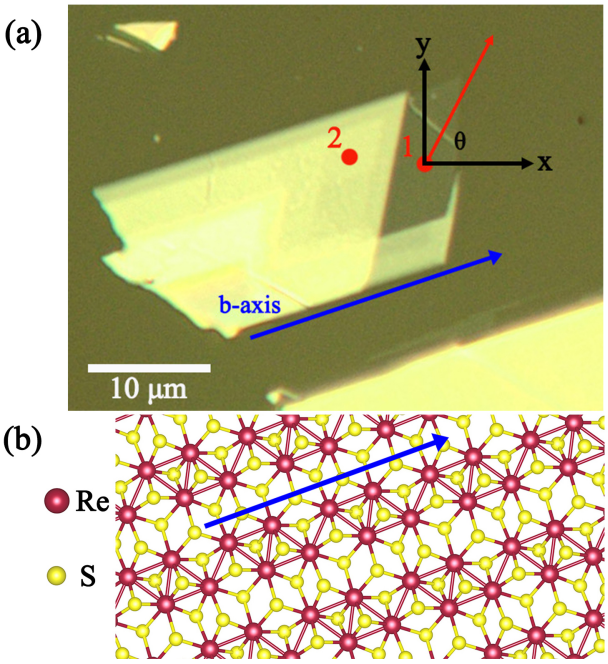

Figure 6.2: (a) Microscope image of monolayer ReS_2 and attached multilayer ReS_2. The red dots 1 and 2 are the laser focusing positions for monolayer and multilayer measurements respectively. The blue arrow indicates the ***b***-axis direction, which is the direction of the Re atom chains in the lattice. The x and y axes define the lab coordinates, and θ denotes the angle between the polarization direction of the fundamental pulse (red arrow) and the x-axis. (b) The distorted 1T lattice structure of ReS_2, showing the Re atom chain along the ***b***-axis (blue arrow).

An optical contrast technique [176] is employed to determine the thickness of the samples. In Figure 6.3(a), the black line indicates a cross section of our monolayer and multilayer samples. As shown in Figure 6.3(b), the normalized optical contrast of the monolayer (1 L, 0.73 nm thick) and multilayer samples in the green channel are about 7.6 % and 100 %, respectively. Since each layer increases the optical contrast by roughly 7.6 %, the multilayer sample is identified as 13 L, which is about 9.5 nm thick. Similarly, the transition region with an optical contrast of 92.4 % is about 1 μm wide and identified as 12 L.

In order to determine the crystal orientation of our monolayer ReS_2 sample, we measured the angular dependence of differential transmission by pump-probe femtosecond laser pulses. A simplified experimental setup is shown in Figure 6.4. The femtosecond laser pulses with a wavelength of 810 nm are generated by a Ti: Sapphire oscillator, which is pumped by a CW laser with a wavelength of 532 nm. Part of the 810 nm power is picked up by a beam splitter to serve as the

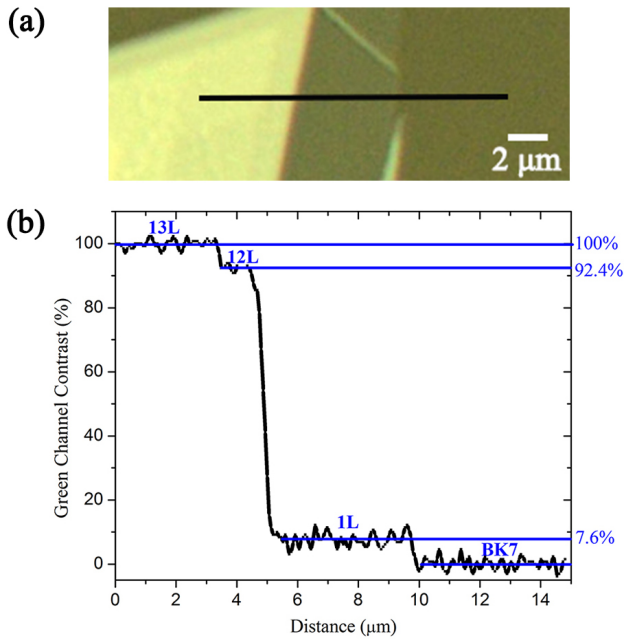

Figure 6.3: (a) Zoom in of the sample region used for optical contrast calculations. (b) Normalized optical contrast of green channel along the black line indicated in (a).

probe for our sample. The rest of the 810 nm power is sent to an optical parametric oscillator (OPO). The signal of the OPO with a frequency corresponding to 1464 nm is focused on a BBO crystal to generate a 732 nm beam, which is used as the pump. The duration of the 732 nm and 810 nm pulses are respectively about 250 fs and 150 fs. Before the beams reach the OB1, a Glan prism is used to ensure the same polarization of the pump and probe pulses when focusing on the sample. The OB2 collects and collimates the transmitted 810 nm probe pulses, which is sent to a silicon detector. Lock-in detection is employed to measure the differential transmission of the probe induced by the pump. The chopping frequency is 2.2 kHz.

The lab coordinate system in this measurement is the same as in the THG measurement. The polarization directions of the pump and probe lasers are the same, even as the Glan prism is rotated. For each polarization angle of the Glan prism, equal pump and probe fluences are maintained by tuning the two half-wave plates (HW). Under this configuration, we measure $\Delta T/T_0$ as a function of the polarization angle of the pump and probe lasers with respect to the sample lattice orientation.

Figure 6.5(a) shows the temporal dynamics of the monolayer sample when the polarization

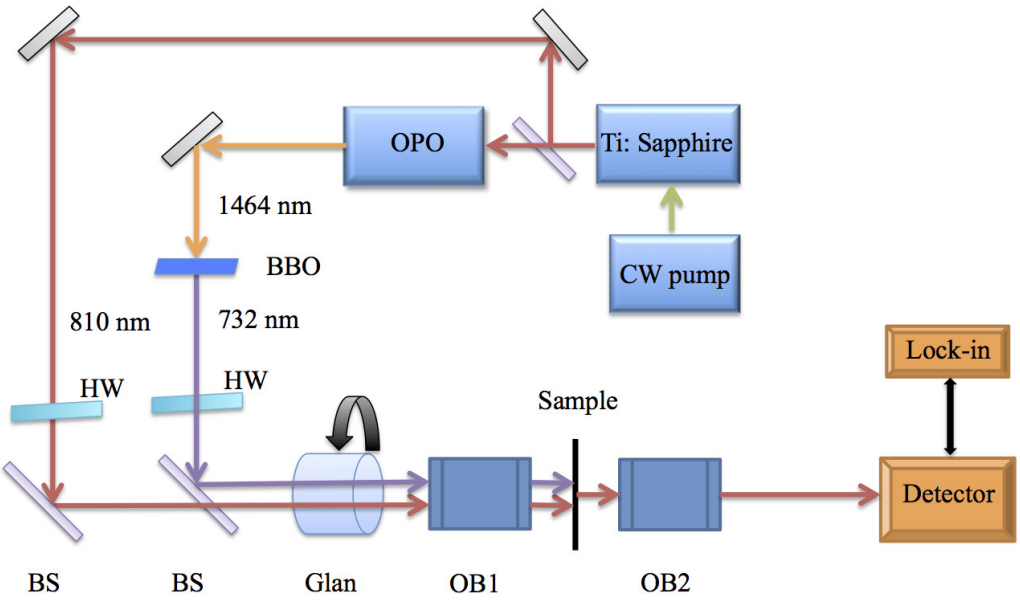

Figure 6.4: Simplified experimental setup for the transient absorption measurement.

angle is 20° with respect to the horizontal direction in the lab coordinate system. This is the angle for which maximum $\Delta T/T_0$ is observed. Figure 6.5(b) shows a polar plot of the angular dependence of $\Delta T/T_0$ for a fixed probe delay time of about 3 ps. It was known through previous studies that the transient absorption signal is strongest when polarizations of pump and probe are both along $\boldsymbol{b}$-axis direction. Therefore, after fitting it with a cosine square function (blue solid line in (b)), the $\boldsymbol{b}$-axis of our monolayer sample corresponds to 20°, which is indicated by blue arrows in Figure 2 of the main text.

6.2 Symmetry analysis of THG in an undistorted 1T lattice

In this section we carry out a point group symmetry analysis for the THG of undistorted 1T layered materials; we use the lab coordinates shown in Figure 6.2(a). A model describing THG of monolayer ReS_2 based on symmetry analysis was developed by our collaborators: Rodrigo A. Muniz and John E. Sipe from University of Toronto [149], which is outlined in the following.

The polarization associated with THG is determined by the third order susceptibility $\chi^{(3)}_{abcd}(\omega,\omega,\omega)$, which is a rank-4 tensor that respects the symmetries of the point group of the lattice, and the ap-

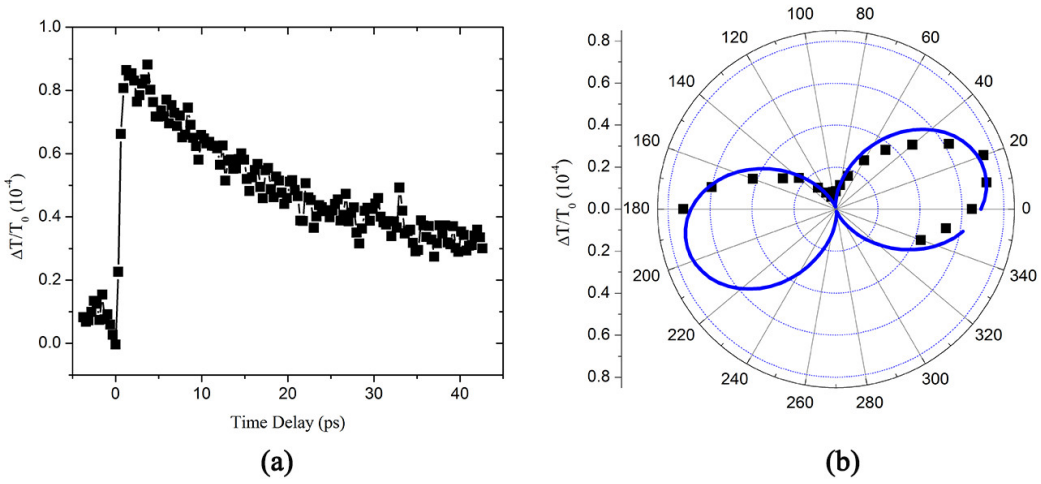

Figure 6.5: (a) Temporal dynamics of monolayer ReS_2. (b) Angular dependence of the differential transmission in monolayer ReS_2 at 3 ps.

plied electric field $\mathbf{E}(t) = \mathbf{E}(\omega) e^{-i\omega t} + c.c.$, through

$$P_a(3\omega) = \varepsilon_0 \chi^{(3)}_{abcd}(\omega,\omega,\omega) E_b(\omega) E_c(\omega) E_d(\omega). \tag{6.1}$$

The electric field associated with the generated radiation is proportional to the polarization $\mathbf{P}(3\omega)$, so the intensity of the generated radiation is proportional to $|P(3\omega)|^2$.

The point group of an undistorted $1T$ lattice is D_{3d} ($\bar{3}\frac{2}{m}$), but in the presence of a substrate the symmetry operations that act on the perpendicular axis are broken, and the point group is C_{3v} ($3m$). Only the planar components of $\chi^{(3)}_{abcd}$ are relevant for normal incidence, and there are only 3 such independent components for both point groups D_{3d} and C_{3v}, namely $\chi^{(3)}_{xxxx}$, $\chi^{(3)}_{xxyy}$ and $\chi^{(3)}_{xyyx}$. Consequently, the THG has the same angular dependence regardless of the presence of the substrate. Describing the incident field as $\mathbf{E}(\omega) = E(\omega)(\hat{\mathbf{x}}\cos\theta + \hat{\mathbf{y}}\sin\theta)$, the polarization associated with the THG field is given by

$$\begin{aligned} P_x(3\omega) &= \varepsilon_0 \chi^{(3)}_{xxxx} [E(\omega)]^3 \cos(\theta), \\ P_y(3\omega) &= \varepsilon_0 \chi^{(3)}_{xxxx} [E(\omega)]^3 \sin(\theta), \end{aligned} \tag{6.2}$$

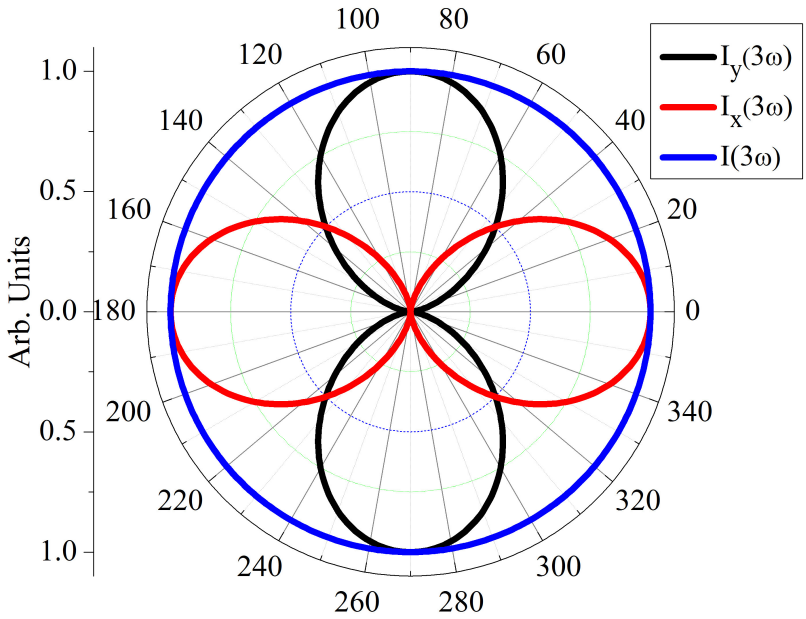

Figure 6.6: The intensities of the different polarizations of the THG field are shown as a function of the angle of polarization of the incident field. The red line corresponds to the horizontal (x-axis) polarization, the black line corresponds to vertical (y-axis) polarization, and the blue line corresponds to the total intensity of the THG field.

and the intensities of the THG fields horizontally and vertically polarized are

$$\begin{aligned} I_x(3\omega) &= \tfrac{1}{2} I_{max}\left[1+\cos(2\theta)\right], \\ I_y(3\omega) &= \tfrac{1}{2} I_{max}\left[1-\cos(2\theta)\right]. \end{aligned} \tag{6.3}$$

Thus the total intensity $I_x + I_y$ is independent of the polarization direction of the incident fields. The above expressions are plotted in Figure 6.6, which shows the isotropy of the total intensity of the THG from an undistorted $1T$ lattice. Thus any anisotropy in the experimental results of the total THG for ReS_2 is due to its lattice distortions.

6.3 Optical fields in the atomic layer of monolayer ReS_2

We model the system by a sample (s) slab of thickness d on top of a glass (g) substrate of thickness $L = 0.48$ mm. Since L is much larger than the photon wavelengths, and the light that reaches the bottom glass-air interface is diverging, we can neglect multiple reflections and assume the

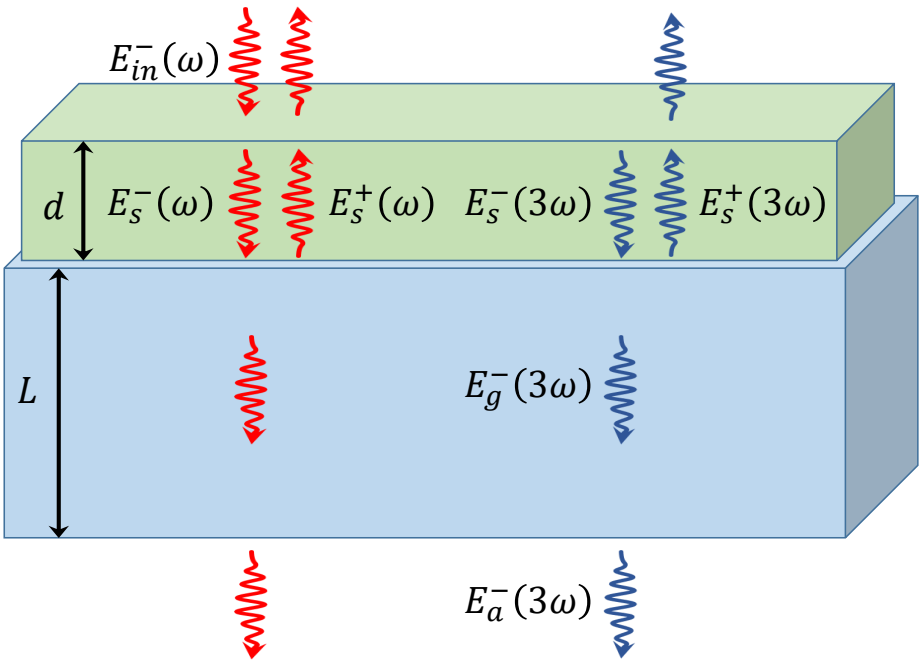

Figure 6.7: Diagram of the fundamental and third harmonic fields in the different regions of the structure. Only the fields used in the calculations are labeled.

transmission is direct at the lowest interface. Fig. 6.7 shows a diagram of the structure. The fundamental field is incident from air (a) above the sample, and our goal in this subsection is to find the fundamental field at sample. For normal incidence, the transmission and reflection coefficients for a single interface are

$$t_{12} = \frac{2n_1}{n_1+n_2}, \qquad r_{12} = \frac{n_1-n_2}{n_1+n_2}. \tag{6.4}$$

The Fresnel coefficients give

$$\begin{aligned} E_g^{-}(\omega) &= \frac{e^{in_s\tilde{\omega}d}t_{as}t_{sg}}{1-e^{2in_s\tilde{\omega}d}r_{sa}r_{sg}}E_{in}^{-}(\omega), \\ E_s^{+}(\omega;z) &= \frac{e^{in_s\tilde{\omega}(d+z)}t_{as}r_{sg}}{1-e^{2in_s\tilde{\omega}d}r_{sa}r_{sg}}E_{in}^{-}(\omega), \\ E_s^{-}(\omega;z) &= \frac{e^{in_s\tilde{\omega}(d-z)}t_{as}}{1-e^{2in_s\tilde{\omega}d}r_{sa}r_{sg}}E_{in}^{-}(\omega), \end{aligned} \tag{6.5}$$

where $\tilde{\omega} = \omega/c$. The total field at the sample is

$$E_s(\omega;z) = E_s^+ + E_s^- = \frac{e^{in_s\tilde{\omega}d}t_{as}\left(e^{-in_s\tilde{\omega}z} + e^{in_s\tilde{\omega}z}r_{sg}\right)}{1 - e^{2in_s\tilde{\omega}d}r_{sa}r_{sg}}E_{in}^-(\omega). \tag{6.6}$$

Since $d \ll \lambda$ such that $\tilde{\omega}d \ll 1$, the field is approximately uniform inside the slab, and we approximate the field everywhere in the slab by its value at the center of the slab $E_s(\omega;z) \simeq E_s(\omega;z = d/2) = E_s(\omega)$, which gives

$$E_s(\omega) \simeq \frac{t_{as}(1+r_{sg})}{1 - r_{sa}r_{sg}}E_{in}^-(\omega) = \frac{2n_a}{n_a + n_g}E_{in}^-(\omega). \tag{6.7}$$

Now that the fundamental field at the sample is determined, we can determine the THG field.

6.3.1 Third harmonic field

The THG field can be obtained from the polarization in the sample region, as referenced in the main text. We assume $\tilde{\omega}d \ll 1$ again, such that the third harmonic fields are also approximately uniform in the slab, which gives

$$\begin{aligned} E_s^-(3\omega) &= \left[\tfrac{1}{1-r_{sg}r_{sa}} + \tfrac{r_{sa}}{1-r_{sg}r_{sa}}\right] i\tfrac{3\tilde{\omega}d}{2\varepsilon_0 n_s}P(3\omega), \\ E_s^+(3\omega) &= \left[\tfrac{r_{sg}}{1-r_{sg}r_{sa}} + \tfrac{1}{1-r_{sg}r_{sa}}\right] i\tfrac{3\tilde{\omega}d}{2\varepsilon_0 n_s}P(3\omega). \end{aligned} \tag{6.8}$$

The field that is transmitted to the glass is

$$E_g^-(3\omega) = t_{sg}E_s^-(3\omega) = \frac{2n_s}{n_a + n_g} i\left(\frac{3\tilde{\omega}d}{2\varepsilon_0 n_s}\right)P(3\omega), \tag{6.9}$$

which, in terms of the incident field, is

$$E_g^-(3\omega) = i\frac{3\tilde{\omega}d}{n_a + n_g}\chi^{(3)}\left[E_s(\omega)\right]^3, \tag{6.10}$$

where $P(3\omega) = \varepsilon_0\chi^{(3)}\left[E_s(\omega)\right]^3$ was used.

The THG field then passes through the glass substrate in the region $0 > z > -L$, being transmitted directly (the roughness of the bottom surface renders the reflections dispersive) at the bottom interface such that

$$E_a^-(3\omega) = t_{ga} E_g^-(3\omega) = ie^{in_g\tilde{\omega}L} \frac{2n_g}{(n_a+n_g)^2} (3\tilde{\omega}d)\chi^{(3)} E_s(\omega)^3 . \tag{6.11}$$

The next step is to determine the power collected by the detector.

6.3.2 Power of the THG field

The irradiance of the third harmonic field propagating downwards in the air is

$$\begin{aligned} I_a^-(3\omega) = & \ 2c\varepsilon_0 n_a \left|E_a^-(3\omega)\right|^2 \\ = & \ \frac{8c\varepsilon_0 n_a n_g^2}{\left(n_a+n_g\right)^4} (3\tilde{\omega}d)^2 \left|\chi^{(3)}\right|^2 |E_s(\omega)|^6 , \end{aligned} \tag{6.12}$$

in terms of the incident field it is

$$\begin{aligned} I_a^-(3\omega) = & \ \frac{2^9 n_a^7 n_g^2}{\left(n_a+n_g\right)^{10}} c\varepsilon_0 (3\tilde{\omega}d)^2 \left|\chi^{(3)}\right|^2 \left|E_{in}^-(\omega)\right|^6 \\ = & \ \frac{2^6 n_a^4 n_g^2}{\left(n_a+n_g\right)^{10}} \frac{(3\tilde{\omega}d)^2}{(c\varepsilon_0)^2} \left|\chi^{(3)}\right|^2 I_{in}(\omega)^3 . \end{aligned} \tag{6.13}$$

For an incident beam that is Gaussian in both space and time, the irradiance is

$$I_{in}(\omega;r,t) = I_{in}^0(\omega) e^{-\ln 2\left(\frac{2r}{W}\right)^2} e^{-\ln 2\left(\frac{2t}{\tau}\right)^2}, \tag{6.14}$$

where W and τ are respectively the spot size width and the pulse duration measured at full width at half maximum. The maximal irradiance $I_{in}^0(\omega)$ is related to the average laser power by

$$\bar{P}_{in}(\omega) = f_{rep} \left(\frac{\pi}{\ln 2}\right)^{\frac{3}{2}} \frac{\tau}{2} \left(\frac{W}{2}\right)^2 I_{in}^0(\omega) , \tag{6.15}$$

where f_{rep} is the laser repetition rate. Following Eq. (6.13), the third harmonic irradiance is

$$I_a^- (3\omega; r, t) = I_a^0 (3\omega)\, e^{-3\ln 2\left(\frac{2r}{W}\right)^2} e^{-3\ln 2\left(\frac{2t}{\tau}\right)^2}, \tag{6.16}$$

where

$$I_a^0 (3\omega) = \frac{2^6 n_a^4 n_g^2}{(n_a + n_g)^{10}} \frac{(3\tilde{\omega} d)^2}{(c\varepsilon_0)^2} \left|\chi^{(3)}\right|^2 I_{in}^0 (\omega)^3, \tag{6.17}$$

and its average power is

$$\bar{P}_a (3\omega) = f_{rep} \left(\frac{\pi}{\ln 2}\right)^{\frac{3}{2}} \frac{\tau}{2\sqrt{3}} \left(\frac{W}{2\sqrt{3}}\right)^2 I_a^0 (3\omega). \tag{6.18}$$

The susceptibility $\left|\chi^{(3)}\right|$ can then be determined by

$$\left|\chi^{(3)}\right| = \frac{(n_a + n_g)^5}{8 n_a^2 n_g} \frac{c\varepsilon_0}{3\tilde{\omega} d} \sqrt{\frac{I_a^0 (3\omega)}{I_{in}^0 (\omega)^3}}, \tag{6.19}$$

and since

$$\sqrt{\frac{I_a^0 (3\omega)}{I_{in}^0 (\omega)^3}} = f_{rep} \left(\frac{\pi}{\ln 2}\right)^{\frac{3}{2}} \frac{\tau}{2} \left(\frac{W}{2}\right)^2 \sqrt{\frac{3\sqrt{3}\bar{P}_a (3\omega)}{\bar{P}_{in} (\omega)^3}}, \tag{6.20}$$

we finally have

$$\left|\chi^{(3)}\right| = \frac{(n_a + n_g)^5}{8 n_a^2 n_g} \frac{c\varepsilon_0}{3\tilde{\omega} d} f_{rep} \left(\frac{\pi}{\ln 2}\right)^{\frac{3}{2}} \frac{\tau}{2} \left(\frac{W}{2}\right)^2 \sqrt{\frac{3\sqrt{3}\bar{P}_a (3\omega)}{\bar{P}_{in} (\omega)^3}}, \tag{6.21}$$

where in the experiment $n_a = 1$ and $n_g = 1.521$, $W = 3.5\,\mu$m, $\tau = 250$ fs and $f_{rep} = 80.54$ MHz.

We note the final result is independent of the index of the sample $n_s = 4.17$. We also note that even though the calculation of the power that is absorbed by the detector assumes that the beam width is maintained throughout the entire apparatus, it still gives the correct result for the power transmitted as the factor due to the different areas compensates the factors for the fields or irradiance.

6.4 Results and analysis: strong and anisotropic THG

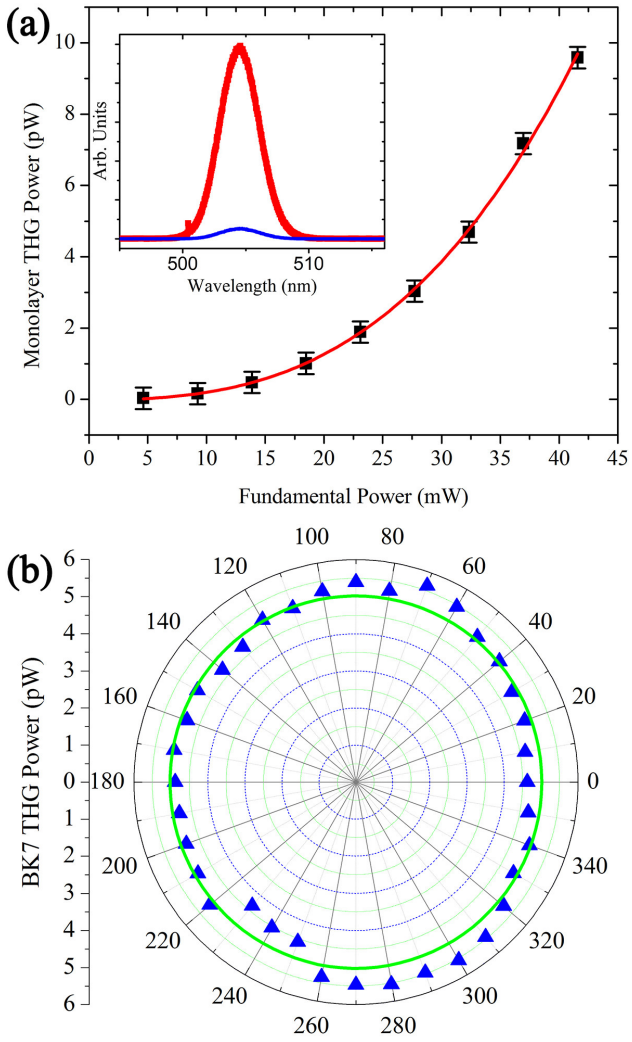

Figure 6.8: (a) THG power (black rectangles) of monolayer ReS_2 as a function of fundamental power. The red line is a cubic fitting. The inset illustrates the third harmonic spectrum from the monolayer ReS_2 sample (red) and the BK7 glass substrate (blue) under the same experimental conditions. (b) Angular dependence of THG (blue triangles) in BK7 glass substrate when the fundamental pulse power is fixed at 23 mW. The green line is an isotropic fitting.

We study THG of monolayer ReS_2 by focusing the fundamental field on the red dot 1 as shown in Figure 6.2(a). The THG spectrum is shown as the red curve in the inset of Figure 6.8(a), which corresponds to $\theta = 310^\circ$ and a fundamental fluence of 12.6 mJ/cm^2. In our experiments, third harmonic frequencies can also be generated from the BK7 glass substrate. The blue curve in the inset of Figure 6.8(a), which is about 5 % of the red curve, shows the third harmonic spectrum of

the BK7 glass substrate under the same experimental conditions as the monolayer ReS_2 sample. In addition, we notice that THG from BK7 glass substrate becomes maximal when moving the ω beam focus away from the surface and into the BK7 glass substrate. Thus we study THG from the BK7 glass substrate by moving the focus of the fundamental beam into the substrate by a few μm. There is no angular dependence of THG power from the BK7 glass substrate when the power of the fundamental beam is fixed at 23 mW, as shown in Figure 6.8(b). What's more, since the contribution from the BK7 glass substrate is much smaller than the THG from ReS_2 samples, it has no effect in our analysis. The fundamental power dependence of THG in monolayer ReS_2 is shown in Figure 6.8(a) for $\theta = 310°$. The cubic power fit (red line) matches well with the data (black rectangles), as expected for a THG process.

By tuning the HW and the GP we measure THG in monolayer ReS_2 as a function of θ, under the same fundamental fluence of 16.5 mJ/cm^2. Horizontal and vertical polarizations of the THG field are resolved by the polarizer before the spectrometer. The results are plotted in Figure 6.9(a), where the lines corresponding to the horizontal and vertical polarizations have the shape of a twisted dumbbell, and the total power (i.e. the sum of the horizontal and vertical components) of the THG field from monolayer ReS_2 is anisotropic as a function of θ.

In order to quantify the THG in monolayer ReS_2, we deduce the magnitude of the third-order susceptibility $\left|\chi^{(3)}\right|$ from the power of the THG field that reaches the detector $\bar{P}_a(3\omega)$ and that of the fundamental incident field $\bar{P}_{in}(\omega)$. Here we extract an estimate for the magnitude of the largest component of $\chi^{(3)}$, which we denote by $\left|\chi^{(3)}\right|$. The fundamental field at the sample is related to the incident field by Fresnel equations. The induced polarization is related to the fundamental field at the sample by Eq. (6.2). The THG field at the sample can then be determined from the polarization [174], which in turn determines the field that is transmitted through the glass substrate and collected by the detector. Considering pulses that are Gaussian in both space and time, the final expression is

$$|\chi^{(3)}| = \left(\frac{\pi}{\ln 2}\right)^{\frac{3}{2}} \frac{(n_a+n_g)^5}{8n_a^2 n_g} \frac{c^2\varepsilon_0}{3\omega d} f_{rep} \frac{\tau}{2} \left(\frac{W}{2}\right)^2 \sqrt{\frac{3\sqrt{3}\bar{P}_a(3\omega)}{\bar{P}_{in}(\omega)^3}}, \tag{6.22}$$

where d is the thickness of the sample, $n_a \approx 1$ and $n_g = 1.521$ are respectively the indices of refraction of air and the BK7 glass substrate (which are both independent of the frequencies involved, ω and 3ω); W and τ are respectively the spot size width and the pulse duration measured at full width at half maximum, and $f_{rep} = 80.54$ MHz is the laser repetition rate. See the Supplemental Material for details on the derivation of this equation. By using the parameters measured in our experiment ($d = 0.73$ nm, $\tau = 250$ fs, $W = 3.5$ μm, and $\lambda = 1515$ nm), we extract the maximal value of $\left|\chi^{(3)}_{20^\circ}\right| \sim 5.3 \times 10^{-18}$ m^2/V^2 for $\theta = 20^\circ$. The maximal THG is confirmed to occur when the polarization of the fundamental field is along the $\boldsymbol{b}$-axis, as determined by angular dependent transient absorption. Thus, THG measurements can be also used to determine the lattice orientation of ReS_2. When $\theta = 70^\circ$, the THG field power reduces to about one third of the maximal value, so $\left|\chi^{(3)}_{70^\circ}\right| \sim 3.5 \times 10^{-18}$ m^2/V^2 is the minimal value of the susceptibility.

To confirm the procedure used to extract the $\left|\chi^{(3)}\right|$ of the monolayer ReS_2 sample, we move the fundamental pulse focus spot to the BK7 glass substrate, which allows us to measure the THG from the BK7 glass substrate under the same conditions. The angular dependence of THG in the BK7 glass substrate is isotropic, as shown in Figure 6.8(b). We extract a $\left|\chi^{(3)}_{BK7}\right| \sim 2.27 \times 10^{-22}$ m^2/V^2 for the BK7 substrate, which is in good agreement with the reported values of $\left|\chi^{(3)}_{BK7}\right| = 2.98 \times 10^{-22}$ m^2/V^2 for a fundamental wavelength of 1064 nm and $\left|\chi^{(3)}_{BK7}\right| = 2.38 \times 10^{-22}$ m^2/V^2 for 1907 nm [177]. The power of the THG due to the substrate is more than 20 times smaller than that of the ReS_2, as shown in the inset of Fig. 6.8 (a). Thus, even the heterodyne contribution of the substrate to the total power of the THG is at least 10 times smaller than that due exclusively to the ReS_2 sample, which lies within the experimental precision. So the contribution of THG from the BK7 glass substrate is ignored in our analysis.

We also use the method described above to study the THG from multilayer ReS_2 by focusing the fundamental laser on the attached multilayer part of the sample, as indicated by the red dot 2 in Fig. 6.2(a). The observed THG from the attached multilayer (13 L) shows an angular dependence very similar to that of monolayer ReS_2. This is a reasonable result, since the attached multilayer should have the same crystal orientation of the monolayer, resulting in the same in-plane symme-

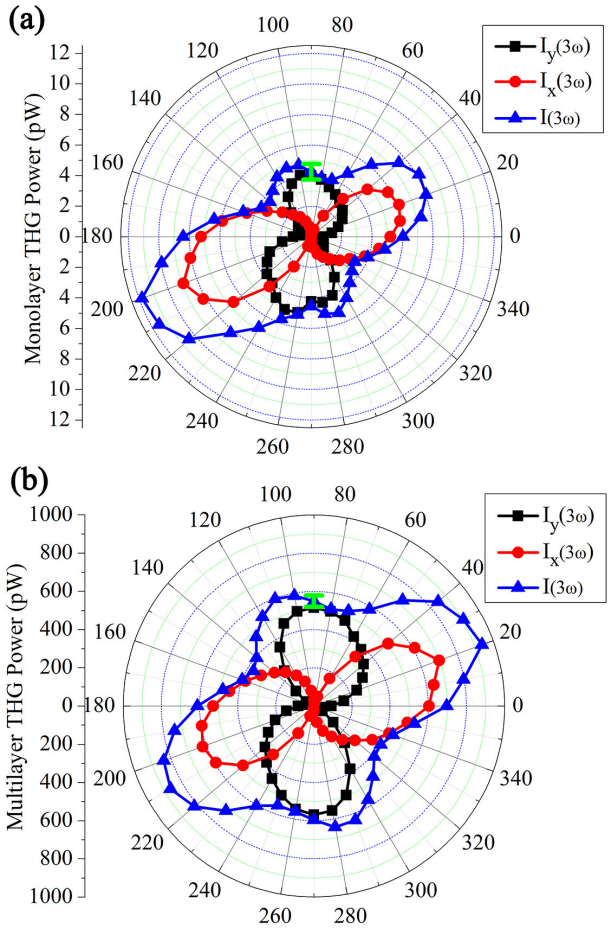

Figure 6.9: Angular dependence of THG power in monolayer ReS_2 (a) and attached multilayer ReS_2 (b). Horizontal, vertical components of total THG power (blue) are in red and black, respectively. The fundamental pulse power is fixed at 30.2 mW.

try of THG. In addition, the THG signal in the multilayer sample is significantly larger than that from the monolayer. Due to the weak interlayer coupling in ReS_2, the THG field from a multilayer sample can be considered as the addition of THG fields generated in each individual layer, and the THG induced power would be simply expected to be proportional to the square of the sample thickness d – see Eq. 6.22. Thus, the THG power from the 13 L sample would be expected to increase by a factor of 169, relative to the monolayer, for each θ. However, since the photon energy of THG is higher than the band gap of ReS_2, the induced THG will be absorbed via one-photon absorption when propagating in the multilayer sample. It has been well-known that linear absorption in ReS_2 is in-plane anisotropic. A maximum (minimum) absorption coefficient is expected

when light polarization is along (perpendicular to) the $\boldsymbol{b}$-axis, which is clearly revealed by our experimental results: Fig. 6.9 shows that when compared to the monolayer THG, the multilayer THG is mostly suppressed by absorption when the polarization of the induced THG is along the $\boldsymbol{b}$-axis ($\theta = 20^{\circ}$).

Finally, the distorted dumbbell shapes for the horizontal and vertical polarizations of the THG field are consistent with the predictions from the point group symmetry analysis. Since we have used BK7 glass substrate as a reference material, we rule out any anisotropic artifact from the measurements, and we can safely attribute the anisotropic THG to the lattice distortions of ReS_2.

Chapter 7

Two-photon transient absorption microscopy

The two-photon absorption coefficient is an important parameter [178–182] for various nonlinear applications of semiconducting materials, such as saturable absorber for ultrafast pulse lasing [183, 184]. As novel materials, significant efforts have been made to utilize 2D materials as saturable absorbers or laser gain media in laser industry. So far, it has been shown that TMD monolayers, such as MoS_2, have giant two-photon absorption coefficients [185, 186]. Many reports have been announced that various lasers based on 2D materials have been successfully fabricated [187–190]. Comparing with traditional saturable absorbers, 2D materials are as thin as a few atomic layers and can be easily integrated into nano-devices. Due to the promising optoelectronics applications, it is important to measure the two-photon absorption coefficients of 2D materials.

Two-photon absorption is a third-order nonlinear optical effect, which is related to the imaginary part of third-order susceptibility. Two photons are simultaneously absorbed via interband transition in a semiconductor. Typically, the two photons have the same energy. Nondegenerate two-photon absorption is also possible in a semiconductor, but will not be discussed in this dissertation.

Transient absorption can be employed as an effective tool to observe two-photon absorption

in 2D materials. The pump photon energy used in transient absorption is usually higher than the band gap. Hence, one-photon process dominate the absorption, where a carrier density related to the one-photon absorption coefficient will be injected. If we decrease the photon energy of pump laser to be lower than the band gap, two-photon absorption will dominate. With enough power of pump laser, a high carrier density can also be injected.

In the following, we show a new approach to measure two-photon absorption coefficient of 2D materials based on transient absorption measurements. By performing one-photon pumped differential transmission measurements, we establish a relation between the injected carrier density and the magnitude of the differential transmission signal. Then, by measuring the relation between the incident two-photon pump power and the differential transmission signal, we can relate the incident power to the injected carrier density, which is used to calculate the two-photon absorption coefficient.

7.1 Carrier density injected by one-photon absorption

OPA is a linear optical process related to $\chi^{(1)}$. In general, linear absorption coefficient (relation to $\chi^{(1)}$) is used to characterize the one-photon absorption ability of a material.

According to Beer's Law, when laser goes through a thin film sample with a thickness of L,

$$\frac{dI}{dz} = -\alpha I. \tag{7.1}$$

Solving the equation, we find,

$$I(z) = I_0 e^{-\alpha z}, \tag{7.2}$$

where $I(z)$ and I_0 are the light intensity inside the film at a distance z from the surface and incident light intensity just into the surface, respectively. The absorptance of the sample is:

$$\frac{I_{ab}}{I_0} = 1 - e^{-\alpha L}. \tag{7.3}$$

In OPA transient absorption, the differential transmission is directly measured. The absorptance of the sample can be used to convert the energy fluence of the pump pulse to the injected carrier density.

7.2 Carrier density injected by two-photon absorption

Similarly, for TPA, Beer's Law becomes,

$$\frac{dI}{dz} = -\beta I^2. \tag{7.4}$$

The solution is,

$$I(z) = \frac{I_0}{1+\beta I_0 z}. \tag{7.5}$$

The absorbtance of the sample is,

$$\frac{I_{ab}}{I_0} = \frac{\beta I_0 L}{1+\beta I_0 L} \approx \beta I_0 L, \tag{7.6}$$

since $I_{ab} \ll I_0$ and $\beta I_0 L \ll 1$.

In OPA transient absorption, the differential transmission is directly measured. The absorptance of the sample can be used to convert the energy fluence of the pump pulse to the injected carrier density. The only unknown parameter will be the TPA coefficient. Hence, it can be calculated.

7.3 Measurement of two-photon absorption coefficient in monolayer WS_2

7.3.1 TPA coefficients of WS_2 monolayer

A monolayer WS_2 sample is mechanically exfoliated from a bulk flake and transferred to a BK7 glass substrate, as indicated in Figure 7.2 (a). The PL peak is centered at about 620 nm, indicating

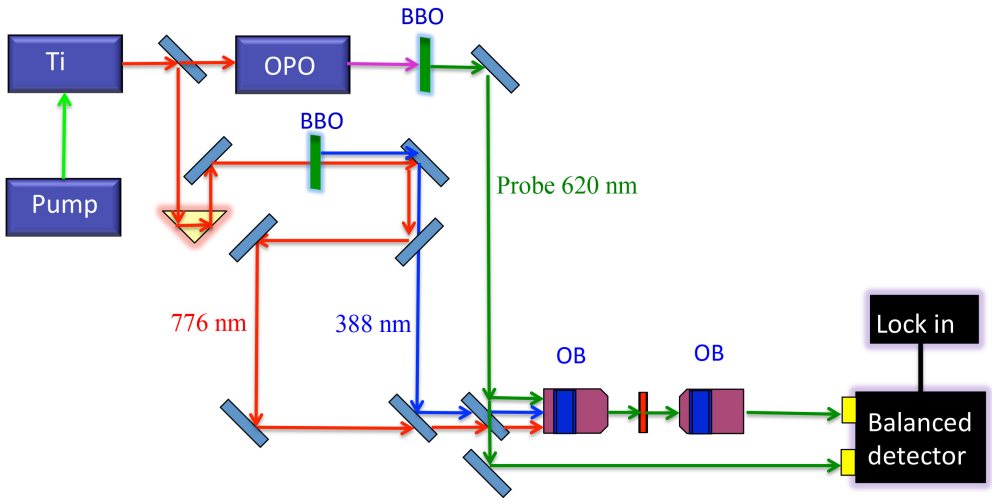

Figure 7.1: Schematic diagram of experimental setup for two-photon transient absorption microscopy.

its monolayer nature, as shown in Figure 7.2 (b). A differential transmission setup is employed to carry out the transient absorption measurements. To enable the ability of measuring OPA and TPA at the same time, three optical paths, including an OPA pump path, a TPA pump path and a probe path, are constructed. The optical lengths of the OPA pump path and the TPA pump path are adjusted to be approximately equal to each other. A Ti: sapphire oscillator generates 776 nm femtosecond pulses with a repetition frequency of 80.48 MHz. With a beamsplitter, one part of 776 nm pulses is focused into a BBO crystal. The induced SHG is sent to the OPA pump path and the residual of 776 nm is sent to TPA pump path. The other part of 776 nm from Ti: sapphire oscillator is used to pump a optical parameter oscillator, signal of which is centered at 1240 nm. Another BBO crystal is used to generate SHG of 1240 nm. The induced SHG centered at 620 nm is sent to the probe path. The optical length of the probe path is controlled by a linear delay stage to match with the pump optical lengths. All three beams are combined by three beamsplitters and focused tightly on the monolayer WS_2 sample by an objective lens with a numerical aperture (NA) of 0.42. The transmitted probe beam is collected by another objective lens with the same NA and delivered to a detector. Balanced and lock-in detections are used to increase signal-to-noise ratio.

In the experiments, we first investigate the differential transmission of the probe under the 388 nm pump only, by blocking the TPA pump path. To control the pump power, a combination of

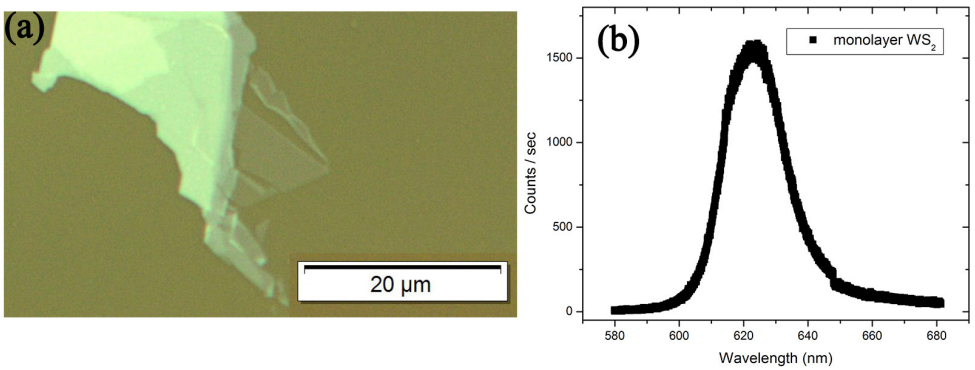

Figure 7.2: (a) Microscope image of mechanically exfoliated monolayer WS_2 sample on a BK7 glass substrate. (b) PL spectrum of the monolayer WS_2 sample.

half-wave plate and polarizer is inserted in the OPA pump path. At various pump powers, temporal scans of probe pulse with respective to pump pulse are obtained, as shown in Figure 7.3 (a). At each OPA pump power, we fit the decay curve by a bi-exponential function. The fast and slow decay components are found to constant, which are 1.5 $\pm$ 0.5 ps and 18 $\pm$ 1 ps, respectively. At 0 ps, we plot the differential transmission signals as a function of OPA pump powers, as shown in Figure 7.3 (b). When the OPA power is smaller than 0.6 μW, the differential transmission signals present a linear dependence on the OPA pump powers. A saturation behavior can be observed when the OPA pump power gets larger than 0.6 μW. Overall, the OPA pump power dependence is sublinear, indicated by the redline in Figure 7.3 (b).

To make the injected carrier density comparable to TPA measurement, we use the data when OPA pump power is 1.0 μW, which falls in the linear range of OPA pump power dependence. The thickness of monolayer WS_2, L = 0.75 nm has been measured elsewhere [191]. Assuming one 388 nm photon absorbed will excite one electron to the conduction band, and using the linear absorption coefficient $\alpha = 2.3\times10^8$ m^{-1} [77, 192], the absorptance at 0 ps can be calcuated by Equation 7.3 as: $\frac{I_{ab}}{I_0} = 1 - e^{-\alpha L} = 15.8\%$.

Next, we block the 388 nm optical path and investigate the TPA with 776 nm beam as the pump. Every other conditions are kept the same as OPA measurements. The pump power of 776 nm beam is also adjusted by a combination of half-wave plate and polarizer. Similarly, at various pump powers, temporal scans of probe pulse with respective to pump pulse are obtained,

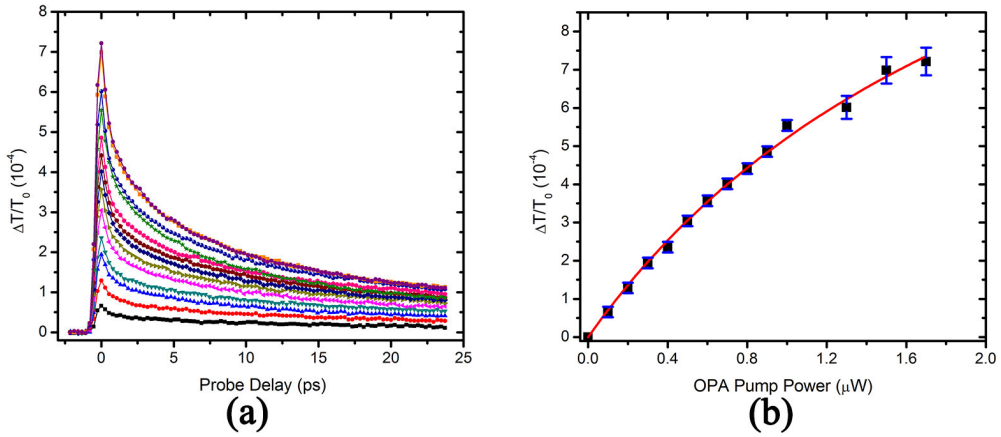

Figure 7.3: (a) OPA pump power dependence of temporal scan in the monolayer WS_2 sample. The pump powers of 388 nm beam (from bottom to top) are 0.1, 0.2, 0.3, 0.4, 0.5, 0.6, 0.7, 0.8, 0.9, 1.0, 1.3, 1.5 and 1.7 μW. (b) At 0 ps, the differential transmission signals (black suqares) as a function of TPA pump power. The redline is a sublinear fitting.

as shown in Figure 7.4 (a). Before the zero delay, a set of negative dips can be clearly observed, which are different from OPA results. These negative dips are induced by nondegenerate two-photon absorption. One 776 nm photon from the pump and one 620 nm photon from the probe are simultaneously absorbed. The negative dip is a direct measurement of the depletion of probe power, that is the differential probe power loss caused by absorption before zero delay. It should be emphasized that the negative dips are Gaussian because they are the convolution of pump and probe pulse in the time domain and will not affect the shape of decay curves after zero delay. On the other hand, it should be noticed that nondegenerate two-photon absorption channel can also inject electrons to conduction band and induce a carrier density after zero delay. However, in our measurement, the probe power is about three order of magnitude smaller than the TPA pump powers. Therefore, the contribution to total carrier density can be neglected, comparing with the degenerate TPA.

At 0 ps, the differential transmission signals are plotted as a function of TPA pump powers, as shown in Figure 7.4 (b). The red line is a quadratic fitting, which agrees well with the experimental data. Hence, it can be confirmed that the differential transmission signal is induced by TPA.

The sample will have no memory of what pump laser is used. The physical processes after zero delay should be the same for OPA and TPA. Hence, the injected carrier density is a parameter

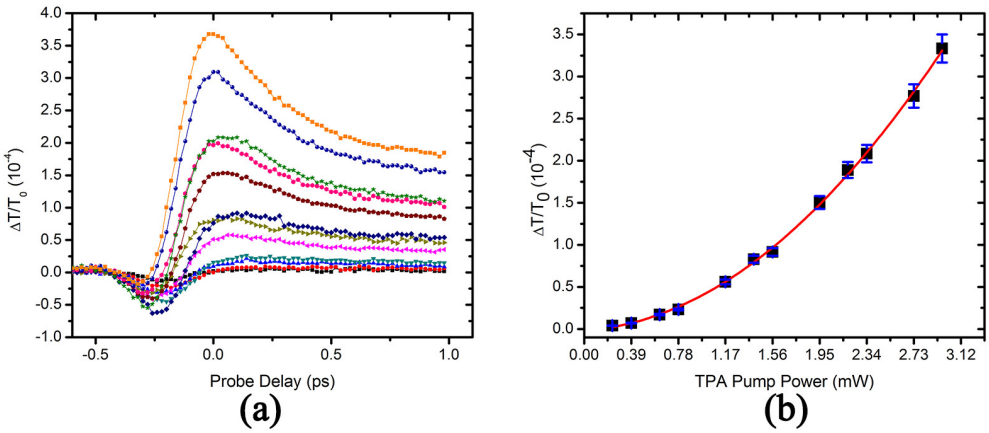

Figure 7.4: (a) TPA pump power dependence of temporal scan in the monolayer WS_2 sample. The pump powers of 776 nm beam (from bottom to top) are 0.23, 0.39, 0.62, 0.78, 1.17, 1.40, 1.56, 1.95, 2.18, 2.34, 2.73, and 2.96 mW. (b) At 0 ps, the differential transmission signals (black squares) as a function of TPA pump power. The red line is a square fitting.

that is equivalent for both OPA and TPA measurements. By the injected carrier density obtained in OPA measurement, we can get the injected carrier density in TPA measurement, by scaling the two 0 ps transient absorptance in OPA and TPA. According to,

$$\frac{I_{ab}}{I_0} = 1 - e^{-\alpha L}, \tag{7.7}$$

in the linear regime, the absorptance will remain a constant, about 15.8 %, which should not be confused with the transient absorption of the probe. The probing is described by:

$$\frac{\Delta T}{T_0} = A\frac{N}{N_0}. \tag{7.8}$$

At 0 ps and OPA pump power 1.0 μW, the $\frac{\Delta T}{T_0} = 5.5 \times 10^{-4}$ is proportional to the injected carrier density, where the absorbed power is, P_1 = 1 μW$\times$15.8 % = 0.158 μW.

Since the TPA pump powers are about three order of magnitude higher than OPA pump powers, thermal effects can also induce a signal after zero delay. It is very clear if we compare the OPA temporal scan with the TPA temporal scan, as shown in Figure 7.5 (a) and (b), respectively. When OPA pump power is 1.0 μW, we fit the decay curve with a bi-exponential function, resulting in a fast decay time of about 1.4 ps and a slow decay time of about 18 ps. These two decay time

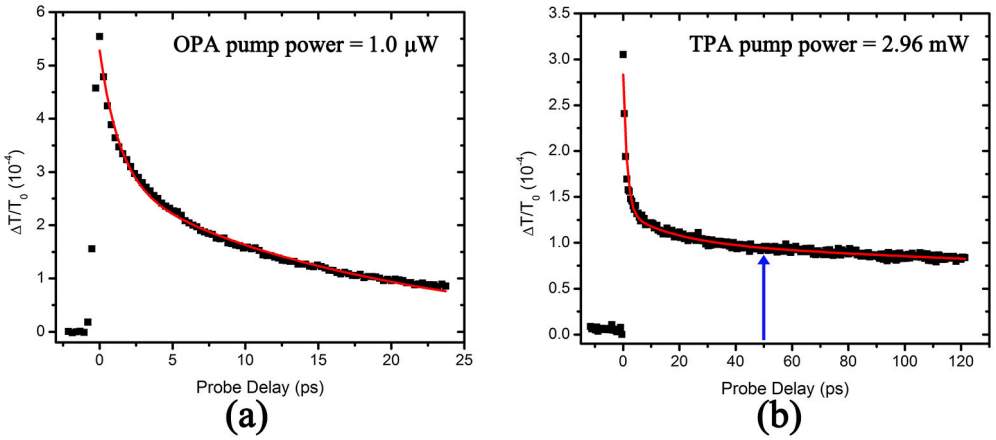

Figure 7.5: (a) Temporal decay of differential transmission signal when OPA pump power is 1.0 μW. The red line is a bi-exponential fitting. (b) Temporal decay of differential transmission signal when TPA pump power is 2.96 mW. The red line is a tri-exponential fitting. The blow arrow is a mark to indicate the thermal contribution after 50 ps.

agree well with previously reported results in monolayer WS_2. However, in TPA measurements, the thermal effects will lead to a residual in the temporal decay curve. From Figure 7.5 (b), after 50 ps indicated by the blue arrow, the differential transmission signal does not reach zero, but still remain about 33 % of the peak at 0 ps. To reveal the thermal component of the temporal decay, we fit the TPA temporal-scanning curve with a tri-exponential function. The first and second decay time are set the same as obtained results from Figure 7.5 (a). The decay time of thermal effects is found to be 620 ps.

At 0 ps and TPA pump power P_2 = 2.96 mW, $\frac{\Delta T}{T_0} = 3.3 \times 10^{-4}$. The contribution of thermal effects is about 33 % as discussed above. Hence, the contribution of injected carrier density will be $0.66\frac{\Delta T}{T_0} = 2.2 \times 10^{-4}$. By scaling the TPA differential transmission by the OPA differential transmission at 0 ps, the absorptance of 776 nm can be calculated as: $\frac{I_{ab}^{TPA}}{I_0^{TPA}} = \frac{2.2}{5.5} \times \frac{0.158\mu W}{2.96mW} \approx 2.14\times10^{-5}$. The peak intensity of the 776 nm pump pulse can be calculated as,

$$I_0 = \frac{P_2}{\tau f \pi w^2}, \tag{7.9}$$

where the temporal width of the 776 nm pump pulse $\tau \approx 200$ fs, pulse repetition frequency $f \approx 80.48$ MHz, and laser spot size $w \approx 2.7$ μm, pointing to $I_0 \approx 0.835$ GW cm^{-2}. Finally, according

to Equation 7.6, we further calculate the two-photon absorption coefficient of our monolayer WS_2 sample, $\beta \approx 340 \pm 30$ cm/GW.

7.3.2 Discussion

High TPA coefficient is desired for the application of saturable absorbers. TPA coefficient of monolayer WS_2 we measured is about two order of magnitude higher that of traditional semiconductors, such as Si: 1.5 cm/GW [181], ZnO: 5 cm/GW [193], and GaAs: 26 cm/GW [194, 195]. Our results confirm that monolayer WS_2 processes giant two-photon absorption coefficient, which can serve as an outstanding material for saturable absorber applications, for instance Q-switching. Furthermore, we notice that z-scan has been used to measure the two-photon absorption coefficient of WS_2 by Jun Wang's group in Shanghai Institute of Optics and Fine Mechanics. With 800nm, 1 kHz, 40 fs ultrafast laser, they reported β = 525 $\pm$ 205 cm/GW for 1-3 L WS_2 [191]. Their results are consistent with our results, since our pump laser wavelength is at 776 nm. In addition, we point out that z-scan measurements need large and uniform samples, which are not required by the two-photon transient absorption microscopy we have illustrated. Therefore, we conclude that two-photon transient absorption microscopy is an effective nonlinear optical spectroscopy to evaluate the two-photon absorption process of 2D materials.

Chapter 8

Conclusion

In conclusion, I have comprehensively investigated nonlinear optical properties and their underlying physics of 2D materials, by carrying out experiments and addressing five kinds of nonlinear optical spectroscopy with ultrafast lasers. My experimental results not only provide valuable information of nonlinear optical properties of 2D materials ranging from spatiotemporal dynamics to third-order nonlinearity, but also reveal novel 2D physics, such as in-plane anisotropic third-order susceptibility of monolayer ReS_2 induced by lattice distortion.

By transient absorption microscopy, I first resolve the saturable absorption of 2D excitons in both time and space. By comparing the excitonic dynamics of monolayer and bulk WSe_2, I show the lifetime of 2D excitons is shorter than that of 3D excitons. Diffusive transport properties of 2D excitons in WSe_2, such as mobility, are comparable to traditional semiconductor silicon. Furthermore, 2D excitons in a special TMD monolayer ReS_2 with a distorted $1T$ lattice structure, possess anisotropic diffusive transport properties. The in-plane anisotropic factor of 2D exciton diffusion is directly measured to be about 3, which adds a new in-plane anisotropic degree of freedom for 2D semiconducting materials.

By quantum interference and control nanoscopy, I illustrate the coherent control of nanoscale ballistic current in a ReS_2 thin film, taking advantage of quantum interference between one-photon absorption and two-photon absorption transition paths. The ballistic transport length of electrons

in ReS_2 is smaller than 1 nm, indicating 2D materials are promising to realize novel nanoscale-devices with ultralow heat dissipation.

By second harmonic generation microscopy, we investigate the second-order nonlinearity of monolayer MoS_2. The second-order susceptibility is effectively measured. More importantly, the in-plane angular dependence of SHG depends on the hexagonal lattice structure and presents a six-fold symmetry, indicating SHG microscopy can serve as a powerful tool to characterize the crystalline direction of TMD monolayers.

By third harmonic generation microscopy, I investigate the third-order nonlinearity of ReS_2. Strong and anisotropic third harmonic generation is observed in monolayer and multilayer ReS_2. The third-order susceptibility is about one-order of magnitude higher than of the hexagonal monolayers, such as, MoS_2. The anisotropic third harmonic generation is attributed to the lattice distortion of ReS_2 by a symmetry analysis of an undistorted $1T$ lattice and using the BK7 glass substrate as a reference material.

By two-photon transient absorption microscopy, we measure the two-photon absorption coefficient of monolayer WS_2, which is about two-order of magnitude higher than that of traditional semiconducting materials, such as silicon. The observed giant two-photon absorption coefficient demonstrates 2D materials, such as monolayer WS_2, can be utilized as ideal saturable absorbers for nanophotonics applications.

My experimental results will play important roles of developing nanophotonics applications with 2D materials, especially 2D flexible devices as thin as a few atomic layers. One research area in which nonlinear optical responses of 2D layers realizing bio-sensing functions, such as blood pressure and heartbeat rate, has been recently brought up. What's more, we point out that our techniques are not only limited to presented 2D materials, but also effective for complicated 2D systems. For example, to obtain information of indirect excitons, the nonlinear optical properties of van der Waals heterostructures formed by combining different 2D materials will be another interesting research area to explore. At last, we hope our techniques stimulate more nonlinear optical studies of 2D materials in the future, as the horizon of 2D physics keeps expanding.

References

[1] Kostya S Novoselov, Andre K Geim, Sergei V Morozov, D Jiang, Y Zhang, Sergey V Dubonos, Irina V Grigorieva, and Alexandr A Firsov. Electric field effect in atomically thin carbon films. *Science*, 306(5696):666–669, 2004.

[2] K. S. Novoselov, A. K. Geim, S. V. Morozov, D. Jiang, M. I. Katsnelson, I. V. Grigorieva, S. V. Dubonos, and A. A. Firsov. Two-dimensional gas of massless Dirac fermions in graphene. *Nature*, 438(7065):197–200, 2005.

[3] Yuanbo Zhang, Yan-Wen Tan, Horst L Stormer, and Philip Kim. Experimental observation of the quantum Hall effect and Berry's phase in graphene. *Nature*, 438(7065):201–204, 2005.

[4] Charles L Kane and Eugene J Mele. Quantum spin Hall effect in graphene. *Phys. Rev. Lett.*, 95(22):226801, 2005.

[5] Andre K Geim and Konstantin S Novoselov. The rise of graphene. *Nat. Mater.*, 6(3):183–191, 2007.

[6] AH Castro Neto, F Guinea, Nuno MR Peres, Kostya S Novoselov, and Andre K Geim. The electronic properties of graphene. *Rev. Mod. Phys.*, 81(1):109, 2009.

[7] Alexander A Balandin, Suchismita Ghosh, Wenzhong Bao, Irene Calizo, Desalegne Teweldebrhan, Feng Miao, and Chun Ning Lau. Superior thermal conductivity of single-layer graphene. *Nano Lett.*, 8(3):902–907, 2008.

[8] Daniel R Dreyer, Sungjin Park, Christopher W Bielawski, and Rodney S Ruoff. The chemistry of graphene oxide. *Chem. Soc. Rev.*, 39(1):228–240, 2010.

[9] Fengnian Xia, Han Wang, Di Xiao, Madan Dubey, and Ashwin Ramasubramaniam. Two-dimensional material nanophotonics. *Nat. Photonics*, 8(12):899–907, 2014.

[10] Kin Fai Mak, Changgu Lee, James Hone, Jie Shan, and Tony F. Heinz. Atomically thin MoS_2: a new direct-gap semiconductor. *Phys. Rev. Lett.*, 105(13):136805, 2010.

[11] Andrea Splendiani, Liang Sun, Yuanbo Zhang, Tianshu Li, Jonghwan Kim, Chi-Yung Chim, Giulia Galli, and Feng Wang. Emerging photoluminescence in monolayer MoS_2. *Nano Lett.*, 10(4):1271–1275, 2010.

[12] Branimir Radisavljevic, Aleksandra Radenovic, Jacopo Brivio, i V Giacometti, and A Kis. Single-layer MoS_2 transistors. *Nat. Nanotechnol.*, 6(3):147–150, 2011.

[13] Matin Amani, Der-Hsien Lien, Daisuke Kiriya, Jun Xiao, Angelica Azcatl, Jiyoung Noh, Surabhi R Madhvapathy, Rafik Addou, KC Santosh, Madan Dubey, et al. Near-unity photoluminescence quantum yield in MoS_2. *Science*, 350(6264):1065–1068, 2015.

[14] Zongyou Yin, Hai Li, Hong Li, Lin Jiang, Yumeng Shi, Yinghui Sun, Gang Lu, Qing Zhang, Xiaodong Chen, and Hua Zhang. Single-layer MoS_2 phototransistors. *ACS Nano*, 6(1):74–80, 2011.

[15] Andrea C Ferrari, Francesco Bonaccorso, Vladimir Fal'Ko, Konstantin S Novoselov, Stephan Roche, Peter Bøggild, Stefano Borini, Frank HL Koppens, Vincenzo Palermo, Nicola Pugno, et al. Science and technology roadmap for graphene, related two-dimensional crystals, and hybrid systems. *Nanoscale*, 7(11):4598–4810, 2015.

[16] Ruben Mas-Balleste, Cristina Gomez-Navarro, Julio Gomez-Herrero, and Felix Zamora. 2d materials: to graphene and beyond. *Nanoscale*, 3(1):20–30, 2011.

[17] Manish Chhowalla, Hyeon Suk Shin, Goki Eda, Lain-Jong Li, Kian Ping Loh, and Hua Zhang. The chemistry of two-dimensional layered transition metal dichalcogenide nanosheets. *Nat. Chem.*, 5(4):263–275, 2013.

[18] Sheneve Z Butler, Shawna M Hollen, Linyou Cao, Yi Cui, Jay A Gupta, Humberto R Gutiérrez, Tony F Heinz, Seung Sae Hong, Jiaxing Huang, Ariel F Ismach, et al. Progress, challenges, and opportunities in two-dimensional materials beyond graphene. *ACS Nano*, 7(4):2898–2926, 2013.

[19] Mingsheng Xu, Tao Liang, Minmin Shi, and Hongzheng Chen. Graphene-like two-dimensional materials. *Chem. Rev.*, 113(5):3766–3798, 2013.

[20] Francesco Bonaccorso, Z Sun, Ta Hasan, and AC Ferrari. Graphene photonics and optoelectronics. *Nat. Photonics*, 4(9):611–622, 2010.

[21] Francesco Bonaccorso, Luigi Colombo, Guihua Yu, Meryl Stoller, Valentina Tozzini, Andrea C Ferrari, Rodney S Ruoff, and Vittorio Pellegrini. Graphene, related two-dimensional crystals, and hybrid systems for energy conversion and storage. *Science*, 347(6217):1246501, 2015.

[22] Kin Fai Mak, Keliang He, Jie Shan, and Tony F Heinz. Control of valley polarization in monolayer MoS_2 by optical helicity. *Nat. Nanotechnol.*, 7(8):494–498, 2012.

[23] Oriol Lopez-Sanchez, Dominik Lembke, Metin Kayci, Aleksandra Radenovic, and Andras Kis. Ultrasensitive photodetectors based on monolayer MoS_2. *Nat. Nanotechnol.*, 8(7):497–501, 2013.

[24] Ting Cao, Gang Wang, Wenpeng Han, Huiqi Ye, Chuanrui Zhu, Junren Shi, Qian Niu, Pingheng Tan, Enge Wang, Baoli Liu, et al. Valley-selective circular dichroism of monolayer molybdenum disulphide. *Nat. Commun.*, 3:887, 2012.

[25] Han Wang, Lili Yu, Yi-Hsien Lee, Yumeng Shi, Allen Hsu, Matthew L Chin, Lain-Jong Li, Madan Dubey, Jing Kong, and Tomas Palacios. Integrated circuits based on bilayer MoS_2 transistors. *Nano Lett.*, 12(9):4674–4680, 2012.

[26] Kin Fai Mak, Keliang He, Changgu Lee, Gwan Hyoung Lee, James Hone, Tony F Heinz, and Jie Shan. Tightly bound trions in monolayer MoS_2. *Nat. Mater.*, 12(3):207–211, 2013.

[27] Simone Bertolazzi, Jacopo Brivio, and Andras Kis. Stretching and breaking of ultrathin MoS_2. *ACS Nano*, 5(12):9703–9709, 2011.

[28] Shaul Mukamel. *Principles of nonlinear optical spectroscopy*. Number 6. Oxford University Press on Demand, 1999.

[29] Qing Hua Wang, Kourosh Kalantar-Zadeh, Andras Kis, Jonathan N Coleman, and Michael S Strano. Electronics and optoelectronics of two-dimensional transition metal dichalcogenides. *Nat. Nanotechnol.*, 7(11):699–712, 2012.

[30] Ashwin Ramasubramaniam. Large excitonic effects in monolayers of molybdenum and tungsten dichalcogenides. *Phys. Rev. B*, 86(11):115409, 2012.

[31] Kin Fai Mak and Jie Shan. Photonics and optoelectronics of 2D semiconductor transition metal dichalcogenides. *Nat. Photonics*, 10(4):216–226, 2016.

[32] Chris Toumey. *Less is moore*. PhD thesis, Nature Publishing Group, 2016.

[33] Di Xiao, Gui-Bin Liu, Wanxiang Feng, Xiaodong Xu, and Wang Yao. Coupled spin and valley physics in monolayers of MoS_2 and other group-VI dichalcogenides. *Phys. Rev. Lett*, 108(19):196802, 2012.

[34] John R Schaibley, Hongyi Yu, Genevieve Clark, Pasqual Rivera, Jason S Ross, Kyle L Seyler, Wang Yao, and Xiaodong Xu. Valleytronics in 2D materials. *Nat. Rev. Mater.*, 1:16055, 2016.

[35] Hui Zhao, Xinyu Pan, Arthur L Smirl, RDR Bhat, Ali Najmaie, JE Sipe, and HM Van Driel. Injection of ballistic pure spin currents in semiconductors by a single-color linearly polarized beam. *Phys. Rev. B*, 72(20):201302, 2005.

[36] Qiannan Cui and Hui Zhao. Coherent control of nanoscale ballistic currents in transition metal dichalcogenide ReS_2. *ACS Nano*, 9(4):3935–3941, 2015.

[37] Hermann A Haus. Theory of mode locking with a fast saturable absorber. *J. Appl. Phys.*, 46(7):3049–3058, 1975.

[38] Melinda Y Han, Barbaros Özyilmaz, Yuanbo Zhang, and Philip Kim. Energy band-gap engineering of graphene nanoribbons. *Phys. Rev. Lett.*, 98(20):206805, 2007.

[39] Yuanbo Zhang, Tsung-Ta Tang, Caglar Girit, Zhao Hao, Michael C Martin, Alex Zettl, Michael F Crommie, Y Ron Shen, and Feng Wang. Direct observation of a widely tunable bandgap in bilayer graphene. *Nature*, 459(7248):820–823, 2009.

[40] Qing Hua Wang, Kourosh Kalantar-Zadeh, Andras Kis, Jonathan N Coleman, and Michael S Strano. Electronics and optoelectronics of two-dimensional transition metal dichalcogenides. *Nat. Nanotechnol.*, 7(11):699–712, 2012.

[41] Manish Chhowalla, Hyeon Suk Shin, Goki Eda, Lain-Jong Li, Kian Ping Loh, and Hua Zhang. The chemistry of two-dimensional layered transition metal dichalcogenide nanosheets. *Nat. Chem.*, 5(4):263–275, 2013.

[42] Nardeep Kumar, Sina Najmaei, Qiannan Cui, Frank Ceballos, Pulickel M. Ajayan, Jun Lou, and Hui Zhao. Second harmonic microscopy of monolayer MoS_2. *Phys. Rev. B*, 87(16):161403, 2013.

[43] Keliang He, Nardeep Kumar, Liang Zhao, Zefang Wang, Kin Fai Mak, Hui Zhao, and Jie Shan. Tightly bound excitons in monolayer WSe_2. *Phys. Rev. Lett.*, 113(2):026803, 2014.

[44] Di Xiao, Gui-Bin Liu, Wanxiang Feng, Xiaodong Xu, and Wang Yao. Coupled spin and valley physics in monolayers of MoS_2 and other group-VI dichalcogenides. *Phys. Rev. Lett.*, 108(19):196802, 2012.

[45] Cory R Dean, Andrea F Young, Inanc Meric, Chris Lee, Lei Wang, S Sorgenfrei, K Watanabe, T Taniguchi, P Kim, KL Shepard, et al. Boron nitride substrates for high-quality graphene electronics. *Nat. Nanotechnol.*, 5(10):722–726, 2010.

[46] D Pacile, JC Meyer, ÇÖ Girit, and A Zettl. The two-dimensional phase of boron nitride: few-atomic-layer sheets and suspended membranes. *Appl. Phys. Lett.*, 92(13):133107, 2008.

[47] Likai Li, Yijun Yu, Guo Jun Ye, Qingqin Ge, Xuedong Ou, Hua Wu, Donglai Feng, Xian Hui Chen, and Yuanbo Zhang. Black phosphorus field-effect transistors. *Nat. Nanotechnol.*, 9(5):372–377, 2014.

[48] Fengnian Xia, Han Wang, and Yichen Jia. Rediscovering black phosphorus as an anisotropic layered material for optoelectronics and electronics. *Nat. Commun.*, 5, 2014.

[49] Jingsi Qiao, Xianghua Kong, Zhi-Xin Hu, Feng Yang, and Wei Ji. High-mobility transport anisotropy and linear dichroism in few-layer black phosphorus. *Nat. Commun.*, 5, 2014.

[50] Andre K Geim and Irina V Grigorieva. Van der Waals heterostructures. *Nature*, 499(7459):419–425, 2013.

[51] Jonathan N Coleman, Mustafa Lotya, Arlene O?Neill, Shane D Bergin, Paul J King, Umar Khan, Karen Young, Alexandre Gaucher, Sukanta De, Ronan J Smith, et al. Two-dimensional nanosheets produced by liquid exfoliation of layered materials. *Science*, 331(6017):568–571, 2011.

[52] Meihua Jin, Hae-Kyung Jeong, Tae-Hyung Kim, Kang Pyo So, Yan Cui, Woo Jong Yu, Eun Ju Ra, and Young Hee Lee. Synthesis and systematic characterization of functionalized

graphene sheets generated by thermal exfoliation at low temperature. *J. Phys. D: Appl. Phys.*, 43(27):275402, 2010.

[53] Andres Castellanos-Gomez, Michele Buscema, Rianda Molenaar, Vibhor Singh, Laurens Janssen, Herre SJ van der Zant, and Gary A Steele. Deterministic transfer of two-dimensional materials by all-dry viscoelastic stamping. *2D Mater.*, 1(1):011002, 2014.

[54] Yi Zhang, Luyao Zhang, and Chongwu Zhou. Review of chemical vapor deposition of graphene and related applications. *Acc. Chem. Res.*, 46(10):2329–2339, 2013.

[55] Yongjie Zhan, Zheng Liu, Sina Najmaei, Pulickel M Ajayan, and Jun Lou. Large-area vapor-phase growth and characterization of MoS_2 atomic layers on a SiO_2 substrate. *Small*, 8(7):966–971, 2012.

[56] Yi-Hsien Lee, Xin-Quan Zhang, Wenjing Zhang, Mu-Tung Chang, Cheng-Te Lin, Kai-Di Chang, Ya-Chu Yu, Jacob Tse-Wei Wang, Chia-Seng Chang, Lain-Jong Li, et al. Synthesis of large-area MoS_2 atomic layers with chemical vapor deposition. *Adv. Mater.*, 24(17):2320–2325, 2012.

[57] Sefaattin Tongay, Wen Fan, Jun Kang, Joonsuk Park, Unsal Koldemir, Joonki Suh, Deepa S Narang, Kai Liu, Jie Ji, Jingbo Li, et al. Tuning interlayer coupling in large-area heterostructures with CVD-grown MoS_2 and WS_2 monolayers. *Nano Lett.*, 14(6):3185–3190, 2014.

[58] Yexin Deng, Zhe Luo, Nathan J Conrad, Han Liu, Yongji Gong, Sina Najmaei, Pulickel M Ajayan, Jun Lou, Xianfan Xu, and Peide D Ye. Black phosphorus-monolayer MoS_2 van der Waals heterojunction p-n diode. *ACS Nano*, 8(8):8292–8299, 2014.

[59] Sanfeng Wu, Chunming Huang, Grant Aivazian, Jason S Ross, David H Cobden, and Xiaodong Xu. Vapor-solid growth of high optical quality MoS_2 monolayers with near-unity valley polarization. *ACS Nano*, 7(3):2768–2772, 2013.

[60] Andres Castellanos-Gomez, Maria Barkelid, AM Goossens, Victor E Calado, Herre SJ van der Zant, and Gary A Steele. Laser-thinning of MoS_2: on demand generation of a single-layer semiconductor. *Nano Lett.*, 12(6):3187–3192, 2012.

[61] A Davydov. *Theory of molecular excitons*. Springer, 2013.

[62] RJ Elliott. Intensity of optical absorption by excitons. *Physical Review*, 108(6):1384, 1957.

[63] Tianhao Zhang. *Optical two-dimensional Fourier transform spectroscopy of semiconductors*. ProQuest, 2008.

[64] Alexey Chernikov, Timothy C Berkelbach, Heather M Hill, Albert Rigosi, Yilei Li, Ozgur Burak Aslan, David R Reichman, Mark S Hybertsen, and Tony F Heinz. Exciton binding energy and nonhydrogenic Rydberg series in monolayer WS_2. *Phys. Rev. Lett*, 113(7):076802, 2014.

[65] Timothy C Berkelbach, Mark S Hybertsen, and David R Reichman. Theory of neutral and charged excitons in monolayer transition metal dichalcogenides. *Phys. Rev. B*, 88(4):045318, 2013.

[66] E Cappelluti, Rafael Roldán, JA Silva-Guillén, Pablo Ordejón, and F Guinea. Tight-binding model and direct-gap/indirect-gap transition in single-layer and multilayer MoS_2. *Phys. Rev. B*, 88(7):075409, 2013.

[67] Habib Rostami, Ali G Moghaddam, and Reza Asgari. Effective lattice Hamiltonian for monolayer MoS_2: Tailoring electronic structure with perpendicular electric and magnetic fields. *Phys. Rev. B*, 88(8):085440, 2013.

[68] Andor Kormányos, Viktor Zólyomi, Neil D Drummond, Péter Rakyta, Guido Burkard, and Vladimir I Fal'ko. Monolayer MoS_2: Trigonal warping, the γ valley, and spin-orbit coupling effects. *Phys. Rev. B*, 88(4):045416, 2013.

[69] Wang Yao, Di Xiao, and Qian Niu. Valley-dependent optoelectronics from inversion symmetry breaking. *Phys. Rev. B*, 77(23):235406, 2008.

[70] Jagdeep Shah. *Ultrafast spectroscopy of semiconductors and semiconductor nanostructures*, volume 115. Springer Science & Business Media, 2013.

[71] Robert W Boyd. *Nonlinear optics*. Academic press, 2003.

[72] D Crichton Hutchings, M Sheik-Bahae, David J Hagan, and Eric W Van Stryland. Kramers-Krönig relations in nonlinear optics. *Opt. Quantum Electron.*, 24(1):1–30, 1992.

[73] Richard L Sutherland. *Handbook of nonlinear optics*. CRC press, 2003.

[74] M Combescot and Ph Nozieres. Condensation of excitons in germanium and silicon. *J. Phys. C: Solid State Phys.*, 5(17):2369, 1972.

[75] S Schmitt-Rink, DS Chemla, and DAB Miller. Theory of transient excitonic optical nonlinearities in semiconductor quantum-well structures. *Phys. Rev. B*, 32(10):6601, 1985.

[76] KJ Painter and T Hillen. Mathematical modelling of glioma growth: the use of diffusion tensor imaging (dti) data to predict the anisotropic pathways of cancer invasion. *J. Theor. Biol.*, 323:25–39, 2013.

[77] Weijie Zhao, Zohreh Ghorannevis, Leiqiang Chu, Minglin Toh, Christian Kloc, Ping-Heng Tan, and Goki Eda. Evolution of electronic structure in atomically thin sheets of WS_2 and WSe_2. *ACS Nano*, 7(1):791–797, 2012.

[78] AR Beal, WY Liang, and HP Hughes. Kramers-Kronig analysis of the reflectivity spectra of 3R-WS_2 and 2H-WSe_2. *J. Phys. C: Solid State Phys.*, 9(12):2449, 1976.

[79] R Coehoorn, C Haas, J Dijkstra, CJF Flipse, RA De Groot, and A Wold. Electronic structure of $MoSe_2$, MoS_2, and WSe_2. i. band-structure calculations and photoelectron spectroscopy. *Phys. Rev. B*, 35(12):6195, 1987.

[80] R Coehoorn, C Haas, and RA De Groot. Electronic structure of $MoSe_2$, MoS_2, and WSe_2. ii. the nature of the optical band gaps. *Phys. Rev. B*, 35(12):6203, 1987.

[81] HJ Lewerenz, A Heller, and FJ DiSalvo. Relationship between surface morphology and solar conversion efficiency of tungsten diselenide photoanodes. *J. Am. Chem. Soc.*, 102(6):1877–1880, 1980.

[82] R Tenne and A Wold. Passivation of recombination centers in n-WSe_2 yields high efficiency (> 14%) photoelectrochemical cell. *Appl. Phys. Lett.*, 47(7):707–709, 1985.

[83] G Prasad and ON Srivastava. The high-efficiency (17.1%) wse2 photo-electrochemical solar cell. *J. Phys. D: Appl. Phys.*, 21(6):1028, 1988.

[84] Adam P. Pieterick Harry B. Gray McKone, James R. and Nathan S. Lewis. Hydrogen evolution from Pt/Ru-coated p-type WSe_2 photocathodes. *J. Am. Chem. Soc.*, 135(1):223–231, 2013.

[85] F Consadori and RF Frindt. Crystal size effects on the exciton absorption spectrum of WSe_2. *Phys. Rev. B*, 2(12):4893, 1970.

[86] Hui Fang, Steven Chuang, Ting Chia Chang, Kuniharu Takei, Toshitake Takahashi, and Ali Javey. High-performance single layered WSe_2 p-FETs with chemically doped contacts. *Nano Lett.*, 12(7):3788–3792, 2012.

[87] ZY Zhu, YC Cheng, and Udo Schwingenschlögl. Giant spin-orbit-induced spin splitting in two-dimensional transition-metal dichalcogenide semiconductors. *Phys. Rev. B*, 84(15):153402, 2011.

[88] Hongtao Yuan, Mohammad Saeed Bahramy, Kazuhiro Morimoto, Sanfeng Wu, Kentaro Nomura, Bohm-Jung Yang, Hidekazu Shimotani, Ryuji Suzuki, Minglin Toh, Christian Kloc, et al. Zeeman-type spin splitting controlled by an electric field. *Nat. Phys.*, 9(9):563–569, 2013.

[89] Aaron M Jones, Hongyi Yu, Nirmal J Ghimire, Sanfeng Wu, Grant Aivazian, Jason S Ross, Bo Zhao, Jiaqiang Yan, David G Mandrus, Di Xiao, et al. Optical generation of excitonic valley coherence in monolayer WSe_2. *Nat. Nanotechnol.*, 8(9):634–638, 2013.

[90] Aaron M Jones, Hongyi Yu, Jason S Ross, Philip Klement, Nirmal J Ghimire, Jiaqiang Yan, David G Mandrus, Wang Yao, and Xiaodong Xu. Spin-layer locking effects in optical orientation of exciton spin in bilayer WSe_2. *Nat. Phys.*, 10(2):130–134, 2014.

[91] Hongtao Yuan, Xinqiang Wang, Biao Lian, Haijun Zhang, Xianfa Fang, Bo Shen, Gang Xu, Yong Xu, Shou-Cheng Zhang, Harold Y Hwang, et al. Generation and electric control of spin-valley-coupled circular photogalvanic current in WSe_2. *Nat. Nanotechnol.*, 9(10):851–857, 2014.

[92] Catalin Chiritescu, David G Cahill, Ngoc Nguyen, David Johnson, Arun Bodapati, Pawel Keblinski, and Paul Zschack. Ultralow thermal conductivity in disordered, layered WSe_2 crystals. *Science*, 315(5810):351–353, 2007.

[93] Vivekanand V Gobre and Alexandre Tkatchenko. Scaling laws for van der waals interactions in nanostructured materials. *Nat. Commun.*, 4, 2013.

[94] Liam Britnell, RM Ribeiro, A Eckmann, R Jalil, BD Belle, A Mishchenko, Y-J Kim, RV Gorbachev, T Georgiou, SV Morozov, et al. Strong light-matter interactions in heterostructures of atomically thin films. *Science*, 340(6138):1311–1314, 2013.

[95] Thanasis Georgiou, Rashid Jalil, Branson D Belle, Liam Britnell, Roman V Gorbachev, Sergey V Morozov, Yong-Jin Kim, Ali Gholinia, Sarah J Haigh, Oleg Makarovsky, et al. Vertical field-effect transistor based on graphene-WS_2 heterostructures for flexible and transparent electronics. *Nat. Nanotechnol.*, 8(2):100–103, 2013.

[96] L Britnell, RV Gorbachev, R Jalil, BD Belle, F Schedin, A Mishchenko, T Georgiou, MI Katsnelson, L Eaves, SV Morozov, et al. Field-effect tunneling transistor based on vertical graphene heterostructures. *Science*, 335(6071):947–950, 2012.

[97] Qiannan Cui, Frank Ceballos, Nardeep Kumar, and Hui Zhao. Transient absorption microscopy of monolayer and bulk WSe_2. *ACS Nano*, 8(3):2970–2976, 2014.

[98] Philipp Tonndorf, Robert Schmidt, Philipp Böttger, Xiao Zhang, Janna Börner, Andreas Liebig, Manfred Albrecht, Christian Kloc, Ovidiu Gordan, Dietrich RT Zahn, et al. Photoluminescence emission and raman response of monolayer MoS_2, $MoSe_2$, and WSe_2. *Opt. Express*, 21(4):4908–4916, 2013.

[99] Hualing Zeng, Gui-Bin Liu, Junfeng Dai, Yajun Yan, Bairen Zhu, Ruicong He, Lu Xie, Shijie Xu, Xianhui Chen, Wang Yao, et al. Optical signature of symmetry variations and spin-valley coupling in atomically thin tungsten dichalcogenides. *Sci. Rep.*, 3:1608, 2013.

[100] DA Kleinman and RC Miller. Band-gap renormalization in semiconductor quantum wells containing carriers. *Phys. Rev. B*, 32(4):2266, 1985.

[101] Hui Fang, Steven Chuang, Ting Chia Chang, Kuniharu Takei, Toshitake Takahashi, and Ali Javey. High-performance single layered WSe_2 p-FETs with chemically doped contacts. *Nano Lett.*, 12(7):3788–3792, 2012.

[102] Wei Liu, Jiahao Kang, Deblina Sarkar, Yasin Khatami, Debdeep Jena, and Kaustav Banerjee. Role of metal contacts in designing high-performance monolayer n-type WSe_2 field effect transistors. *Nano Lett.*, 13(5):1983–1990, 2013.

[103] Jun Dai, Ming Li, and Xiao Cheng Zeng. Group IVB transition metal trichalcogenides: a new class of 2D layered materials beyond graphene. *Wiley Interdisciplinary Reviews: Computational Molecular Science*, 2016.

[104] Titanium Trisulfide Monolayer. Theoretical prediction of a new direct-gap semiconductor with high and anisotropic carrier mobility dai, jun; zeng, xiao cheng. *Angew. Chem. Int. Ed.*, 54(26):7572–7576, 2015.

[105] Ming Li, Jun Dai, and Xiao Cheng Zeng. Tuning the electronic properties of transition-metal trichalcogenides via tensile strain. *Nanoscale*, 7(37):15385–15391, 2015.

[106] Jun Kang, Hasan Sahin, H Duygu Ozaydin, R Tugrul Senger, and François M Peeters. TiS_3 nanoribbons: Width-independent band gap and strain-tunable electronic properties. *Phys. Rev. B*, 92(7):075413, 2015.

[107] Joshua O Island, Mariam Barawi, Robert Biele, Adrián Almazán, José M Clamagirand, José R Ares, Carlos Sánchez, Herre SJ van der Zant, José V Álvarez, Roberto D'Agosta, et al. TiS_3 transistors with tailored morphology and electrical properties. *Adv. Mater.*, 27(16):2595–2601, 2015.

[108] Alexey Lipatov, Peter M Wilson, Mikhail Shekhirev, Jacob D Teeter, Ross Netusil, and Alexander Sinitskii. Few-layered titanium trisulfide (TiS_3) field-effect transistors. *Nanoscale*, 7(29):12291–12296, 2015.

[109] Joshua O Island, Michele Buscema, Mariam Barawi, José M Clamagirand, José R Ares, Carlos Sánchez, Isabel J Ferrer, Gary A Steele, Herre SJ van der Zant, and Andres Castellanos-Gomez. Ultrahigh photoresponse of few-layer TiS_3 nanoribbon transistors. *Adv. Opt. Mater.*, 2(7):641–645, 2014.

[110] Aday J Molina-Mendoza, Mariam Barawi, Robert Biele, Eduardo Flores, José R Ares, Carlos Sánchez, Gabino Rubio-Bollinger, Nicolás Agraït, Roberto D'Agosta, Isabel J Ferrer, et al. Electronic bandgap and exciton binding energy of layered semiconductor TiS_3. *Adv. Electron. Mater.*, 1(9), 2015.

[111] Akitoshi Hayashi, Takuya Matsuyama, Atsushi Sakuda, and Masahiro Tatsumisago. Amorphous titanium sulfide electrode for all-solid-state rechargeable lithium batteries with high capacity. *Chem. Lett.*, 41(9):886–888, 2012.

[112] M Barawi, E Flores, IJ Ferrer, JR Ares, and C Sánchez. Titanium trisulphide (TiS_3) nanorib-

bons for easy hydrogen photogeneration under visible light. *J. Mater. Chem. A*, 3(15):7959–7965, 2015.

[113] Qiannan Cui, Alexey Lipatov, Jamie Samantha Wilt, Matthew Z Bellus, Xiao Cheng Zeng, Judy Wu, Alexander Sinitskii, and Hui Zhao. Time-resolved measurements of photocarrier dynamics in tis3 nanoribbons. *ACS Appl. Mater. Interfaces*, 8(28):18334–18338, 2016.

[114] IJ Ferrer, JR Ares, JM Clamagirand, M Barawi, and C Sánchez. Optical properties of titanium trisulphide (TiS_3) thin films. *Thin Solid Films*, 535:398–401, 2013.

[115] Dezheng Sun, Yi Rao, Georg A Reider, Gugang Chen, Yumeng You, Louis Brezin, Avetik R Harutyunyan, and Tony F Heinz. Observation of rapid exciton-exciton annihilation in monolayer molybdenum disulfide. *Nano Lett.*, 14(10):5625–5629, 2014.

[116] Srabani Kar, Yang Su, RR Nair, and AK Sood. Probing photoexcited carriers in a few-layer MoS_2 laminate by time-resolved optical pump-terahertz probe spectroscopy. *ACS Nano*, 9(12):12004–12010, 2015.

[117] Nardeep Kumar, Qiannan Cui, Frank Ceballos, Dawei He, Yongsheng Wang, and Hui Zhao. Exciton-exciton annihilation in $MoSe_2$ monolayers. *Phys. Rev. B*, 89(12):125427, 2014.

[118] Long Yuan and Libai Huang. Exciton dynamics and annihilation in WS_2 2D semiconductors. *Nanoscale*, 7(16):7402–7408, 2015.

[119] Shinichiro Mouri, Yuhei Miyauchi, Minglin Toh, Weijie Zhao, Goki Eda, and Kazunari Matsuda. Nonlinear photoluminescence in atomically thin layered WSe_2 arising from diffusion-assisted exciton-exciton annihilation. *Phys. Rev. B*, 90(15):155449, 2014.

[120] K Friemelt, L Kulikova, L Kulyuk, A Siminel, E Arushanov, Ch Kloc, and E Bucher. Optical and photoelectrical properties of ReS_2 single crystals. *J. Appl. Phys.*, 79(12):9268–9272, 1996.

[121] CH Ho, PC Liao, YS Huang, and KK Tiong. Temperature dependence of energies and broadening parameters of the band-edge excitons of ReS_2 and $ReSe_2$. *Phys. Rev. B*, 55(23):15608, 1997.

[122] CH Ho, PC Liao, YS Huang, and KK Tiong. Piezoreflectance study of the band-edge excitons of ReS_2. *Solid State Commun.*, 103(1):19–23, 1997.

[123] CH Ho, YS Huang, JL Chen, TE Dann, and KK Tiong. Electronic structure of ReS_2 and $ReSe_2$ from first-principles calculations, photoelectron spectroscopy, and electrolyte electroreflectance. *Phys. Rev. B*, 60(23):15766, 1999.

[124] K Friemelt, M-Ch Lux-Steiner, and E Bucher. Optical properties of the layered transition-metal-dichalcogenide ReS_2: anisotropy in the van der Waals plane. *J. Appl. Phys.*, 74(8):5266–5268, 1993.

[125] G Leicht, H Berger, and F Levy. The growth of n-and p-type ReS_2 and $ReSe_2$ single crystals and their electrical properties. *Solid State Commun.*, 61(9):531–534, 1987.

[126] Sefaattin Tongay, Hasan Sahin, Changhyun Ko, Alex Luce, Wen Fan, Kai Liu, Jian Zhou, Ying-Sheng Huang, Ching-Hwa Ho, Jinyuan Yan, et al. Monolayer behaviour in bulk ReS_2 due to electronic and vibrational decoupling. *Nat. Commun.*, 5, 2014.

[127] Stephen P Kelty, Albert F Ruppert, Russell R Chianelli, Jingqing Ren, and M-H Whangbo. Scanning probe microscopy study of layered dichalcogenide ReS_2. *J. Am. Chem. Soc.*, 116(17):7857–7863, 1994.

[128] HH Murray, SP Kelty, RR Chianelli, and CS Day. Structure of rhenium disulfide. *Inorg. Chem.*, 33(19):4418–4420, 1994.

[129] CH Ho, YS Huang, KK Tiong, and PC Liao. In-plane anisotropy of the optical and electrical properties of layered ReS_2 crystals. *J. Phys.: Condens. Matter*, 11(27):5367, 1999.

[130] CH Ho, YS Huang, KK Tiong, and PC Liao. Absorption-edge anisotropy in ReS_2 and $ReSe_2$ layered semiconductors. *Phys. Rev. B*, 58(24):16130, 1998.

[131] S Horzum, D Çakır, J Suh, S Tongay, Y-S Huang, C-H Ho, J Wu, H Sahin, and FM Peeters. Formation and stability of point defects in monolayer rhenium disulfide. *Phys. Rev. B*, 89(15):155433, 2014.

[132] Takeshi Fujita, Yoshikazu Ito, Yongwen Tan, Hisato Yamaguchi, Daisuke Hojo, Akihiko Hirata, Damien Voiry, Manish Chhowalla, and Mingwei Chen. Chemically exfoliated ReS_2 nanosheets. *Nanoscale*, 6(21):12458–12462, 2014.

[133] Xuexia He, Fucai Liu, Peng Hu, Wei Fu, Xingli Wang, Qingsheng Zeng, Wu Zhao, and Zheng Liu. Chemical vapor deposition of high-quality and atomically layered ReS_2. *Small*, 11(40):5423–5429, 2015.

[134] Kunttal Keyshar, Yongji Gong, Gonglan Ye, Gustavo Brunetto, Wu Zhou, Daniel P Cole, Ken Hackenberg, Yongmin He, Leonardo Machado, Mohamad Kabbani, et al. Chemical vapor deposition of monolayer rhenium disulfide (ReS_2). *Adv. Mater.*, 27(31):4640–4648, 2015.

[135] Qiannan Cui, Jiaqi He, Matthew Z. Bellus, Mirzojamshed Mirzokarimov, Tino Hofmann, Hsin-Ying Chiu, Matthew Antonik, Dawei He, Yongsheng Wang, and Hui Zhao. Transient absorption measurements on anisotropic monolayer ReS_2. *Small*, 2015.

[136] L. V. Keldysh. Excitons in semiconductor-dielectric nanostructures. *Phys. Status Solidi A*, 164(1):3–12, 1997.

[137] Nardeep Kumar, Qiannan Cui, Frank Ceballos, Dawei He, Yongsheng Wang, and Hui Zhao. Exciton diffusion in monolayer and bulk $MoSe_2$. *Nanoscale*, 6(9):4915–4919, 2014.

[138] Jiaqi He, Dawei He, Yongsheng Wang, Qiannan Cui, Frank Ceballos, and Hui Zhao. Spa-

tiotemporal dynamics of excitons in monolayer and bulk WS_2. *Nanoscale*, 7(21):9526–9531, 2015.

[139] Albert Einstein. *Investigations on the Theory of the Brownian Movement*. Courier Corporation, 1956.

[140] Mark Lundstrom. *Fundamentals of carrier transport*. Cambridge University Press, 2009.

[141] M Heiblum, MI Nathan, Dd C Thomas, and CM Knoedler. Direct observation of ballistic transport in GaAs. *Phys. Rev. Lett.*, 55(20):2200, 1985.

[142] Kong-Thon Tsen. *Ultrafast Phenomena in Semiconductors*. Springer Science & Business Media, 2012.

[143] Youngki Yoon, Kartik Ganapathi, and Sayeef Salahuddin. How good can monolayer MoS_2 transistors be? *Nano Lett.*, 11(9):3768–3773, 2011.

[144] Hui Zhao, Arthur L Smirl, and HM van Driel. Temporally and spatially resolved ballistic pure spin transport. *Phys. Rev. B*, 75(7):075305, 2007.

[145] C. H. Ho, Y. S. Huang, K. K. Tiong, and P. C. Liao. In-plane anisotropy of the optical and electrical properties of layered ReS_2 crystals. *J. Phys.: Condens. Matter*, 11(27):5367, 1999.

[146] S. Schmitt-Rink, D. S. Chemla, and D. A. B. Miller. Theory of transient excitonic optical nonlinearities in semiconductor quantum-well structures. *Phys. Rev. B*, 32(10):6601, 1985.

[147] PA Franken, Alan E Hill, CW el Peters, and G Weinreich. Generation of optical harmonics. *Phys. Rev. Lett.*, 7(4):118, 1961.

[148] Nardeep Kumar, Sina Najmaei, Qiannan Cui, Frank Ceballos, Pulickel M Ajayan, Jun Lou, and Hui Zhao. Second harmonic microscopy of monolayer MoS_2. *Phys. Rev. B*, 87(16):161403, 2013.

[149] Rodrigo E. Muniz and John E. Sipe. Point group symmetries and optical properties of 1T layered materials. Private Communication, 2016.

[150] Liang Wu, Shreyas Patankar, Takahiro Morimoto, Nityan L Nair, Eric Thewalt, Arielle Little, James G Analytis, Joel E Moore, and J Orenstein. Giant anisotropic nonlinear optical response in transition metal monopnictide Weyl semimetals. *Nat. Phys.*, 2016.

[151] Rui Wang, Brian A Ruzicka, Nardeep Kumar, Matthew Z Bellus, Hsin-Ying Chiu, and Hui Zhao. Ultrafast and spatially resolved studies of charge carriers in atomically thin molybdenum disulfide. *Phys. Rev. B*, 86(4):045406, 2012.

[152] Di Xiao, Gui-Bin Liu, Wanxiang Feng, Xiaodong Xu, and Wang Yao. Coupled spin and valley physics in monolayers of MoS_2 and other group-VI dichalcogenides. *Phys. Rev. Lett.*, 108(19):196802, 2012.

[153] Rodrigo A Muniz and JE Sipe. All-optical injection of charge, spin, and valley currents in monolayer transition-metal dichalcogenides. *Phys. Rev. B*, 91(8):085404, 2015.

[154] Alexey Chernikov, Timothy C Berkelbach, Heather M Hill, Albert Rigosi, Yilei Li, Ozgur Burak Aslan, David R Reichman, Mark S Hybertsen, and Tony F Heinz. Exciton binding energy and nonhydrogenic Rydberg series in monolayer WS_2. *Phys. Rev. Lett.*, 113(7):076802, 2014.

[155] Keliang He, Nardeep Kumar, Liang Zhao, Zefang Wang, Kin Fai Mak, Hui Zhao, and Jie Shan. Tightly bound excitons in monolayer WSe_2. *Phys. Rev. Lett.*, 113(2):026803, 2014.

[156] Rui Wang, Hui-Chun Chien, Jatinder Kumar, Nardeep Kumar, Hsin-Ying Chiu, and Hui Zhao. Third-harmonic generation in ultrathin films of MoS_2. *ACS Appl. Mater. Interfaces*, 6(1):314–318, 2013.

[157] Carlos Torres-Torres, Néstor Perea-López, Ana Laura Elías, Humberto R Gutiérrez, David A Cullen, Ayse Berkdemir, Florentino López-Urías, Humberto Terrones, and Mauri-

cio Terrones. Third order nonlinear optical response exhibited by mono-and few-layers of WS_2. *2D Mater.*, 3(2):021005, 2016.

[158] Kangpeng Wang, Jun Wang, Jintai Fan, Mustafa Lotya, Arlene O'Neill, Daniel Fox, Yanyan Feng, Xiaoyan Zhang, Benxue Jiang, and Quanzhong Zhao. Ultrafast saturable absorption of two-dimensional MoS_2 nanosheets. *ACS Nano*, 7(10):9260–9267, 2013.

[159] Andre K Geim and Irina V Grigorieva. Van der Waals heterostructures. *Nature*, 499(7459):419–425, 2013.

[160] HH Murray, SP Kelty, RR Chianelli, and CS Day. Structure of rhenium disulfide. *Inorg. Chem.*, 33(19):4418–4420, 1994.

[161] Sefaattin Tongay, Hasan Sahin, Changhyun Ko, Alex Luce, Wen Fan, Kai Liu, Jian Zhou, Ying-Sheng Huang, Ching-Hwa Ho, and Jinyuan Yan. Monolayer behaviour in bulk ReS_2 due to electronic and vibrational decoupling. *Nat. Commun.*, 5, 2014.

[162] Qiannan Cui and Hui Zhao. Coherent control of nanoscale ballistic currents in transition metal dichalcogenide ReS_2. *ACS Nano*, 9(4):3935–3941, 2015.

[163] Daniel A Chenet, O Burak Aslan, Pinshane Y Huang, Chris Fan, Arend M van der Zande, Tony F Heinz, and James C Hone. In-plane anisotropy in mono-and few-layer ReS_2 probed by raman spectroscopy and scanning transmission electron microscopy. *Nano Lett.*, 15(9):5667–5672, 2015.

[164] Qiannan Cui, Jiaqi He, Matthew Z Bellus, Mirzojamshed Mirzokarimov, Tino Hofmann, Hsin-Ying Chiu, Matthew Antonik, Dawei He, Yongsheng Wang, and Hui Zhao. Transient absorption measurements on anisotropic monolayer ReS_2. *Small*, 11(41):5565–5571, 2015.

[165] Rui He, Jia-An Yan, Zongyou Yin, Zhipeng Ye, Gaihua Ye, Jason Cheng, Ju Li, and Chun Hung Lui. Coupling and stacking order of ReS_2 atomic layers revealed by ultralow-frequency Raman spectroscopy. *Nano Lett.*, 16(2):1404–1409, 2016.

[166] Jian Gao, Lu Li, Jiawei Tan, Hao Sun, Baichang Li, Juan Carlos Idrobo, Chandra Veer Singh, Toh-Ming Lu, and Nikhil Koratkar. Vertically oriented arrays of ReS_2 nanosheets for electrochemical energy storage and electro-catalysis. *Nano Lett.*, 16(6):3780–3787, 2016.

[167] Qin Zhang, Shuangjie Tan, Rafael G Mendes, Zhongti Sun, Yongting Chen, Xin Kong, Yinghui Xue, Mark H Rümmeli, Xiaojun Wu, and Shengli Chen. Extremely weak van der Waals coupling in vertical ReS_2 nanowalls for high-current-density lithium-ion batteries. *Adv. Mater.*, 28(13):2616—2623, 2016.

[168] Erfu Liu, Yajun Fu, Yaojia Wang, Yanqing Feng, Huimei Liu, Xiangang Wan, Wei Zhou, Baigeng Wang, Lubin Shao, and Ching-Hwa Ho. Integrated digital inverters based on two-dimensional anisotropic ReS_2 field-effect transistors. *Nat. Commun.*, 6, 2015.

[169] Shengxue Yang, Jun Kang, Qu Yue, JMD Coey, and Chengbao Jiang. Defect-modulated transistors and gas-enhanced photodetectors on ReS_2 nanosheets. *Adv. Mater. Interfaces*, 3(6), 2016.

[170] Enze Zhang, Yibo Jin, Xiang Yuan, Weiyi Wang, Cheng Zhang, Lei Tang, Shanshan Liu, Peng Zhou, Weida Hu, and Faxian Xiu. ReS_2-based field-effect transistors and photodetectors. *Adv. Funct. Mater.*, 25(26):4076–4082, 2015.

[171] Mohammad Najmzadeh, Changhyun Ko, Kedi Wu, Sefaattin Tongay, and Junqiao Wu. Multilayer res2 lateral p–n homojunction for photoemission and photodetection. *Appl. Phys Express*, 9(5):055201, 2016.

[172] Fucai Liu, Shoujun Zheng, Xuexia He, Apoorva Chaturvedi, Junfeng He, Wai Leong Chow, Thomas R Mion, Xingli Wang, Jiadong Zhou, and Qundong Fu. Highly sensitive detection of polarized light using anistropic 2D ReS_2. *Adv. Funct. Mater.*, 26(8):1169–1177, 2015.

[173] DJ Moss, Henry M van Driel, and John E Sipe. Dispersion in the anisotropy of optical third-harmonic generation in silicon. *Opt. Lett.*, 14(1):57–59, 1989.

[174] JE Sipe, DJ Moss, and HM Van Driel. Phenomenological theory of optical second-and third-harmonic generation from cubic centrosymmetric crystals. *Phys. Rev. B*, 35(3):1129, 1987.

[175] Andres Castellanos-Gomez, Michele Buscema, Rianda Molenaar, Vibhor Singh, Laurens Janssen, Herre SJ van der Zant, and Gary A Steele. Deterministic transfer of two-dimensional materials by all-dry viscoelastic stamping. *2D Mater.*, 1(1):011002, 2014.

[176] Ozgur Burak Aslan, Daniel A Chenet, Arend M van der Zande, James C Hone, and Tony F Heinz. Linearly polarized excitons in single-and few-layer ReS_2 crystals. *ACS Photonics*, 3(1):96–101, 2015.

[177] Peter Günter. *Nonlinear optical effects and materials*, volume 72. Springer, 2012.

[178] JH Bechtel and W Lee Smith. Two-photon absorption in semiconductors with picosecond laser pulses. *Phys. Rev. B*, 13(8):3515, 1976.

[179] Eric W Van Stryland, H Vanherzeele, M Am Woodall, MJ Soileau, Arthur L Smirl, Shekhar Guha, and Thomas F Boggess. Two photon absorption, nonlinear refraction, and optical limiting in semiconductors. *Opt. Eng.*, 24(4):244613–244613, 1985.

[180] Vaidya Nathan, Arthur H Guenther, and Shashanka S Mitra. Review of multiphoton absorption in crystalline solids. *J. Opt. Soc. Am. B*, 2(2):294–316, 1985.

[181] Alan D Bristow, Nir Rotenberg, and Henry M Van Driel. Two-photon absorption and Kerr coefficients of silicon for 850-2200 nm. *Appl. Phys. Lett.*, 90(19):191104, 2007.

[182] Q Lin, Oskar J Painter, and Govind P Agrawal. Nonlinear optical phenomena in silicon waveguides: modeling and applications. *Opt. Express*, 15(25):16604–16644, 2007.

[183] ER Thoen, EM Koontz, M Joschko, P Langlois, TR Schibli, FX Kärtner, EP Ippen, and LA Kolodziejski. Two-photon absorption in semiconductor saturable absorber mirrors. *Appl. Phys. Lett.*, 74(26):3927–3929, 1999.

[184] Qiaoliang Bao, Han Zhang, Yu Wang, Zhenhua Ni, Yongli Yan, Ze Xiang Shen, Kian Ping Loh, and Ding Yuan Tang. Atomic-layer graphene as a saturable absorber for ultrafast pulsed lasers. *Adv. Funct. Mater.*, 19(19):3077–3083, 2009.

[185] Kangpeng Wang, Jun Wang, Jintai Fan, Mustafa Lotya, Arlene O?Neill, Daniel Fox, Yanyan Feng, Xiaoyan Zhang, Benxue Jiang, Quanzhong Zhao, et al. Ultrafast saturable absorption of two-dimensional MoS_2 nanosheets. *ACS Nano*, 7(10):9260–9267, 2013.

[186] Shuxian Wang, Haohai Yu, Huaijin Zhang, Aizhu Wang, Mingwen Zhao, Yanxue Chen, Liangmo Mei, and Jiyang Wang. Broadband few-layer MoS_2 saturable absorbers. *Adv. Mater.*, 26(21):3538–3544, 2014.

[187] Yu Chen, Guobao Jiang, Shuqing Chen, Zhinan Guo, Xuefeng Yu, Chujun Zhao, Han Zhang, Qiaoliang Bao, Shuangchun Wen, Dingyuan Tang, et al. Mechanically exfoliated black phosphorus as a new saturable absorber for both Q-switching and mode-locking laser operation. *Opt. Express*, 23(10):12823–12833, 2015.

[188] D Popa, Z Sun, T Hasan, F Torrisi, F Wang, and AC Ferrari. Graphene q-switched, tunable fiber laser. *Appl. Phys. Lett.*, 98(7):073106, 2011.

[189] Qiaoliang Bao and Kian Ping Loh. Graphene photonics, plasmonics, and broadband optoelectronic devices. *ACS Nano*, 6(5):3677–3694, 2012.

[190] Juan Du, Qingkai Wang, Guobao Jiang, Changwen Xu, Chujun Zhao, Yuanjiang Xiang, Yu Chen, Shuangchun Wen, and Han Zhang. Ytterbium-doped fiber laser passively mode locked by few-layer molybdenum disulfide (MoS_2) saturable absorber functioned with evanescent field interaction. *Sci. Rep.*, 4:6346, 2014.

[191] Saifeng Zhang, Ningning Dong, Niall McEvoy, Maria O?Brien, Sinéad Winters, Nina C Berner, Chanyoung Yim, Yuanxin Li, Xiaoyan Zhang, Zhanghai Chen, et al. Direct observation of degenerate two-photon absorption and its saturation in WS_2 and MoS_2 monolayer and few-layer films. *ACS Nano*, 9(7):7142–7150, 2015.

[192] Marco Bernardi, Maurizia Palummo, and Jeffrey C Grossman. Extraordinary sunlight absorption and one nanometer thick photovoltaics using two-dimensional monolayer materials. *Nano Lett.*, 13(8):3664–3670, 2013.

[193] Eric W Van Stryland, MA Woodall, H Vanherzeele, and MJ Soileau. Energy band-gap dependence of two-photon absorption. *Opt. Lett.*, 10(10):490–492, 1985.

[194] T Boggess, A Smirl, S Moss, I Boyd, and E Van Stryland. Optical limiting in GaAs. *IEEE J. Quantum Electron.*, 21(5):488–494, 1985.

[195] AA Said, Mansoor Sheik-Bahae, David J Hagan, TH Wei, J Wang, James Young, and Eric W Van Stryland. Determination of bound-electronic and free-carrier nonlinearities in ZnSe, GaAs, CdTe, and ZnTe. *J. Opt. Soc. Am. B.*, 9(3):405–414, 1992.

Appendix A

List of publications

1. Qiannan Cui, Rodrigo A. Muniz, John E. Sipe, and Hui Zhao, "Strong and anisotropic third harmonic generation in monolayer and bulk ReS_2," ***Phys. Rev. B*** 95, 165406 (2017).

2. Qiannan Cui, Alexey Lipatov, Jamie Wilt, Matthew Z. Bellus, Xiao-Cheng Zeng, Judy Wu, Alexander Sinitskii, and Hui Zhao, "Time-resolved measurements of photocarrier dynamics in TiS_3 nanoribbons," ***ACS Appl. Mater. Interfaces*** 8, 28 (2016).

3. Qiannan Cui, Jiaqi He, Matthew Z. Bellus, Mirzojamhed Mirzokarimov, Tino Hofmann, Hsin-Ying Chiu, Matthew Antonik, Dawei He, Yongsheng Wang, and Hui Zhao, "Transient absorption measurements on anisotropic monolayer ReS_2," ***Small*** 11, 41 (2015).

4. Qiannan Cui and Hui Zhao, "Coherent control of nanoscale ballistic currents in transition metal dichalcogenide ReS_2," ***ACS Nano*** 9, 4 (2015).

5. Qiannan Cui, Frank Ceballos, Nardeep Kumar, and Hui Zhao, "Transient absorption microscopy of monolayer and bulk WSe_2," ***ACS Nano*** 8, 3 (2014).

6. Matthew Z. Bellus, Ming Li, Samuel D. lane, Frank Ceballos, Qiannan Cui, Xiao Cheng Zeng, and Hui Zhao, "Type-I van der Waals heterostructure formed by MoS_2 and ReS_2 monolayers," ***Nanoscale Horiz.*** 2, 1 (2017).

7. Frank Ceballos, Qiannan Cui, Matthew Z. Bellus, and Hui Zhao, "Exciton formation in monolayer transition metal dichalcogenides," ***Nanoscale*** 8, 22 (2016).

8. Jiaqi He, Yongsheng Wang, Qiannan Cui, Matthew Z. Bellus, Hsin-Ying Chiu, and Hui Zhao, "Exceptional and anisotropic transport properties of photocarriers in black phosphorus," ***ACS Nano*** 9, 6 (2015).

9. Jiaqi He, Dawei He, Yongsheng Wang, Qiannan Cui, Frank Ceballos, and Hui Zhao, "Spatiotemporal dynamics of excitons in monolayer and bulk WS_2," ***Nanoscale*** 7, 21 (2015).

10. Maogang Gong, Tejas A. Shastry, Qiannan Cui, Ryan R. Kohlmeyer, Kyle A. Luck, Andrew Rowberg, Tobin J. Mark, Michael F. Durstock, Hui Zhao, Mark C. Hersam, and Shenqiang Ren, "Understanding charge transfer in carbon nanotube-fullerene bulk heterojunctions," ***ACS Appl. Mater. Interfaces*** 7, 13 (2015).

11. Nardeep Kumar, Qiannan Cui, Frank Ceballos, Dawei He, Yongsheng Wang and Hui Zhao, "Exciton diffusion in monolayer and bulk $MoSe_2$," ***Nanoscale*** 6, 9 (2014).

12. Nardeep Kumar, Qiannan Cui, Frank Ceballos, Dawei He, Yongsheng Wang, Hui Zhao, "Exciton-exciton annihilation in $MoSe_2$ monolayers," ***Phys. Rev. B*** 89, 12 (2014).

13. Nardeep Kumar, Sina Najmaei, Qiannan Cui, Frank Ceballos, Pulickel M. Ajayan, Jun Lou, and Hui Zhao, "Second harmonic microscopy of monolayer MoS_2," ***Phys. Rev. B*** 87, 16 (2013).